UNIVERSIDAD POLITÉCNICA DE MADRID
Escuela Técnica Superior de Ingenieros de Caminos, Canales y Puertos

Phase control for semi-active applications: inertial mass dampers and base isolation systems

D O C T O R A L T H E S I S

Submitted for the degree of Doctor by:

Christian Alexander Barrera Vargas
MSc. Civil Engineer

Madrid, 2023


UNIVERSIDAD POLITÉCNICA DE MADRID
Escuela Técnica Superior de Ingenieros de Caminos, Canales y Puertos

Doctoral Degree in Engineering of Structures, Foundations and Materials

Phase control for semi-active applications: inertial mass dampers and base isolation systems

D O C T O R A L T H E S I S

Submitted for the degree of Doctor by:

Christian Alexander Barrera Vargas
MSc. Civil Engineer

Under the supervision of:
Dr. Ivan Muñoz Díaz
Dr. Jaime Higinio García Palacios

Madrid, 2023

Title: Phase control for semi-active applications: inertial mass dampers and base isolation systems

Author: Christian Alexander Barrera Vargas

Doctoral Programme: Engineering of Structures, Foundations and Materials

Thesis Supervision:

Dr. Ivan Muñoz Díaz, Professor, Universidad Politécnica de Madrid (Supervisor)

Dr. Jaime Higinio García Palacios, Professor, Universidad Politécnica de Madrid (Supervisor)

External Reviewers:

Thesis Defense Committee:

Thesis Defense Date:

This thesis has been supported by *Ministry of Science, Innovation and Universities of Spain*, for the financial support through the FPI grant within the project "Structural Efficiency Enhancement for Bridges subjected to Dynamic Loading: Integrated Smart Dampers SEED-SD"(RTI2018-099639-BI00).

Acknowledgments

In these years I have learned so much that it is difficult to explain in a few lines how grateful I am. There were great people who were part of this process, so I want to express my gratitude to them:

→ *Iván Muñoz Díaz*, his dedication as an advisor made it possible for this research work to achieve the proposed objectives. His kindness and simplicity made that his vast knowledge was acquired in a very pleasant way. In addition, his advice helped me a lot in my academic and personal formation. I hope to continue learning a lot from him.

→ *Jaime García Palacios*, his great work as co-advisor was of great help during all this time, I acquired a lot of knowledge during this time followed by an excellent sense of humor. I also hope to continue learning from him.

→ *Carlos Zanuy, Elena Pilar, Gonzalo Saenz, Isidro García y Miguel Angel Peña.* The little breaks in which we shared funny anecdotes and laughs made my life happy.

→ *Javier Naranjo, Christian Gallegos, Carlos Martín y Jose Soría.* The long working days in which they shared their knowledge, joys, and jokes, were fundamental to carrying out this work.

→ *Prof. Dimitrios Konstantinidis and UC Berkeley students.* Prof. Dimitrios and UC Berkeley students. During my research stay, I had the opportunity to learn from the vast experiences and knowledge provided by Prof. Dimitrios, who always shared pleasant conversations and great advice. To my friends at Berkeley, Gabriela, Miguel, Ya−heng, Panorea, Maria, Dimi, Alex, Camila, Diego, Eduardo, Goktug and all the others, thank you for the happy moments.

→ *Ph.D. Students at ETSI Caminos, Canales y Puertos.* Benedetta, Rafael, Marck, Belén y Luis, we have been a long time working together, thanks for your shared time, knowledge, and amazing mood.

→ *Ministry of Science, Innovation and Universities of Spain*, for the financial support through the FPI grant within the project "Structural Efficiency Enhancement

for Bridges subjected to Dynamic Loading: Integrated Smart Dampers SEED-SD"(RTI2018-099639-BI00).

Last but very important I would like to thank my family, the long distance kept us apart, but you were always in my mind, you are everything in my life. To my friends Eduard, Stanislav, Yesica, Tomas, Esther, Rodrigo, Diego, Magaly and Fernando thank you very much for the laughs, the advice, the meals and the trips. Words cannot adequately express my gratitude.

Abstract

The new challenges of civil engineering are focused on the development of sustainable structures and the need to reduce the carbon footprint. Under these circumstances, structures will be more slender and prone to vibration problems, which give rise to the presence of local failures or collapse situations.

On the one hand, these vibrations may be due to the action of a pedestrian or group of pedestrians walking with possible resonance effects if the passing frequency, or any of its higher harmonics, is close to the natural frequency of the structure; this effect is more likely to occur in the case of lightweight structures with low mass/stiffness ratio. On the other hand, wind and earthquakes action generates vibrations on the structure. The particularity of this type of load lies in the uncertainty that exists in the dynamic characteristics of the excitation and how it can affect the structure. Without a correct evaluation of this effect, the design behavior may deviate from reality.

The most common solution to control the vibration problems consists of increasing the stiffness of the structure with two main objectives: i) to increase the fundamental frequency of the structure avoiding resonance effects and ii) to guarantee the lateral stability of the structure and reduce maximum drift caused by wind or earthquake actions.

An alternative to avoid stiffness increase in the structure is the use of passive control devices, such asTuned Mass Dampers (TMDs) and seismic base isolators. These devices do not require additional energy for their correct operation, developing adequate behavior when they are correctly tuned or designed. However, if the modal properties of the structure change over time or other uncertainty factors are present, the passive control systems may become detuned, and their performance may be far from the expected one.

In order to alleviate the detuning or saturation problems of passive devices, semi-active devices can be used to upgrade capacities. The system maintains its passive nature with low energy demand and real-time adaptative capacities as an alternative to active control systems, where unstable behaviors may occur and high energy demand for functioning is

required. In this thesis, the use of a Magnetorheological Damper (MR damper) added to a passive TMDs and to a Friction Pendulum System (FPS) isolator is explored. For both implementations, a phase control law is considered; that is, the damper activates or deactivates depending on the relative position (or acceleration) and the velocity sign. The practical implementation is quite simple since it can be implemented by using two accelerometers, one on the structure and the other on the device, and no-structural model is needed for the implementation.

The practical implementation has been tested through experimental tests carried out on a very lightweight footbridge in which human-structure-controller interaction phenomena have been considered for the design of a Semi-active Tuned Mass Damper (STMD). Additionally, realistic simulations have been undergone for friction pendulum isolators equipped with MR dampers, named as Semi-active Friction Pendulum System (SFPS). Therefore, the advantages of including semi-active dampers within the passive devices have been demonstrated in terms of performance improvements and/or reduction of the control device.

This thesis dealt with the challenge of optimizing the design of semi-active devices, which encompass both inertial controllers and isolator devices. The functional principle of the devices is based on phase control using an On-Off strategy, a continuous fixed gain control, and a variable gain control, which automatically selected its value in real time to avoid overdemand on the semi-active damper associated with the continuous fixed gain. Hence, the proposed semi-active systems controlled by phase control-based strategies enhance the passive devices in terms of effectiveness and reducing the device size.

Resumen

La ingeniería civil debe asumir los nuevos retos de sostenibilidad desarrollando estructuras más eficientes que generen una menor huella de carbono. Para ello, se requiere el diseño de estructuras esbeltas con menor consumo de material, dando lugar a estructuras propensas a sufrir problemas de vibraciones que pueden de generar fallos locales o colapso.

Por una parte, estas vibraciones pueden ser ocasionadas por la acción de un peatón o grupo de peatones al caminar sobre una estructura ligera con baja relación masa/rigidez, dando lugar a efectos de resonancia si la frecuencia de paso o alguno de sus armónicos coincide o está próxima a la frecuencia fundamental de la estructura. Por otra parte, el viento y los terremotos también pueden generar vibraciones sobre la estructura. La particularidad de este tipo de carga radica en la incertidumbre que existe en las características dinámicas de dicha excitación y como puede afectar a la estructura. Sin una correcta evaluación de la acción, el comportamiento esperado puede separarse de la realidad.

La solución más común frente a problemas de vibraciones consiste en un aumento de rigidez de la estructura con dos objetivos fundamentales: i) incrementar la frecuencia fundamental de la estructura para evitar los efectos de resonancia, y ii) garantizar la estabilidad lateral global de la estructura limitando los desplazamientos ocasionados por acciones de viento o terremotos.

La alternativa para evitar el incremento de rigidez es el uso de dispositivos de control pasivo, como pueden ser los amortiguadores de masa sintonizada o los aisladores sísmicos. Estos dispositivos desarrollan un comportamiento adecuado si se diseñan sintonizados con base en una excitación conocida. De existir cambios en la estructura o incertidumbres el funcionamiento se aleja del óptimo esperado.

La utilización de dispositivos semi-activos permiten atenuar el desintonizado o los problemas de saturación inherentes al dispositivo pasivo, mejorando sus capacidades. El sistema mantiene la naturaleza del dispositivo pasivo con una baja demanda de energía adaptando así la capacidad del sistema en tiempo real, sin acarrear comportamiento in-

estable presentes en dispositivos activos.

En esta tesis, se explora el uso de amortiguadores magneto-reológicos como dispositivo semi-activo incorporados tanto en amortiguadores de masa sintonizada como en péndulos de fricción. En ambas implementaciones, se considera el uso de una ley de control de fase para regular el comportamiento del dispositivo dependiendo de la posición relativa (o aceleración) y la velocidad registrada. Un aspecto fundamental de esta ley de control es la simplicidad al requerir el uso de dos acelerómetros, uno en la estructura y otra en el dispositivo de control, sin requerir conocer el estado completo de la estructura.

Para demostrar de forma práctica la validez de los conocimientos desarrollados en este trabajo, se han realizado ensayos experimentales en una pasarela ligera en la cual se ha considerado el fenómeno de interacción humano-estructura-controlador para el diseño de un amortiguador de masa sintonizado semi-activo. Adicionalmente, los aisladores de péndulo de fricción con amortiguadores magneto-reológicos, conocidos como sistemas de péndulo de fricción semi-activos, se han analizado bajo simulaciones realistas provenientes de terremotos registrados. Todo ello ha permitido evaluar la mejora en términos de comportamiento al incluir un dispositivo semi-activo en un actuador pasivo o en un péndulo.

Esta tesis demuestra experimentalmente, el diseño óptimo de dispositivos semi-activos inerciales y de aislamiento mediante la utilización de una ley de control de fase con base en estrategias de todo o nada, control continuo con ganancia fija y control de ganancia variable. La principal conclusión es que los sistemas semi-activos propuestos controlados por una ley de control de fase mejora el desempeño de los dispositivos y permite la reducción de su tamaño.

Contents

List of Figures

List of Tables

Acronyms

AMD Active Mass Damper

ASCE American Society of Civil Engineering

ATMD Active Tuned Mass Damper

AVS Active Variable Stiffness

CDF Cumulative Distribution Function

DAQ Data Acquisition

DBG Displacement-Based Groundhook

DFPS Double Friction Pendulum System

EPS Earthquake Protection System

ER Electrorheological Damper

FFT Fast Fourier Transforms

FPS Friction Pendulum System

FRF Frequency Response Function

FRP Fiber-Reinforced Polymers

GFRP Glass Fiber-Reinforced Polymers

HDRB High Damping Rubber Bearing

HSI Humand-Structure Interaction

LFE Low-frequency Earthquake

LRB Lead Rubber Bearing

MCE Maximum Considered Earthquake

MR damper Magnetorheological Damper

MSDA Mass-Spring-Damper Actuator

MTMD Multiple Tuned Mass Damper

MTVV Maximum Transient Vibration Value

NRB Natural Rubber Bearing

PGA Peak Ground Acceleration

PI Performance Index

PID Proportional-Integral-Derivative

PSD Power Spectral Density

TMD Tuned Mass Damper

RMS Root Mean Square

ROM Reduced-Order Model

SDOF Single-Degree-of-Freedom

SFPS Semi-active Friction Pendulum System

STMD Semi-active Tuned Mass Damper

TF Transfer Function

TFPS Triple Friction Pendulum System

TH Time History

TVA Tuned Vibration Absorber

USGS United States Geological Survey

VBG Velocity-Based Groundhook

VDV Vibration Dose Value

Chapter 1

Introduction

1.1 Motivation

The carbon footprint emissions generated by the construction industry represent about 30% of global emissions [1], with three main emitting factors presented: energy, transportation, and construction. In addition, the use of raw materials and the process of transforming them into building products are other consequences that contribute to the growth of CO2 levels [2]. Based on this issue, the need to develop sustainable projects becomes evident, one strategy to achieve these goals consists in to designing slender structures without decreasing the stability and vital safety of the structure. This is achieved by using new lightweight materials with a high strength-weight ratio together with new and innovative construction techniques. Nevertheless, structures with this characteristic may be prone to undesirable vibration effects, firstly, due to natural hazards (e.g., wind or earthquakes), and secondly, due to serviceability actions (e.g., rotation equipment or human walking effects) that structural engineering must correctly deal with them in the near future.

Wind and earthquakes are often analyzed as a lateral load that develops lateral displacements or drift associated with high stresses and vibrations due to oscillatory motions. Furthermore, for slender structures that usually have long natural periods, earthquake actions affect other vibration modes than the fundamental one, amplifying vibration effects that may generate damage in structural elements, non-structural elements, and adjacent structures [3, 4]. Additionally, sustained vibration due to wind may lead to fatigue problems, especially in structures with large fundamental period. [5].

The second type of vibration mentioned corresponds to service loads, in which structures such as concert halls or stadium bleachers with a large number of occupants are more prone to be excited by dynamic loads, usually generated by dancing or rhythmic jumping actions developing vibrations capable of inducing panic in the occupants, fatigue, and damage to the structure [6]. However, this effect is not only present in this type of structure, pedestrian-induced vibrations are also present in footbridges and floors, in which the vibration serviceability limits may be overtaken [7]. Most of the current design codes

consider the pedestrians on the structure as lumped moving loads, without considering the human-structure interaction (except for the code *"Dynamic performance requirements for permanent stands subject to crowd action"*)[8]). When dealing with lightweight pedestrian structures, human-structure interaction phenomena should be taken into account for both vibration serviceability assessment and vibration control design. That is, human-structure-controller interaction makes it obvious that human and controller dynamics should be taken into account.

An increase of stiffness in structures to control serviceability vibrations has been the most applied solution in the last years, and although it is the most common, pretending that a structure can resist the effects of a large earthquake in an elastic range may not be economically viable. Consequently, codes accept inelastic behavior with its corresponding damage. Commonly, the damage is concentrated at the join beam column and is manifested by plastic hinges. Buildings with inelastic behavior can amplify the ground acceleration experiments on each floor and how it grows until it reaches the top floor. Finally, the amplified effects drastically affect the occupants and contents of each floor. [9].

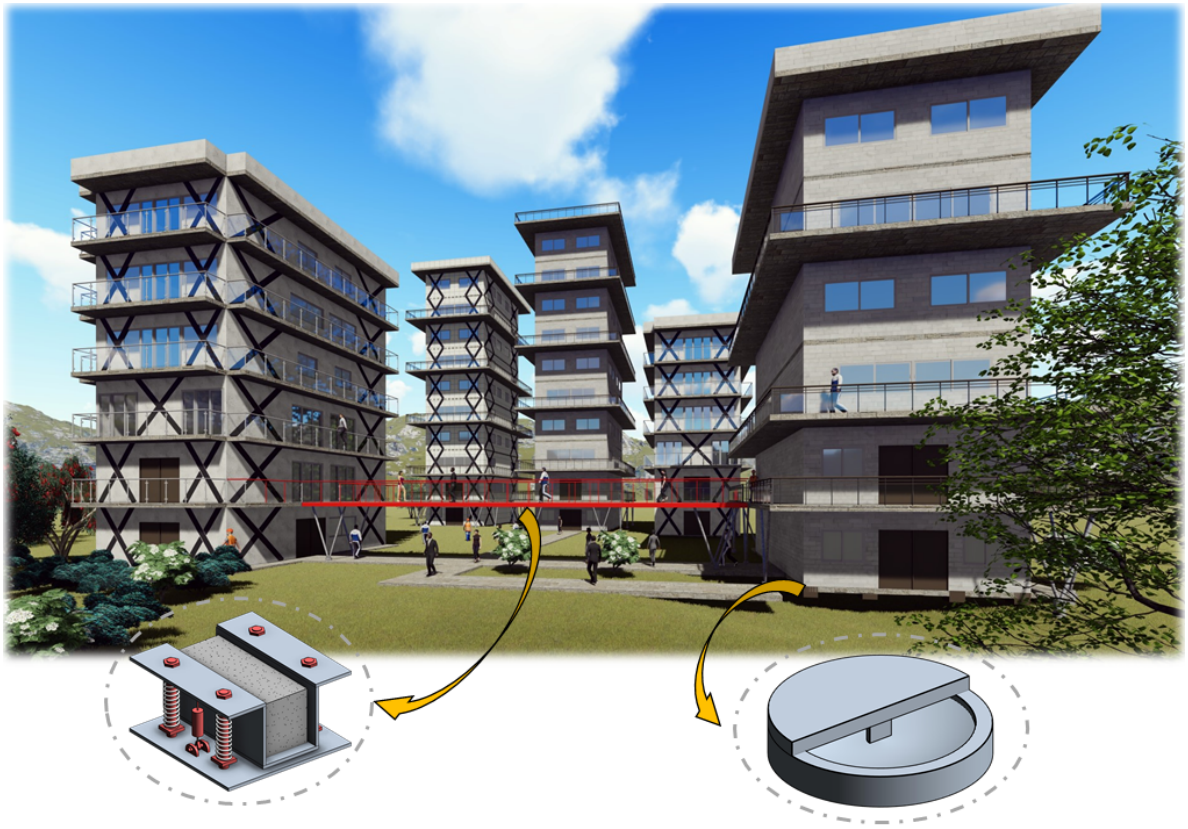

Figure 1.1: Idealization of lightweight footbridge with passive control and buildings with base isolation system.

Nowadays, earthquake protection systems are designed (especially for key facilities and buildings, such as hospitals) to allow "continued functionality."That is, the structure is fully operational after a high-intensity earthquake. In this sense, there is a need for improved vibration isolators to cope with this crucial paradigm.

Some research about the implementation of base seismic isolation has demonstrated that is possible to reduce the input ground acceleration [10, 11, 12]. As a consequence, the peak acceleration and the inter-story drift experiment in each story of the structure are reduced, which could allow optimization of the raw material consumption of the structure through a reduction in element sizes or the elimination of rigid elements, such as seismic braces (see Figure 1.1). Nevertheless, the large global displacement created by the isolation device could be a problem when adjacent structures exist [13, 14]. Different versions and base seismic isolators have been developed, such as: Lead Rubber Bearing (LRB), High Damping Rubber Bearing (HDRB), and FPS, where the FPS has better capacity to achieve reductions in the peak response acceleration developing large bearings displacements [9, 15, 16].

Although the FPS has attracted great interest as a seismic protection device, there is a paradigm for achieving the optimum design, taking into account that manufacturers do not follow the same manufacturing criteria. For example, Earthquake Protection System (EPS) company manufactures FPS with a retaining ring, while many others do not include this element. Based on the fact that the optimal behavior is achieved for large displacements in the isolator, the retaining ring is really important to avoid the collapse of the system at beyond-design demands, which is more relevant to near-fault motions [17].

The friction coefficient on the pendulum plays a crucial role in its performance. For example, for high friction values, the pendulum can absorb high-intensity earthquakes and slide around the pendulum; once the intensity of the earthquake decreases, a residual displacement could arise in the pendulum, and the isolator could not activate in case of low-intensity earthquakes. On the other hand, the recentering capacity is better for low friction, avoiding residual displacements in the pendulum and allowing the isolator to absorb low-intensity earthquakes,but with the uncertainty that a high intensity earthquake would produce the collapse of the system. In the case of the FPS with retaining ring, this leads to a significant increase in the energy transfer to the structure caused by the plate-ring impact.

In order to avoid the failure of the FPS with low friction value under a high excitation, the use of a semi-active device is able to provide and control additional damping force efficiently [18, 19, 20]. A semi-active damper attached to an FPS Is controlled with a phase control law; based on the ground acceleration and velocity of the pendulum it is possible to know the position of the upper plate and apply the damping force to reduce the excessive displacement or deactivate the semi-active damper to allow proper functionality of the isolator.

TMDs are a great solution for controlling vertical excitation produced by humans or

equipment [21, 22]. Its design requires the correct identification of the modal parameters of the structure, specifically the vibration mode to control. Although the TMD presents high effectiveness, it could develop undesirable behavior if it is detuned, and it might even amplify the acceleration response [23]. Different configurations, such as series and parallel TMDs have been studied [24, 25], achieving a larger frequency band of operative that improves the response under uncertainty in the estimation of the modal properties of both the structure and the device.

When dealing with the vibration control problem of lightweight pedestrian structures, the human-structure interaction plays an important role. The main point is that the system to be controlled is the coupled human-structure system, which may be significantly different than the simple structure. That is, the coupled human-structure system shows different dynamic properties with high damping behavior in a broad frequency band. In this case, normal-damped TMDs are quite inefficient. That is, very low damped TMDs are recommended. However, in this case, when the vibration is canceled, the TMD continues vibrating, and the structure starts to vibrate again but under the TMD's vibration effect.

Therefore, semi-active devices that can connect and disconnect smartly are needed. This may be carried out using semi-active dampers within a TMD [26, 27], which are continuously controlled using phase control law. The damper is activated depending on the relative movement between the structure and the initial mass. As a result, the upgraded STMD can efficiently detect vibrations of relatively high-damped lightweight pedestrian structures in a broader frequency band due to its real-time adaptation capabilities.

1.2 Objectives

The main objective of this thesis is to propose simple but effective strategies to enhance the performance of classical passive vibration control devices (inertial controllers and isolators). The strategies are based on integrating smart semi-active dampers within the passive systems and using the so-called phase control. Hence, the smart damper continuously modified its properties, attending to the relative movement between the structure to be controlled and the device movement. This concept has been applied and validated in two common and interesting applications: 1) vibration control of vertical human-induced vibration in lightweight structure using TMDs and 2) vibration isolation through FPS. For both applications, optimal designs have been proposed.

The following specific objectives are cope with this thesis:

- Proposing a design methodology for STMD applied to very lightweight pedestrian structures in which human-structure-controller interaction plays an important role and should considered for the controller design.

- Proposing a semi-active control strategy for an STMD based on phase control of the inertial mass and the structure movement based on magnitudes easy to measure or estimate.
- Carry out an experimental identification of several MR damper models to be used for precise simulations.
- Conduct experimental testing of the STMD developed for a large-scale laboratory footbridge.
- Study of several versions of a phase control: On-Off control, continuous control with constant gain and self-adaptive gain control.
- Propose a design methodology for SFPS to maximize the range of earthquakes for which the FPS is effective while minimizing the device size. A constrained multi-objective optimization has been proposed.
- Perform realistic simulations for an example of a real building including the MR damper model, the bidirectional behavior and the uncertainties associated with the practical implementation of a phase control law for isolators to evaluate the advantages of integrating MR damper in FPS.

1.3 Thesis outline

This thesis is composed of five chapters. Chapter 1 presents a motivation for the research, objectives, and publications developed during the research work.

Chapter 2 introduces the state of the art for passive control active control, and semi-active control. Followed for the description of semi-active devices, control strategies and control criteria for footbridge and base isolated structures.

Chapter 3 contains the overall description, analysis and performance assessment of the phase control for inertial mass dampers under vertical vibrations considering numerical models and realistic applications.

Chapter 4 studies the phase control behavior and effectiveness to control lateral vibration on semi-active base isolation devices. In this chapter also numerical models are analyzed and evaluated. Based on the configuration adopted on the semi-active control device figured out in chapter 3 for real applications. The performance for semi-active base isolation device is assessed taking into account numerical-real applications.

Finally, chapter 5 presents the conclusions of the research developed and enumerate future works for the phase control implementation.

1.4 Publications

During the development of the present doctoral thesis, the author with the contribution of other researchers developed a series of publications, which extend the contents and results

about isolation systems, tuned mass dampers, and smart dampers applied in structures. The papers published in scientific-technical journals are following described:

- Christian A. Barrera-Vargas, Javier Narajo Pérez, Iván M. Díaz, Jaime H. García-Palacios. (2022). Design of Semiactive TMD for Lightweight Pedestrian Structures Considering Human-Structure-Actuator Interaction. Actuators 2022, 11, 101; doi:10.3390/act11040101

- Christian A. Barrera-Vargas, Iván M. Díaz, José M. Soria, Jaime H. García-Palacios. (2020). Enhancing Friction Pendulum Isolation System Using Passive and Semi-Active Dampers. Appl. Sci. 2020, 10, 5621; doi:10.3390/app10165621

Within the same period, some papers published were presented in national and international conferences, which are listed below:

- *Dynamic Response of a Controlled FRP Footbridge: Implications of Human-Structure Interaction Phenomenon.* Iván M. Díaz, Christian Gallegos Calderón, Javier Naranjo Pérez, Christian A. Barrera-Vargas. **10th International Conference on Experimental Vibration Analysis for Civil Engineering Structures (2023)**.

- *Vibration Control Realizations on a Lightweight FRP Footbridge.*Iván M. Díaz, Christian Gallegos Calderón, José Ramírez Senent, Christian A. Barrera-Vargas. **8th World Conference on Structural Control and Monitoring (2022)**.

- *Semi-Active Tuned Mass Damper: Magnetorheological damper Identification and Performance Evaluation.* Christian A. Barrera-Vargas, Iván M. Díaz, Jaime H. García-Palacios, José M. Soria. (2019). **2nd Conference on Structural Dynamics (2021)**

- *In the Search of Modal Parameters Configuration of Passive and Active Isolation Systems, Applied to Moment Frames.* Christian A. Barrera-Vargas, Soria, José M.; Díaz; Iván M.; García-Palacios, Jaime H. **5th International Conference on Mechanical Models in Structural Engineering (2019)**.

- *On The Search of Multiple Tuned Mass Damper Configurations for a Vibration Mode with Changing Modal Properties.* Christian A. Barrera-Vargas, José M. Soria, Xidong Wang, Iván M. Díaz, Jaime H. García Palacios. **1st Conference on Structural Dynamics (2018)**.

Chapter 2

Magnetorheological Dampers for Structural Control

This chapter presents the state of the art on structural control systems, mainly passive, active and semi-active control. The MR damper is defined as a semi-active device, while three numerical models to reproduce its hysteretic behavior are reviewed. Finally, some control strategies based on force control and phase control used in active or semi-active control are disclosed.

2.1 Structural control systems

The use of a control system was introduced in civil engineering to limit vibration in buildings and bridges due to the action of earthquakes or wind [28]. These actions are characterized by their cyclic behavior, which can produce damage represented in plastic hinges followed by an increase in lateral deformation. In case of significant deformation, there is a considerable risk of collapse. The implementation of control systems leads to a remarkable increase in the safety of the structure.

This approach earned a substantial interest, and many investigations have been developed for various types of structures and different versions of control systems. The general literature review classifies control systems into passive, active, and semi-active according to their operating mechanisms [29]. Each type of control system is presented in the following sections:

2.1.1 Passive Control

Passive control is characterized by dissipating the input energy through elastic energy and can be classified into three types of strategies: vibration isolators, dissipative systems, and inertial controller. These systems have the advantage of achieving large deformation and,

in some cases, returning to the original shape.

First, vibration isolators mitigate the vibration by reducing the mechanical interaction between the vibration source and the structure, placing a device (isolator) between them. Thus, the isolator filters out the base movement to the structure. Excitation frequencies higher than a value are filtered out. However, smaller frequencies from that value increase the transmitted movement to the structure. This isolators, also called seismic isolation devices, are used to decouple the structure from the ground. Earthquake energy is dissipated through deformation on the isolator before the energy fully affects the structure. Since the first US patent issued for an isolation system in 1870 [30] in San Francisco, this technique has been growing worldwide. Figure 2.1a shows the San Francisco Hall City building in (USA) built with 530 isolation devices in 1915 [31], while Figure 2.1b shows the Adana Integrated Health Campus in Adana (Turkey), built in 2017 on 1512 base isolators.

(a) San Francisco City Hall (b) Adana Integrated Health Campus

Figure 2.1: Building constructed with base isolation devices (Figures obtained from [32, 33]).

Within the base isolation systems, three main types of isolators can be found: elastomeric bearing, lead rubber bearing, and sliding frictional pendulum, which are explained in detail in chapter 4.

Second, dissipative systems increase the damping by dissipating energy inside the structure. Commonly, energy dissipation starts with the deformation of the structure, and the releasing energy is produced through hinge, frictional damping, or viscous mechanism. These strategies are useful for controlling dynamic responses. However, the performance is usually limited by the damage associated.

Dissipative systems provide additional stiffness and damping without needing an external energy source, as occurs with active or semi-active systems. This category includes metallic dampers, frictional dampers, viscous fluid dampers, and viscoelastic solid dampers [34]. All of these require an auxiliary chevron frame or braces to be adapted

to the main structure. However, their performance in dissipating energy is different i.e., metallic dampers consist of a chevron frame connected to the structure by a series of plates, where the energy dissipation is performed by plastic deformation of the plates, developing a stable hysteretic behavior. Once the plastic deformation has occurred, it is necessary to replace these elements, while for frictional and viscous dampers, it is not necessary.

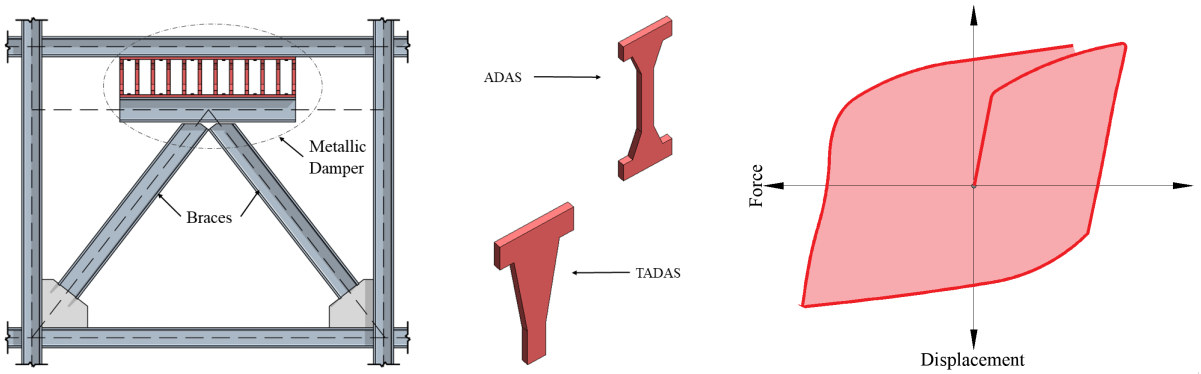

(a) Metallic dampers in a chevron frame (b) ADAS and TADAS (c) Hysteretic behavior curve

Figure 2.2: Passive control with metallic dampers.

According to Javanmardl et al. [35], metallic dampers are classified by material type into steel dampers, aluminum dampers, lead dampers, copper dampers, and shaped memory alloy dampers. Their principle is based on the concept of "added damping and stiffness", which was adapted to different shapes and techniques for joining the series of plates as shown in Figure 2.2.

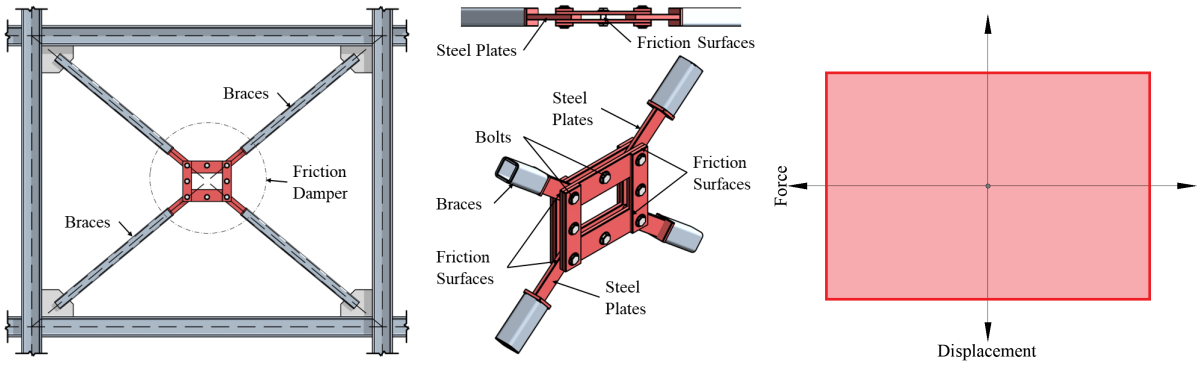

(a) Friction damper in X−shape braces (b) Friction devices system (c) Hysteretic behavior curve

Figure 2.3: Passive control with friction dampers.

Friction dampers use X-shape braces with additional plates in their midpoint. These plates are bolted together to allow rotation, so friction between plates is the dissipation mechanism (see Figure 2.3). This concept was introduced by Pall et al. in 1980 [36], followed by experimental tests carried out in concrete shearwalls to figure out a predictable and efficient sliding friction behavior, even for several load cycles, as a first approximation to the problem [37].

Several improvements were developed for the Pall friction damper (PFD) [38], updating its shape (Improve PFD), its connection type (slotted bolted connection), and even with new geometries (Symmetric/Asymmetric Friction connection). In reference [38], all these versions are explained in detail, while Figure 2.3 shows a version for friction dampers.

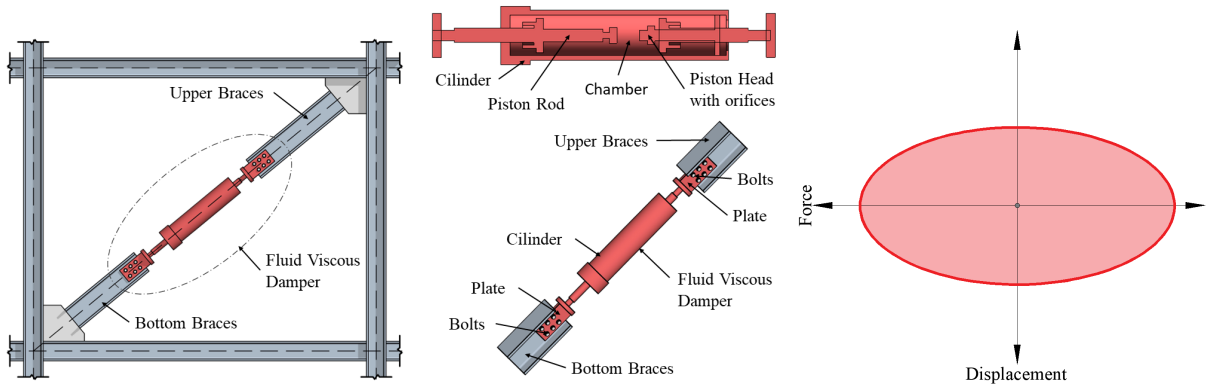

(a) Braces with fluid dampers (b) Viscous damper device (c) Hysteretic behavior curve

Figure 2.4: Passive control with fluid viscous damper.

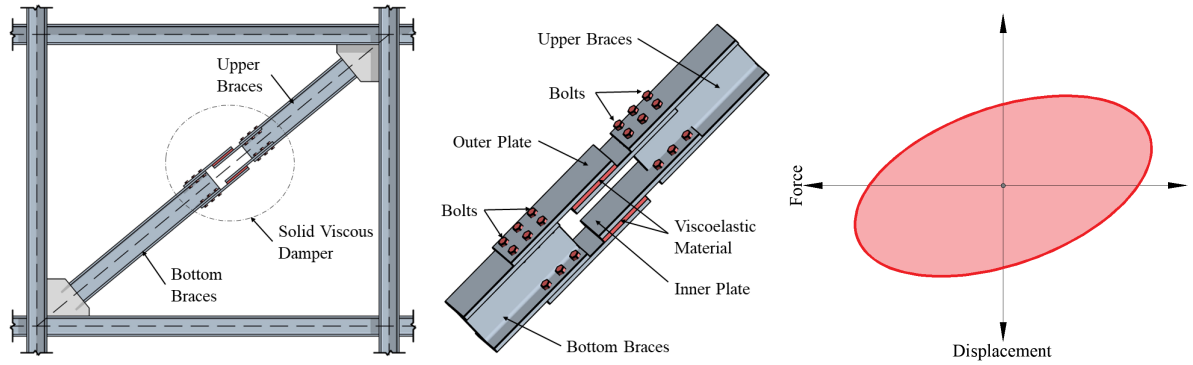

(a) Braces with viscoelastic material (b) Viscoelastic shear connection (c) Hysteretic behavior curve

Figure 2.5: Passive control with solid viscous dampers.

Fluid and viscous dampers shown in Figure 2.4 and 2.5 dissipate energy by friction and shear, respectively. According to Symans [34], when the fluid in a damper flows at

high velocities, there is friction between fluid particles and the damper head piston. The friction force releases energy dissipation in the form of heat. On the other hand, a solid material works under shear stress, developing heat as a dissipation mechanism. Both systems require an auxiliary frame to be adapted to the structure; the solution is usually the chevron frames or diagonal elements.

Finally, inertial controllers are based on device which apply counteract forces through the movement of an inertial mass in the opposite phase to the structural movement in order to mitigate the structural dynamic response. Within the civil engineering structures, Tuned Vibration Absorbers (TVAs) or TMDs are commonly used. In contrast to the dissipative strategies, inertial controllers are very effective in a narrow frequency band. The TMD system is explained in detail in Chapter 3.

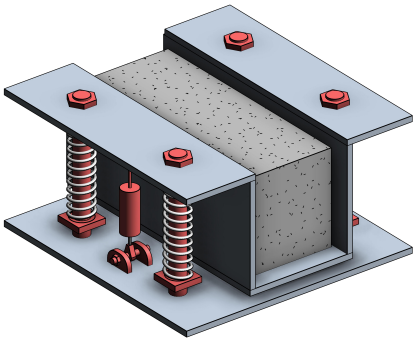

Figure 2.6: Passive TMD.

2.1.2 Active Control

Active control has been successfully used in electrical and control engineering, and its application was introduced in aerospace and mechanical engineering to control vehicle motion in real time; the idea is to improve its performance based on the measurement of external actions. Active control is characterized by the need of an actuator, which commonly requires a high external power source to induce the desired force on the structure or element to be controlled. According to Soong [39], active control in civil engineering appeared when Lev Zetlin, in 1965, came up with the idea of designing tall buildings and controlling the top response through cables attached at the bases with hydraulic jacks. This idea is based on Eugen Freyssinet's attempt in 1960 to control the behavior of tall buildings using prestressing tendons as control devices. In Zetlin's case, sensors are required to know the response at the top of the building; the information goes directly to the hydraulic jack that induces the necessary force.

The active control for civil structures can be directed in two configurations, the first one is known as closed-loop control or feedback control, where the input excitation (if it is possible) and the response of the structure are measured using sensors, and based on that information the actuator acts or not over the structure to improve performance. The

second one is known as open-loop control, in this case, the response of the structure is not taken into account and the actuator only acts based on the input excitation. Figure 2.7 shows the block diagram for the closed-loop and open-loop control.

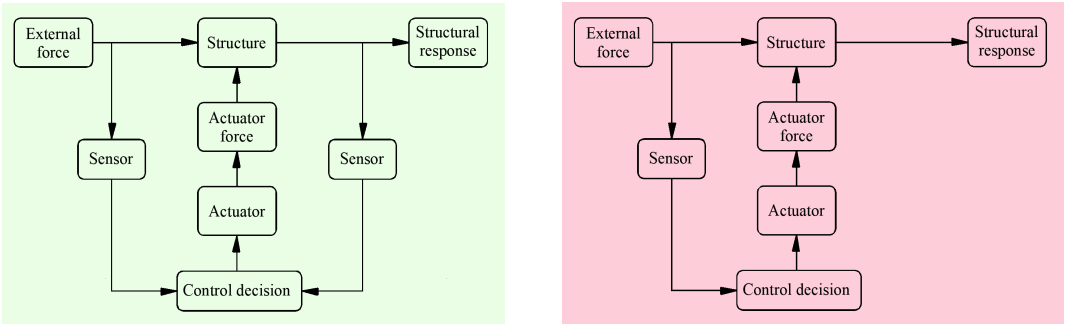

(a) Closed-loop control (b) Open-loop control

Figure 2.7: Block diagrams for control systems.

In Japan, design criteria for high-rise buildings must consider active or semi-active control, and its practical application has already become a trend. Active Mass Dampers (AMDs) that are not tuned for a specific natural frequency, Active Tuned Mass Dampers (ATMDs), in which the passive part is tuned to a specific vibration mode and it is accmpained by an actuator to induce force on the mass, and active inter-structure dampers system where a damper is connected between high-rise buildings have been put into practice as recorded in table 2.1.

Table 2.1: Active control applied to buildings in Japan [40].

Completion		**Building (Use, City)**	**Story**	**ht(m)**	**Control system**
2003	1	Shiodome Tower (hotel & office, Tokyo)	38	172	2 TMDs with AMD
	2	Shiodome Media Tower (hotel, office, Tokyo)	34	172	2 TMDs with AMD
2001	3	Hotel Nikko Bayside Osaka (hotel, Osaka)	33	138	2 ATMDs
	4	Dentsu Head Office (office, Tokyo)	48	210	2 TMD with AMDs
	5	Office Towers, Triton Square, Tower X	45	195	2 Active Interstruct
	6	Harumi Island (office store, Tokyo) Tower Y	40	175	Dampers
	7	Tower Z	34	155	(Max. force 340 kN)
	8	Cerulean Tower (hotel & office, Tokio)	41	184	2 ATMDs
	9	Osaka Airport Control Tower (control tower, Osaka)	5	69	2 ATMDs
1999	10	Century Park Tower (residence, Tokyo)	170	440	4 ATMDs
	11	Shinagawa Intercity Bldg. (office, Tokyo)	32	144	2 ATMDs
	12	JR Central Towers (Nagoya): Office Tower	51	245	2 ATMDs
	13	Hotel Tower	53	226	4 ATMDs
1998	14	Oita Oasis Tower (hotel, Oita)	21	101	2 ATMDs
	15	OTIS Shibayama Test Tower (elevator test, Chiba)	39	154	ATMD

Continues on next page

Table 2.1: Active control applied to buildings in Japan [40].

Completion		Building (Use, City)	Story	ht(m)	Control system
	16	Odakyu Southern Tower (hotel, office & store, Tokyo) CFT	36	151	2 ATMDs
	17	Kaikyo Messe Yume Tower (observation, Shimonoseki)	11	153	ATMD
	18	Bunka Gakuen (school, Tokyo) CFT	20	93	2 ATMDs
	19	Yokohama Bay Sheraton Hotel & Towers (hotel, Yokohama)	27	115	2 ATMDs
1997	20	The Itoyama Tower (hotel, Yokohama)	18	90	ATMD
	21	Nisseki Yokohama Bldg. (office, Yokohama)	30	133	2 ATMDs
	22	Herbis Osaka (hotel & office, Osaka)	40	190	2 ATMDs
1996	23	Rinku Gate Tower Bldg. (hotel, office & hall, Osaka)	56	225	2 ATMDs
1995	24	Osaka World Trade Center Bldg. (office,Osaka)	55	255	2 ATMDs
	25	Nissei Dowa Sonpo Phoenix Tower (office, store & hall, Osaka)	29	145	2 TMDs with AMD
	26	Plaza Ichihara (hall, Chiba)	12	58	2 ATMDs
1994	27	J City Tower (office, Tokyo)	24	100	2 ATMDs
	28	Shinjuku Park Tower	52	233	3 ATMDs
	29	Hamamatsu ACT Tower (hotel, office & store, Hamamatsu)	45	213	3 ATMDs
	30	Hirobe Miyake Bldg. (office & residence, Tokyo)	9	30	3 ATMD
	31	Hotel Ocean 45 (hotel, Miyazaki)	43	154	2 ATMDs
	32	MHI Yokohama Bldg. (office & store, Yokohama)	43	154	2 ATMDs
	33	Riverside Sumida Central Tower (office & residence, Tokyo)	33	134	2 AMDs
1993	34	NTT Cred Motomachi Bldg. (hotel & store, Hiroshima) SRC	35	150	ATMD
	35	Nishimoto Kosan Nishikicho Bldg. (office, Tokyo)	14	68	TMD with AMD
	36	Long Term Credit Bank (office, Tokyo)	21	130	ATMD
	37	Porte Kanazawa (hotel & office, Kanazawa)	30	131	2 AMDs
	38	Yokohama Landmark Tower (hotel, office & store, Yokohama) SRC	70	296	2 ATMDs
1992	39	Appluase Tower (hotel, office & theater, Osaka)	34	162	AMD
	40	ORC 200 Bay Tower (hotel, office & residence, Osaka)	34	162	2 ATMDs
	41	Kansai Airport Control Tower (control tower, Osaka)	5	86	2 ATMDs
1991	42	Sendagaya INTES (office, Tokyo)	11	58	2 AMDs
1989	43	Kyobashi Center Bldg. (office, Tokyo)	10	33	2 AMDs

2.1.3 Semi-active Control

Semi-active control requires a smart device operating independently or integrated into a passive system. The difference with an active device is the amount of external power supply needed for the smart device, which is much less for semi-active devices than for active devices. In addition, active control can induce force, whereas semi-active devices

cannot because the principle of operation is based on modifying their damping and/or mechanical properties in real time in order to achieve a grade of adaptability. Similar to active control, semi-active control uses sensors to perform feedback measurements and, with an appropriate algorithm, sends the correct signal to that semi-active device to modify its mechanical properties [41].

One version of a semi-active device used for controlling the seismic response in structures, changing its mechanical properties, was an Active Variable Stiffness (AVS) control, consisting of an instrument with a servo valve that allows oil flow from one cavity to another, this tipe of semi-active device change. The AVS is installed in a chevron-braced frame; if a high stiffness is required, the servo valve closes to prevent the oil flow. Otherwise, it opens to reduce pressure and release the device's movement [42]. Another version is the semi-active oil damper, which uses a servo valve to control oil flows, modifying its damping properties. In this cases, an On/Off control law where the damper piston stroke is measured to regulate supply and demand pressure is used to manage the response.

MR dampers and Electrorheological Dampers (ERs) are the most common semi-active devices that can modify damping properties. MR dampers are more useful in civil engineering applications due to their higher damping force than ERs. MR dampers are semi-active dampers with a fluid with suspended ferrous (iron) particles. Through a magnetic field, it is possible to control the rheological properties of the fluid in a few miliseconds in order to increase or decrease the viscosity or damping force of the damper. The magnetic field is generated through an external power source that supplies current to the damper coil. Thus, the current is modified by changing the supplied voltage, and damping properties can be changed almost in real-time. As mentioned, all semi-active devices can be integrated into passive devices, e.g., TMD or seismic isolation devices. Table 2.2 records some practical applications of semi-active control in buildings in Japan.

Table 2.2: Practical applications of semi-active control to buildings in Japan [40].

Completion		**Building (Use, City)**	**Story**	**ht(m)**	**Control system**
2004	1	Higashi Shinagawa Office Bldg. CFT (office, Tokyo)	23	100	28 oil dampers (on/off)
	2	Tokyo Prince Park Tower CFT (hotel, Tokyo)	30	105	66 oil dampers (on/off)
2003	3	Bandaijima Bldg. (hotel & office, Niigata) CFT	31	141	72 oil dampers (on/off)
	4	Tokyo Head Office Bldg., Matsushita Electric Works (office, Tokyo)CFT	25	120	38 oil dampers (on/off)
	5	Roppongi Hills Mori Tower (art museum, office & store, Tokyo)CFT	54	241	356 oil dampers (on/off)
	6	Shiodome Tower (hotel & office, Tokyo) CF,	38	172	88 oil dampers (on/off)

Continues on next page

Table 2.2: Practical applications of semi-active control to buildings in Japan [40].

Completion		Building (Use, City)	Story	ht(m)	Control system
	7	Toppan Forms Bldg. (office, Tokyo) CFT	19	100	27 oil dampers (on/off)
	11	Head Office Bldg., Nippon Express (office, Tokyo) CFT	28	137	60 oil dampers (on/off)
2001	12	Chuden Gifu Bldg. (office, Gifu)	11	56	42 oil dampers (on/off)
2000	13	House of Creation & Imagination Keio Univ. (school, Yokohama) SRC, CFT	7	29	8 oil dampers for base isolation
1999	14	Laxa Osaka (hotel & office, Osaka)	24	97	2 oil dampers for 2 TMDs (2TMDs: 330t)
1998	15	Kajima Shizuoka Bldg. (office, Shizuoka)	5	20	8 oil dampers (contin.)
1990	16	Kajima Shizuoka Bldg. (office, Shizuoka)	3	12	AVS (6 on/off devices)

2.2 Magnetorheological Dampers

MR dampers (Figure 2.8 illustrates an identification carried out in the lab) have attracted a great interest in controlling vibration in civil structures. Its use has been considered in vibration absorbers [43, 44, 45] and base isolation systems [46, 47, 48].

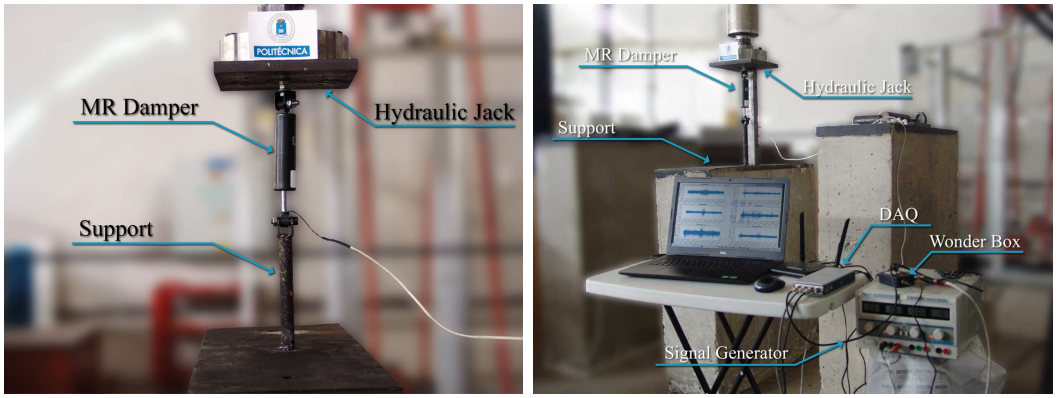

(a) (b)

Figure 2.8: **(a)** MR Damper of Lord Corporation, **(b)** instrumentation for the identification process.

Usually, the response of MR dampers incorporated in civil structures is analyzed through numerical models such as the Bingham model [49], Gamota and Filisk [50], Bouc-Wen [51], modified Bouc-Wen [52] and hyperbolic tangential model [53], where the Bingham and Bouc-wen models are the most used. The first is used for its simplicity in

reproducing a linear behavior, while the second reproduces its hysteretic behavior. However, these models do not consider the frequency or amplitude of the piston movement in the identification procedure, and for MR damper, these variables must be taken into account [54]. For the identification process (see Figure 2.8), the MR damper may subjected to a series of controlled excitations. A hydraulic jack applies a force on the MR damper, and the data acquisition Data Acquisition (DAQ) system saves the amplitude, force, and applied voltage on the MR damper in each time step. The wonder box transforms the controlled voltage applied into the current for the MR damper. The numerical models can be identified once the information is registered and analyzed in the post-process. The Bingham model, Bouc-Wen model, and Hyperbolic-tangential model are presented in the following sections:

2.2.1 Bingham Model

The Bingham model was studied by Stanway in 1985 [49] during the identification of ER effect in fluids. The preliminary model studied by Stanway considered both viscous damper and Coulomb friction damper. The ER fluid changes its viscosity when an electric potential is applied to it. According to Stanway, for a low electric potential, the ER behavior is similar to a viscous damper, while for a high electric potential, the material will solidify, and its behavior resembles Coulomb friction.

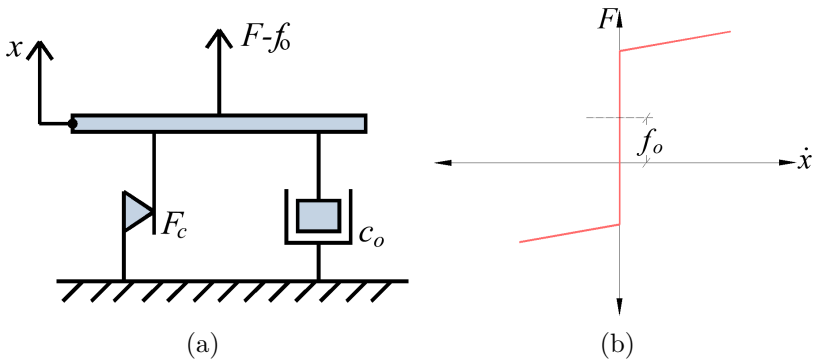

Figure 2.9: **(a)** Bingham model and **(b)** velocity-damping force curve.

According to Spencer [52], the force of the damper expressed through the Bingham model is given by:

$$F - f_0 = F_c \cdot sgn(\dot{x}) + c_0\dot{x}, \tag{2.1}$$

where F and f_0 are the restoring damper force and the offset force presented in the accumulator for the nonzero mean observed in the measured force, respectively. Parameter c_0 is the damping coefficient, F_c is the friction force related to fluid yield stress, $\dot{x}$ is the relative velocity of the damper, and when the velocity is zero, the Coulomb friction governates the damper. Figure 2.9 shows the mechanical model and the hysteretic behavior

for the Bingham model.

2.2.2 Bouc-Wen and Modified Bouc-Wen model

Bouc [51] introduced a model to describe the hysteretic response in non-linear systems. Wen et al. [55] improved this model to reproduce a variety of hysteretic patterns given the so-called Bouc-Wen model. The restoring damper force based on the Bouc-Wen model requires two equations 2.2 and 2.3, which depend on a set of variables [52], as follows:

$$F = \alpha z + c_0 \dot{x} + k_0 x, \tag{2.2}$$

$$\dot{z} = \delta \dot{x} - \beta |\dot{x}| z |z|^{n-1} - \gamma \dot{x} |z|^n. \tag{2.3}$$

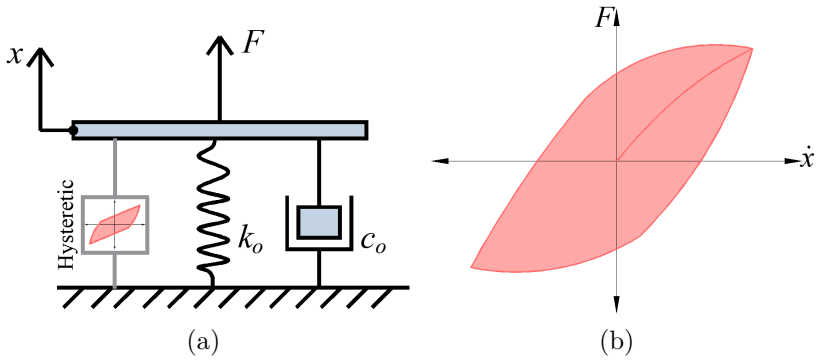

Figure 2.10: **(a)** Bouc-Wen model and **(b)** velocity-damping force curve [52].

The additional parameters k_0, z, α are the stiffness, the hysteretic variable, and the scaling factor. Variables $\dot{x}$, x are damper velocity and displacement. The parameters c_0, k_0, α, β, δ, z and n need to be identified. Figure 2.10 show the respectively mechanical model and the hysteretic behavior for the Bouc-Wen model.

Another version of the Bouc-Wen model proposed by Spencer, called "Modified Bouc-Wen model", was introduced to improve the non-linear force-velocity response of the Bouc-Wen model, which occurs when the magnitude of the acceleration and velocity are low, and when an opposite sign is present between them. In order to obtain the roll-off effect expected for low velocity in some experimental tests [52], a stiffness and an additional damping coefficient or dashpot in the classic model were included. Figure 2.11 shows the free body diagram of the Bouc-Wen modified system.

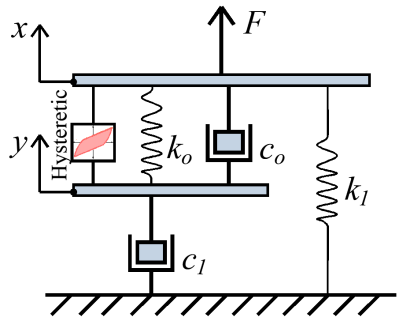

Figure 2.11: Modified Bouc-Wen model.

The damper force for this model is described by the following equations:

$$F = \alpha z + c_0(\dot{x} - \dot{y}) + k_0(x - y) + k_1 x + c_1 y, \tag{2.4}$$

$$\dot{z} = \delta(\dot{x} - \dot{y}) - \beta|\dot{x} - \dot{y}|z|z|^{n-1} - \gamma(\dot{x} - \dot{y})|z|^n. \tag{2.5}$$

$$\dot{y} = \frac{1}{c_0 + c_1}\left[\alpha z + c_0\dot{x} + k_0(x - y)\right], \tag{2.6}$$

the variable k_1 is the stiffness at high velocity, while c_0 and c_1 are viscous damping at low and high velocity, respectively. The variables $\dot{y}$ and y are, respectively, the velocity and displacement associated with the dashpot motion. The accuracy of the modified Bouc-Wen model is better than the basic Bouc-Wen model, but the number of variables brings challenges and increases the complex of the identification process.

2.2.3 Tangential model

To solve the complex identification process in modified and classic Bouc Wen models, Kwok et al. [53] proposed a model based on a hyperbolic tangent function to represent the hysteretic variable z. Although the hyperbolic tangent model requires fewer variables, it fits the velocity-damping force hysteresis curve better than the Bouc-Wen model, even in the velocity transition zone. Figure 2.12 shows mechanical model and the hysteretic behavior for the tangent model.

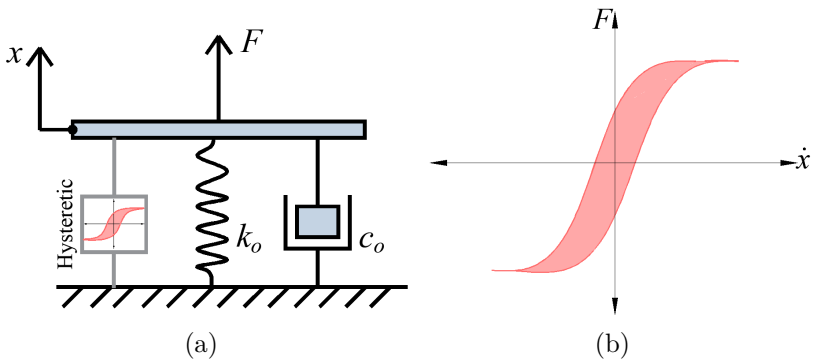

(a) (b)

Figure 2.12: **(a)** Hyperbolic tangent model and **(b)** velocity-damping force curve [52].

This model is represented by the following equations:

$$F = \alpha z + c_0 \dot{x} + k_0 x + f_0, \tag{2.7}$$

$$z = tanh(\beta \dot{x} + \delta sign(x)), \tag{2.8}$$

again, z is the hysteretic variable and β and δ are parameters to be identified.

Zhang et al. [56] proposed a method of identification of MR damper parameters based on the hyperbolic tangent model, taking into account excitation characteristics and current. The method introduces the term of maximum velocity (v_m), which is related to the amplitude and frequency of a sine excitation by the following equation:

$$v_m = c_0 \cdot (a \cdot f), \tag{2.9}$$

where a and f are the amplitude and frequency, respectively. Due to the fact that the frequency cannot be measured in real-time, the displacement, velocity, and acceleration are associated to obtain the v_m instantaneously as follows:

$$v_m = \sqrt{\dot{x}^2 - x \cdot \ddot{x}}. \tag{2.10}$$

In this sense, the parameters (c_0, α, β, δ) can be identified as dependent of the maximum velocity v_m and voltage/current V/I.

2.3 Control Strategies

The MR damper has been used and considered for several civil or structural engineering applications involving vibration control [57, 58, 59, 60]. To achieve a semi-active control strategy, the MR damper has to be continuously controlled. In order to achieve this goal, a proper control strategy is required to manage the input voltage/current on the control device.

Different strategies to control the response of semi-active devices, mainly for MR dampers, have been developed. Some of them are based on force control and other on phase control strategies. The following sections briefly describe some of the most common strategies adopted.

2.3.1 Proportional-Integral-Derivative Control

The force Proportional-Integral-Derivative (PID) control adjusts the force, taking into account the error between the desired and actual force. The PID consists of three elements: a proportional gain K_P, integral gain K_I, and derivative gain K_D. The gain K_P amplifies the error, ensuring the output follows the desired reference. The gain K_I makes the tracking error equal to zero during stationary-state conditions. The gain K_D adds damping to the closed-loop structure control output response as the input variable changes [61].

The SAMCO guide [62] defines the PID control as a parallel system through a Transfer Function (TF). Figure 2.13a shows a parallel PID block diagram including an inverse model of nonlinearity (NL^{-1}), which in this case, compensates the MR damper nonlinearities, while Figure 2.13b shows the Bode diagram of PID with a low pass filter, which is introduced to avoid instablities coming for high-frequency components.

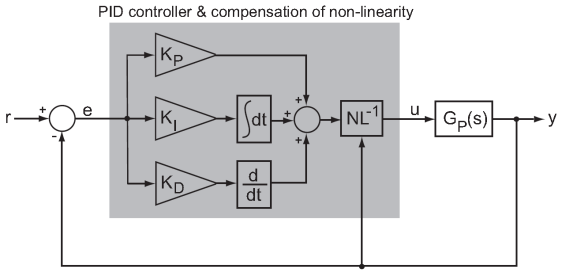

(a) Structure of parallel PID controller with inverse plant model NL^{-1}

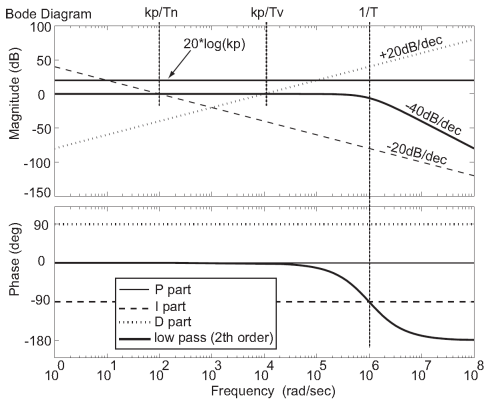

(b) Bode diagram of P, I, D elements, and of low-pass filter of 2nd order

Figure 2.13: PID Controller [62].

The parallel PID TF can be expressed by the following equation:

$$G_{PID}(s) = K_P + \frac{K_I}{s} + K_D \cdot s. \tag{2.11}$$

Non-linearity (NL^{-1}) shows in Figure 2.13a works by compensating for the non-linear effects of the MR damper within the control algorithm, where the non-linear relationship between actuator input (voltage/current) and actuator output (force, strain, displacement) must also be considered in $G_P(s)$. In addition, a low pass filter is added to suppress measurement noise in the PID to achieve the "roll-off"behavior of the controller (Figure 2.14), thus, improving the stability of the control system. The TF equation for the PID with the low-pass filter is given by:

$$G_{PID-rf}(s) = K_P + \frac{K_I}{s} + K_D \cdot s \frac{1}{(T \cdot s + 1)^n} \quad (n \geq 1), \tag{2.12}$$

where the variable $1/T$ is the cut-off frequency as Figure 2.13b shown, and subindex rf means roll-off.

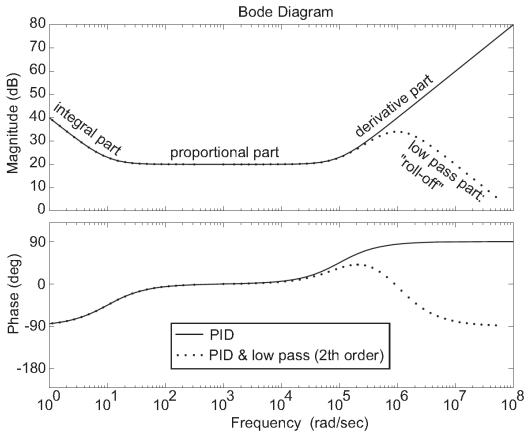

Figure 2.14: Bode diagram of a parallel PID controller with low pass filter of 2nd order including the roll-off part [62].

2.3.2 Fuzzy Logic Control

Fuzzy logic control is a control strategy used for complex and uncertain systems. The fuzzy logic control works as an artificial intelligence-based technique, which controls the system without considering physical models Fuzzy logic works by executing rules that correlate the controller inputs and the desired outputs. [63].

As Figure 2.15 shows, the architecture of a fuzzy logic controller is composed of Fuzzification, inference engine (the execute of the rules of the controller), defuzzification, and rule base.

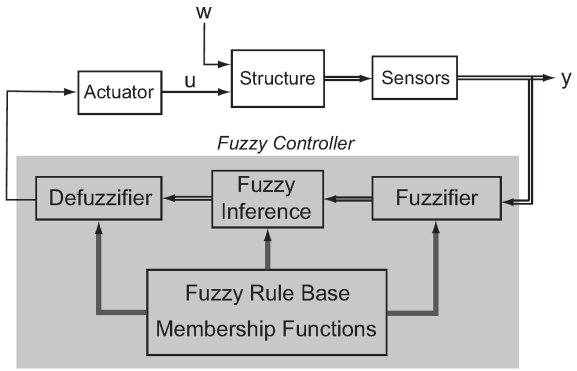

Figure 2.15: Structure of a fuzzy controller [62].

The fuzzification step transforms the inputs and outputs from crisp values to fuzzy linguistic values. Then, a set of if-then rules are evaluated. The fuzzy rule base is created to relate the inputs and outputs. These rules are considered to define the output for a specific set of inputs. Finally, the output variable is transformed from a fuzzy quantity to a non-fuzzy discrete value.

2.3.3 Model predictive conrol

This strategy is based on predicting the system response at a future time step to minimize an objective function. However, the time delay in this strategy could be a problem if the system to control is complex due to the time required in the control process since the model has to be run between each time step.

In reference [64], the predictive control is applied to a discrete system with an MR damper control device subjected to seismic excitations. For this case, the optimal control is obtained based on an actual past control and an actual measurement response state. It means the past state of the MR damper at time (t) is considered in the response state at time (t+1), and the object function is evaluated. If the objective function is not minimized, the MR damper shall change its state for the next step at (t+1). The main drawback of these strategies is that a precise model for a broad frequency and amplitude band is required and, at the same time, the model should be as simple as possible in order to be integrated in the real-time control chain.

2.3.4 Phase Control

Phase-contro-based strategies aim to control the relative movement between the controller and the structure to be controlled. These are non-model-based strategies in which the complete state of both controller and structure is not needed for their application. Another important advantage is that the non-linear behavior of the damper does not affect the realization of control law. The first phase control was introduced in the power flow theory proposed by Soong and Dargush [65] to control the phase of a TMD. Actually, in resonance, for a low-damped TMD (assuming the TMD damping is negligible) the phase between the relative displacement of the inertial mass and the structure displacement is 90º. Therefore, the transmitted force from the TMD and the excitation force are 180º delay.

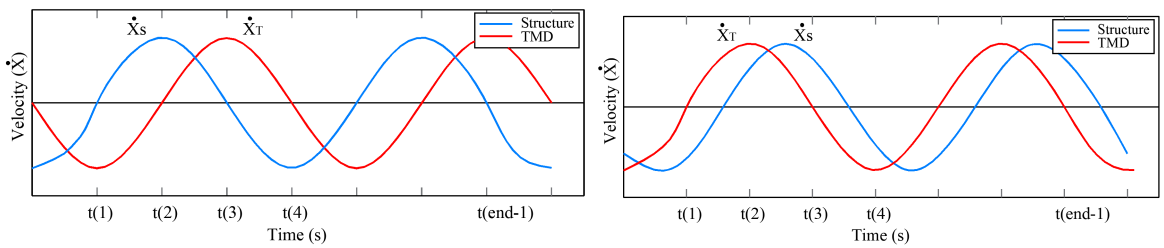

(a) Tuned cases.

(b) Detuned cases.

Figure 2.16: Tuned and detuned situation for a phase control.

Figure 2.16 shows the velocity response for a structure and the relative velocity of a TMD for a tuned and detuned case. When the velocity of the structure is zero, and the TMD velocity is maximum, the TMD the TMD is tuned (Figure 2.16a). However, as the

phase relationship is lost, the TMD loses effectiveness and is considered detuned (Figure 2.16b).

Koo et al. [66] used the skyhook and groundhook concepts [67] to define **On-Off controllers** for TMD. Even though the On-Off is not initially defined as a phase control, the controller analyzes the response in terms of the velocity of the structure and relative velocity of the control device. The control law used in a STMD analyzes the velocity $\dot{x}_1$ and relative velocity $\dot{x}_{12}$, where $\dot{x}_1$ is the velocity of the main structure, and $\dot{x}_2$ is the velocity of the TMD. Koo defines the control strategy in terms of velocity as a Velocity-Based Groundhook (VBG) as follows:

$$\begin{aligned} \dot{x}_1 \cdot \dot{x}_{12} \geq 0 &\rightarrow \text{On State}, \\ \dot{x}_1 \cdot \dot{x}_{12} < 0 &\rightarrow \text{Off State}, \end{aligned} \tag{2.13}$$

The VBG can be analyzed in terms of displacement through the Displacement-Based Groundhook (DBG) as follows:

$$\begin{aligned} x_1 \cdot \dot{x}_{12} \geq 0 &\rightarrow \text{On State}, \\ x_1 \cdot \dot{x}_{12} < 0 &\rightarrow \text{Off State}, \end{aligned} \tag{2.14}$$

The variable x_1 is the displacement of the main structure, while On-Off states correspond to the application of minimum and maximum voltage/current on the MR Damper. The On-Off control is known in the control theory as the Bang-bang control [68] since switches abruptly between two states.

Furthermore, Koo also presents a **linear control**, which changes the damping level between the On and Off states. The control law may be formulated as velocity or displacement feedback as follows:

$$\begin{aligned} c_{controllable} &= \frac{G \cdot \dot{x}_1}{\dot{x}_{12}}, \\ c_{controllable} &= \frac{G \cdot x_1}{\dot{x}_{12}}, \end{aligned} \tag{2.15}$$

in which G is a control gain.

Lineal control could produce overload in the MR damper because the control has no boundaries. Hanagan [69] proposed a **nonlinear control** for active control of floor vibrations, which prevents the overload effect, that is, a velocity feedback control plus a saturation rule. This nonlinear control is given by:

$$\text{Voltage command} = \begin{cases} v_{max} & \text{for} \quad \dot{x}_s > \frac{v_{max}}{G}, \\ G \cdot \dot{x}_s & \text{for} \quad \frac{v_{min}}{G} < \dot{x}_s < \frac{v_{max}}{G}, \\ v_{min} & \text{for} \quad \dot{x}_s < \frac{v_{min}}{G}, \end{cases} \tag{2.16}$$

where v_{min} and v_{max} are the limits of the voltage to avoid the overloading effect.

Nonlinear control requires a previous evaluation to obtain the gain (G). This G is obtained and adapted for a specific set of conditions. However, if these conditions change, the nonlinear control will not be effective and could adopt a behavior similar to an On-Off control.

A **continuous control** offers a solution for the previous evaluation to define G, transforming it variable from constant to variable in time. Nyawako et al. [70] defines continuous variable gain as follows:

$$G = \frac{v_{max}}{|\dot{x}_s|_{T,max}}, \tag{2.17}$$

$|\dot{x}_s|_{T,max}$ is the maximum absolute velocity in a previous period (T). In this sense, gain G will change over time adapting its value based on the actual response of the system to be controlled.

This thesis will propose phase controllers for MR dampers adapted to TMDs and FPSs. The concept of groundhook control will be used and adapted to these two problems. Particularities of each one, together with additional elements for the control chain, will be considered to improve the applicability of the controllers.

Chapter 3

Phase Control in the Inertial Systems

This chapter introduces in section 3.1 a brief chronology of the TVA device, known as TMD, focusing on its discovery and applications as a passive control device. Section 3.2 describes the basic TMD and the different configurations studied. In 3.2.2 the enhancement of the TMD adding an ideal semi-active device is introduced, while the real semi-active device is introduced in 3.4. Finally, experimental tests are carried out in section 3.5 studying the performance of the STMD with a phase control law, an On-Off control and a continuous control.

3.1 Introduction

One of the most popular strategies to mitigate the vibration in structures is the TMD, which was invented by Hermann Frahm in 1911 to damp the resonance vibration under certain periodic impacts [71]. The strategy consists in attach an auxiliary body to the main vibration body. The auxiliary body begins to vibrate due to the vibration induced by the main body. The resonance effects of the main body are attenuated by the relative movement of the auxiliary body, which acts with a delay of approximately 90° when the fundamental frequency of the auxiliary body is close to the resonance frequency of the main body.

According to Yang [72], this type of device is very useful for its mechanical simplicity, and great cost-effectiveness ratio, it has also been widely studied under harmonic loads and successfully installed in recognized civil engineering projects, such as Taipei 101 Tower in Taiwan, the Millennium Bridge in London, among others.

Den Hartog [73] presented the equations of motion of a damped and undamped dynamic vibration absorber, also known as a TMD. Hartog developed a series of relationships among external force, stiffness, and mass of the main body and TMD, which are used to cancel the resonance effect on the main body, optimizing the parameters of the TMD. This work has been the most important reference used for the study of TMD implementation, including the study of its effectiveness under different vibration sources.

For example, Wang et al. [74] studied the vertical vibration induced by the pedestrian effect in long-span steel footbridges with TMD. Liu et al. [75] have evaluated the response of a cantilevered floor with human-induced vibration, considering a single pedestrian and groups of pedestrians, and a TMD as a passive control device. Troncoso et al. [76] have carried out a numerical assessment of pedestrian-induced vibration for a wide range of girder footbridges, where the vibration attenuation is achieved through a TMD.

On the other hand, TMD has been analyzed under wind and earthquake effects. Xu et al. [77] developed an experimental test and theoretical analysis to assess the capacity of a TMD to suppress wind-induced vibrations in tall buildings. Elias and Matsagar [78] have examined the wind response of tall buildings considering a TMD on different floors. Each TMD position was selected considering the modal shape of the first modal frequency.

Lu et al. [79] have developed an experimental and analytic study to control the vibration induced by seismic events on a five-story steel frame using a particular TMD. Salví et al. [80] have evaluated the soil-structure interaction effects for the design of the optimal TMD, considering that this effect could affect the tuning of the TMD due to strong motion earthquakes. Pinkaew et al. [81] have analyzed the use of TMD to control structures under seismic ground motion, revealing that the TMD cannot reduce the drift once the yielding is present, but is possible to reduce the damage to the structure. Other researchers have focused on optimizing the TMD for a specific situation, e.g. Shi et al. [82] proposed a new optimization method base on an artificial fish swarm algorithm for TMD attached to the pedestrian bridge. Greco et al. [83] have proposed one optimization criterion for TMD in buildings subjected to low-moderate seismic actions, where a multi-objective optimization is carried out by the non-dominated sorting genetic algorithm. Bekdas and Nigdeli [2011] proposed the optimum parameters of TMD under seismic action, which have been found through and harmonic search, where the peak displacement values and acceleration transfer function are the optimization criteria. In the next section a detailed introduction of the passive systems is mentioned, including each version or generation created, and their main characteristics

3.2 Inertial mass dampers

The TMD is a control device that can reduce the vibration level of resonance vibration when it is attached to a structure. This effect is achieved because the movement of TMD has a delay of 90° concerning the movement of the main structure. When this delay is presented the behavior is known as the tuning effect. Otherwise, the effect is known as the detuning effect, and the cancellation of vibration on the structure is not effective. Den Hartog [73] studied a system of two degrees of freedom without damping under a harmonic force to figure out the optimal equations that reproduce the correct tuning on the TMD. The equations of motion for this system are presented below:

$$m_t\ddot{x}_t + k_t(x_t - x_s) = 0 \quad \rightarrow (\text{TMD}), \tag{3.1}$$

$$m_s\ddot{x}_s + k_s x_s - k_s(x_t - x_s) = F_0 \sin(\omega t) \quad \rightarrow (\text{Structure}), \tag{3.2}$$

where the parameters m and k are the generalized mass and modal stiffness. The parameters $\ddot{x}$ and x are the acceleration and displacement, while the sub-indexes s and t refer to structure and TMD respectively.

Forced vibration for the system above is given by:

$$\begin{aligned} x_t = a_t \sin(\omega t) \quad &\rightarrow a_t = \frac{x_t}{\sin(\omega t)}, \\ x_s = a_s \sin(\omega t) \quad &\rightarrow a_s = \frac{x_s}{\sin(\omega t)}, \end{aligned} \tag{3.3}$$

where the a_s and a_t are the amplitude of the mass of the structure and TMD, respectively. The second derivative of the expressions in (3.3) takes the form of "$\ddot{x}_i = -a_i\omega^2 \sin(\omega t)$". If the acceleration $\ddot{x}_i$ and displacement x_i are replaced in equations (3.1) and (3.2) in terms of amplitude a_i and divide by $\sin(\omega t)$, the equations are the following:

$$a_t(k_t - m_t\omega^2) - a_s k_t = 0, \tag{3.4}$$

$$a_s(k_s + k_t - m_s\omega^2) - a_t k_t = F_0. \tag{3.5}$$

Furthermore, these equations can be expressed in terms of angular frequency when are divided by k_s and k_t, respectively. Additionally, the expression $x_i = P_0/k_i$, $\omega_i = k_i/m_i$ and mass ratio $\mu = m_t/m_s = k_t/k_s$ are identified in the solving process, resulting in the following equations:

$$a_t\left(1 - \frac{\omega^2}{\omega_t^2}\right) = a_s \quad \rightarrow a_t = \frac{a_s}{\left(1 - \frac{\omega^2}{\omega_t^2}\right)} \tag{3.6}$$

$$a_s\left(1 + \mu - \frac{\omega^2}{\omega_s^2}\right) - a_t\mu = x_s. \tag{3.7}$$

Finally, replacing the left equation on (3.6) in equation (3.7), the equation of the TF between the amplitude of TMD and the displacement is obtained as follow:

$$\frac{a_t}{x_s} = \frac{1}{\left(1 - \frac{\omega^2}{\omega_t^2}\right)\left(1 + \mu - \frac{\omega^2}{\omega_t^2}\right) - \mu}, \tag{3.8}$$

while if the right equation on (3.6) is replaced in equation (3.8), the TF for the amplitude of the structure is expressed by the following equation:

$$\frac{a_s}{F_0} = \frac{\left(1 - \frac{\omega^2}{\omega_t^2}\right)}{\left(1 - \frac{\omega^2}{\omega_t^2}\right)\left(1 + \mu - \frac{\omega^2}{\omega_t^2}\right) - \mu}. \tag{3.9}$$

According to the equation (3.9), the amplitude a_s will be zero when the numerator is zero. It occurs when ω_f is equal to the angular frequency (ω) of the harmonic force. As the resonance of the structure happen when the frequency ω is equal to ω_s, it is possible to state that the amplitude a_s will be zero when $\omega_t \equiv \omega_s$, in this way, the TMD will be tuning.

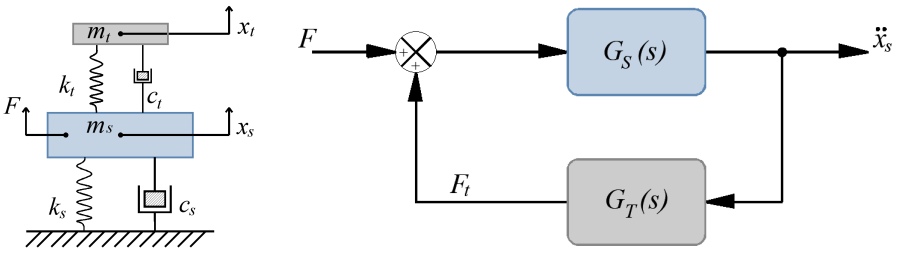

(a) (b)

Figure 3.1: (**a**) Free body diagram for a SDOF structure, (**b**) Block diagram of the structure with TMD system.

Based on the previous concept, Den Hartog has defined the damping coefficient ζ_{opt} and frequency ratio f_{opt} of the TMD as a function of the mass ratio μ. In this sense, to achieve the perfect tuning on a damping system, the optimal equations are:

$$f_{opt} = \frac{1}{1+\mu}, \tag{3.10}$$

$$\zeta_{opt} = \sqrt{\frac{3\mu}{8(1+\mu)}}. \tag{3.11}$$

The equations of motion for a damped two-degree-of-freedom system are given by:

$$m_t\ddot{x}_t + c_t(\dot{x}_t - \dot{x}_s) + k_t(x_t - x_s) = 0, \tag{3.12}$$

$$m_s\ddot{x}_s + c_s\dot{x}_s + k_s x_s - c_t(\dot{x}_t - \dot{x}_s) - k_t(x_t - x_s) = F, \tag{3.13}$$

where damping is defined as $c = 2m\zeta(2\pi f)$ and the stiffness as $k = m(2\pi f)^2$. For the case of the TMD, the damping coefficient is $\zeta = \zeta_{opt}$, while the frequency is $f_t = f_s \cdot f_{opt}$, with f_s equal to the frequency of the main structure.

The system of structure with TMD shows in figure 3.1 can also be solved in the Laplace domain through the TF. Hence, it is necessary to define the force F_t as the force transmitted by the TMD to the structure. Thus, the equations of motion can be expressed as:

$$-m_t\ddot{x}_t = F_t \longrightarrow c_t(\dot{x}_t - \dot{x}_s) + k_t(x_t - x_s) = F_t, \tag{3.14}$$

$$m_s\ddot{x}_s + c_s\dot{x}_s + k_s x_s = F + F_t, \tag{3.15}$$

and the corresponding TFs are given by:

$$G_T(s) = \frac{F_t(s)}{s^2 X_s(s)} = \frac{-m_t(sc_t + k_t)}{s^2 m_t + sc_t + k_t}, \tag{3.16}$$

$$G_S(s) = \frac{s^2 X_s}{F(s) + F_t(s)} = \frac{s^2}{s^2 m_s + sc_s + k_s}, \tag{3.17}$$

where $s = j\omega$ is the Laplace variable with ω being the angular frequency (rad/s).

Figure 3.2 shows the magnitude and phase for a structure with and without control, where the control is provided by the TMD. The TMD is analyzed under two principal situations, "Tuned"and "Detuned". In the case of the TMD tuned, the optimal equation mentioned previously have been used, while that TMD detuned is considered modifiying the frequency of the TMD with an upper and lower value concerning to the frequency of the structure.

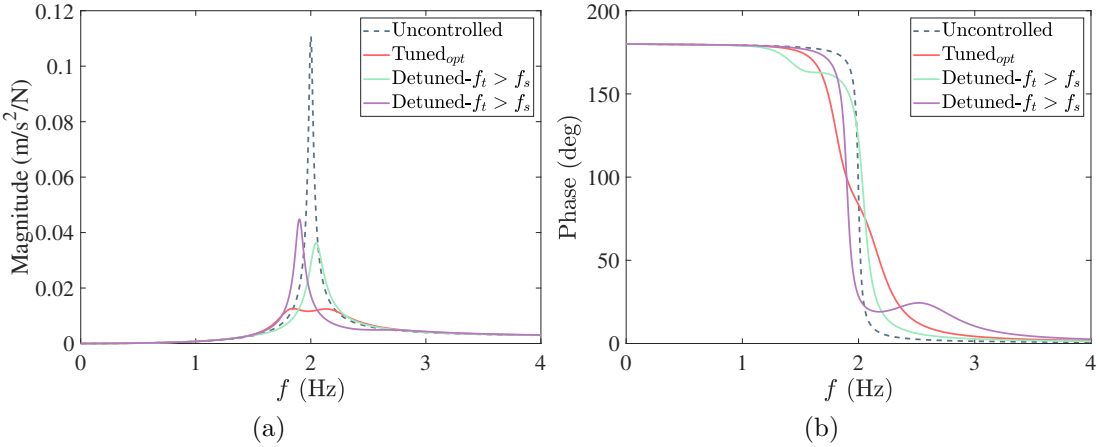

Figure 3.2: (**a**) Magnitude in acceleration/force, and (**b**) phase in degrees of the FRF for structure with TMD.

3.2.1 Multiples inertial mass dampers

Several alternatives to achieve a major width band of control through TMD have been studied, and one of them is the use of Multiple Tuned Mass Damper (MTMD). In this case, the structure is considered as a system of multiples degree of freedom, the mathematical problem is a little bit more complex and has to be solved depending on the configuration adopted. The main configurations, parallel and series are explained as follow:

MTMD Parallels
An MTMD in parallel consists of a series of TMD attached to the main structure, where the transfer force of each TMD is applied directly to the main structure (see figure 3.3). The parallel configuration allows each TMD to have its own natural frequency. In this way, each TMD will respond under the excitation frequency of the main structure.

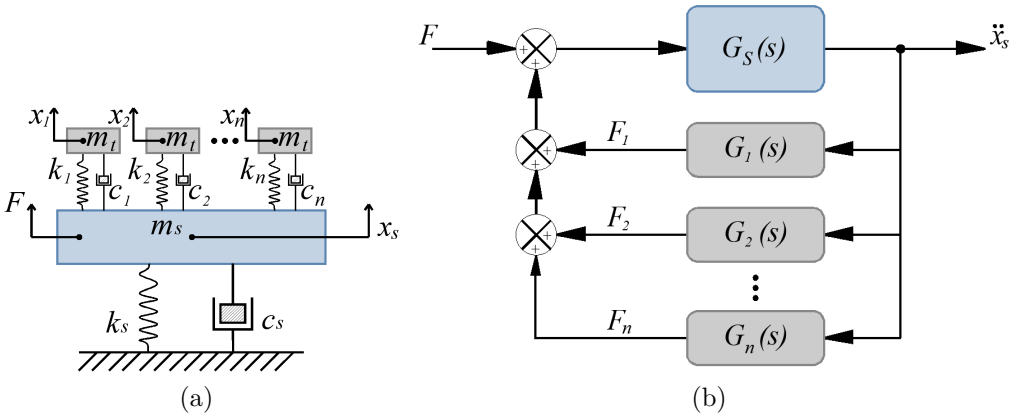

Figure 3.3: (**a**) Free body diagram for a MDOF structure with MTMD in parallel, (**b**) Block diagram of the structure with MTMD in parallel.

The following equations of motion describe the system of a structure with MTMD in parallel, where equation 3.18 correspond to the equation of motion for each TMD.

$$m_i\ddot{x}_i + F_{ti} = 0, \rightarrow F_{ti} = c_i(\dot{x}_i - \dot{x}_s) + k_i(x_i - x_s), \tag{3.18}$$

$$m_s\ddot{x}_s + c_s\dot{x} + k_s x_s - \sum_{i=1}^{n} F_{ti} = F, \tag{3.19}$$

where the sub-index i is the identification for each TMD and n is the total number of TMD.
The TF for MTMD in a parallel system, TMDs and structure, can be expressed in the Laplace domain as follows:

$$G_i(s) = \frac{X_i(s)}{X_s(s)} = \frac{(sc_i + k_i)}{(s^2m_i + c_i + k_i)}, \tag{3.20}$$

$$Gs_(s) = \frac{X_s(s)}{F(s)} = \frac{1}{\left((s^2m_s + sc_s + k_s) + \sum_{=1}^{n}(sc_i + k_i) - \sum_{i=1}^{n}\frac{(sc_i+k_i)^2}{(s^2m_i+sc_i+k_i)}\right)}. \tag{3.21}$$

MTMD Series
An MTMD configured in series consists of a system of several TMD joined one behind the other, where the control force on the structure is transferred through the first TMD, but its behavior is influenced by the response of the other TMD (see figure 3.4). In this configuration, each TMD needs an adequately tuned frequency to achieve the correct behavior of the control. Otherwise, the response of each TMD will be canceled between them without transferring the desired control force to the structure.

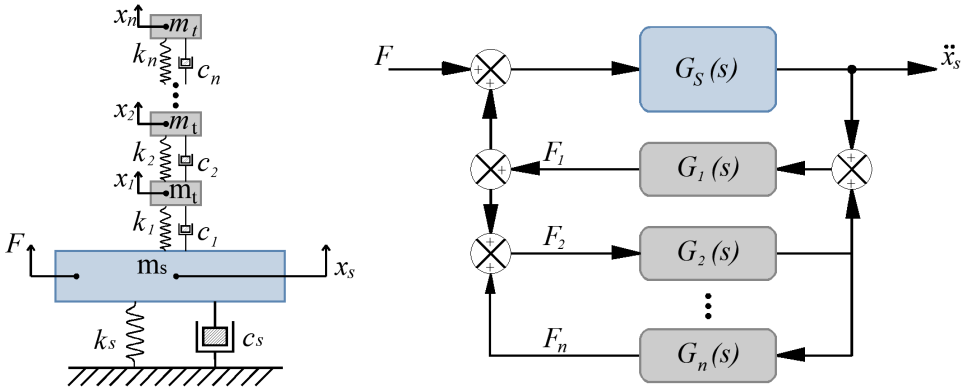

Figure 3.4: (**a**) Free body diagram for a MDOF structure with MTMD in series, (**b**) Block diagram of the structure with MTMD in series

The following equations of motion describe the last TMD in equation (3.22), intermediate TMD in equation (3.23), and structure in equation (3.24) as follow:

$$m_n\ddot{x}_n + F_{t(n)} = 0, \tag{3.22}$$

$$m_i\ddot{x}_i + F_{t(i)} - F_{t(i+1)} = 0, \tag{3.23}$$

$$m_s\ddot{x}_s + sc_s\dot{x}_s + k_s x_s - F_{t(1)} = F. \tag{3.24}$$

The TF for the MTMD in series is more complex to detail than MTMD in parallel if the number of TMDs is considerable. Hence, the variables N_r (numerator) and D_r (denominator) will be introduced, and the sub-index r will take the identification for each TMD analyzed. In this way, equation (3.25) is the TF for the last TMD, equation (3.26) is the TF for intermediate TMD, and equation (3.27) is the TF for the structure.

$$\frac{X_n(s)}{X_{n-1}(s)} = \frac{(sc_n + k_n)}{(s^2m_n + sc_n + k_n)} \Rightarrow \frac{N_n}{D_n}, \tag{3.25}$$

$$\frac{X_i(s)}{X_{i-1}(s)} = \frac{N_i}{(D_i + N_{i+1}) - \frac{(N_{i+1})^2}{(D_{i+1}+N_{i+2}) - \cdots - \frac{(N_n)^2}{D_n}}}, \tag{3.26}$$

$$\frac{X_s(s)}{F(s)} = \frac{1}{(D_s + N_1) - \frac{(N_1)^2}{(D_1+N_i) - \frac{(N_i)^2}{(D_i+N_{i+1}) - \cdots - \frac{(N_n)^2}{D_n}}}}. \tag{3.27}$$

Figure 3.5 shows the FRF for the MTMD system configured in parallel and series for 3 different frequencies of the structure, which pretend to assess the response under detuned effects, where the MTMD achieve less vibration level than the classic TMD.

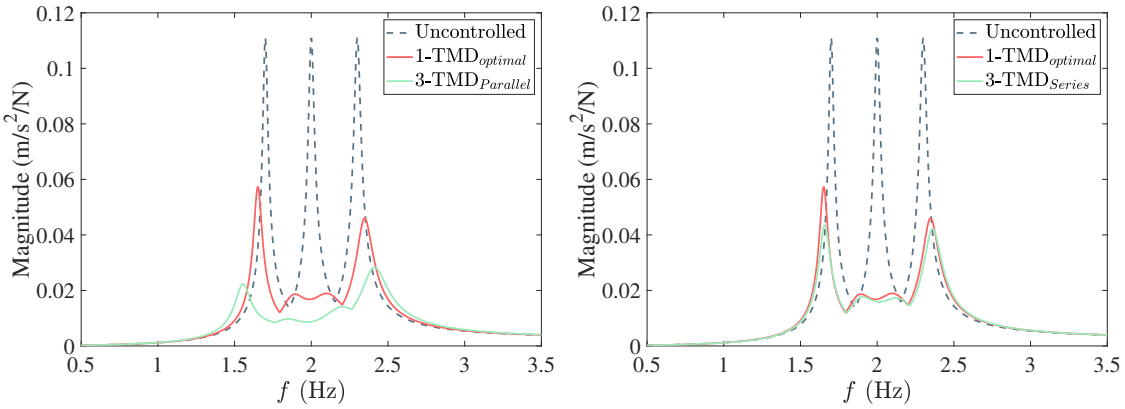

Figure 3.5: (**a**) FRF for the system with MTMD in parallel, (**b**) FRF for the system with MTMD in series.

3.2.2 Semi-active inertial mass damper

The STMD is an improvement of the TMD, it means that the new device is composed of a passive component and a semi-active component.The viscous damper used on the TMD is replaced with a semi-active device, which usually is a magnetorheological damper. This device can modify its properties in real time to provide a more or less damping force on the control system. The equations of motion 3.12 and 3.13 defined for the Structure-TMD system in section 3.2 are updated to the equations 3.28 and 3.29, respectively, to modify the viscous damper to a semi-active damper. The equations of motion considering a semi-active damper are given by:

$$m_t\ddot{x}_t + c_t(t)(\dot{x}_t - \dot{x}_s) + k_t(x_t - x_s) = 0, \tag{3.28}$$

$$m_s\ddot{x}_s + c_s\dot{x}_s + k_s x_s - c_t(t)(\dot{x}_t - \dot{x}_s) - k_t(x_t - x_s) = F, \tag{3.29}$$

where the previous variable c_t now is $c_t(t)$ due to its response change at each time step. The behavior of the semi-active damper could solve the detuning problem for the passive TMD. If the STMD is detuning with respect to the vibration of the structure, the semi-active damper can block the motion of the inertial mass of the control device increasing the damping force, and release it again when the phase between structure and that inertial mass is 90º achieving the tuned effect for the STMD.

3.3 Phase control law for semi-active inertial systems

According to Barrera-Vargas [84], the right manner to use a semi-active damper requires introducing a control law. Different control laws have been studied, some of them based on the knowledge of the whole system state. Zhang et al. [85] proposed a robust algorithm that combines a linear quadratic regulator and a nonlinear robust compensator to control

the oil pressure in the cavity of a friction pendulum system. Gu et al. [86] used an optimal neuro-fuzzy logic control to modify the stiffness of a magnetorheological elastomer. However, the phase control approach is geared to allow the practice implementation. Koo et al. [66] proposed a control law for the application within STMDs, which depends on the phase between the displacement of the main structure and the relative velocity between the structure and the TMD inertial mass. Later, Moutinho et al. [87] modified Koo's control law, substituting the displacement with the acceleration and neglecting the structure's velocity concerning the TMD mass velocity.

The control law employed herein consist of an On-Off phase control, which take into account the acceleration of the structure and relative velocity between the structure and the inertial mass. Figure 3.6 shows the different states of an SDOF structure controlled by an STMD in order to illustrate how the phase control works.

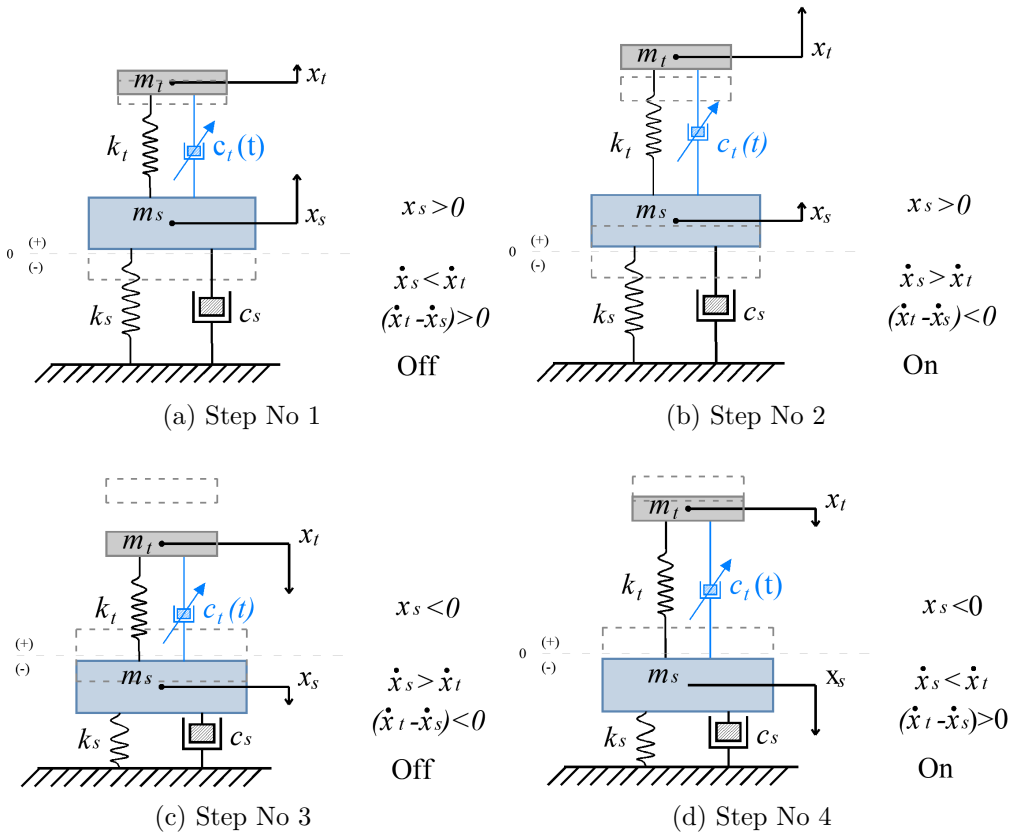

(a) Step No 1 (b) Step No 2

(c) Step No 3 (d) Step No 4

Figure 3.6: (**a**) and (**b**) show the phase control logic for upward motion with respect to an equilibrium state. (**c**) and (**d**) show the phase control logic for downward motion with respect to an equilibrium state.

The phase control can be expressed by the following inequations:

$$
\begin{aligned}
&\ddot{x}_s \cdot (\dot{x}_t - \dot{x}_s) \leq 0 \quad \Rightarrow \quad c_t(t) = c_{min} \quad \text{(normal functioning)}, \\
&\ddot{x}_s \cdot (\dot{x}_t - \dot{x}_s) > 0 \quad \Rightarrow \quad c_t(t) = c_{max} \quad \text{(blocking functioning)}, \\
&\text{s.t.: } |c_t(t) \cdot (\dot{x}_t - \dot{x}_s)| \leq F_{sat},
\end{aligned}
\tag{3.30}
$$

in which x_s has been substituted by $\ddot{x}_s$ (and changing the inequation sign of Figure 3.6) and a viscous semi-active damper with force saturation is assumed. The parameters c_{min} and c_{max} are the minimum and maximum damping coefficients, respectively, and F_{sat} is the saturation value for the force.

In order to evaluate the effectiveness of the STMD using a phase control law, a previous work has been developed in [84], and it is presented in Sections 3.4 and 3.5.

3.4 Performance assessment of the semi-active inertial system with linear viscous damper

The new trends in civil engineer aims to the uses of lightweight materials, such as Fiber-Reinforced Polymers (FRP). This type of materials has been widely studied to the construction of pedestrian footbridges. Although its properties has several benefits, lightweight pedestrian structure are more prone to suffer from resonance effects induced for serviceability loads. Besides, the uncertainties associated with the estimated modal properties, the excitation of more than one vibration mode, and the sensibility of the structure to be excited under any harmonic load induced by the pedestrian, result in a poor performance of passive TMDs to control vibration in this type of lightweight structures.

The assesment of the vibration level is applied to the optimum design of a TMD and a STMD to control the excessive vibrations of a real FRP footbridge. A lightweight FRP footbridge designed using the motion-based design method and constructed at the Laboratory of Structures of the Technical University of Madrid is used as a benchmark structure (see Figure 3.7). The structure fulfills all the structural limit states except the vibration serviceability one, which should be met through the integration of an inertial damper [88]. The footbridge, which is 10 m-long and 1.5 m-wide, is simply supported at the two ends and consists of three longitudinal Glass Fiber-Reinforced Polymers (GFRP) stringers connected by transversal GFRP crossbeams placed every 1.20 m. In order to provide a higher bending stiffness and less static sag, Carbon FRP strips are bonded to the top and bottom flanges of the longitudinal stringers. The handrails are comprised of GFRP profiles with a square hollow section connected to the transversal beams. From [88], the first bending mode is achieved at 7.63 Hz, and the second and third mode are torsional modes that are unlikely to be excited by a pedestrian.

Figure 3.7: FRP footbridge at the Laboratory of Structures of the Technical University of Madrid.

3.4.1 Human induced vibration

The design acting force corresponds to the action of a pedestrian on the structure. Therefore, the pedestrian model based on the Mass-Spring-Damper Actuator (MSDA) proposed by Gallegos et al. [88] is considered.

The Humand-Structure Interaction (HSI) model considers the human interactive force originated from the structure movement. Based on Dougill et al. [89], the dynamic properties of the pedestrian could be analyzed as a MSDA system, while the structure is represented as a Single-Degree-of-Freedom (SDOF) system, for the sake of clarity, defined through the following equation:

$$m_s\ddot{x}_s + c_s\dot{x}_s + k_s x_s = F_h, \tag{3.31}$$

where the parameters m_s, c_s, k_s are the generalized modal mass, damping coefficient, and modal stiffness of the structure, respectively; x_s is the structure displacement (dots mean time derivatives); and F_h is the resultant force acting on the structure. This system can also be represented in the Laplace domain by the following TF between the structure acceleration and the force:

$$G_S(s) = \frac{s^2 X_s(s)}{F_h(s)} = \frac{s^2}{s^2 m_s + s c_s + k_s}, \tag{3.32}$$

The equations of motion that govern the HSI model are obtained from the force balance of Figure 3.8a [90] and are given by:

$$m_h\ddot{x}_h + c_h(\dot{x}_h - \dot{x}_s) + k_h(x_h - x_s) = F_a, \tag{3.33}$$

$$m_s\ddot{x}_s + c_s\dot{x}_s + k_s x_s - c_h(\dot{x}_h - \dot{x}_s) - k_h(x_h - x_s) = -F_a, \tag{3.34}$$

where the subindexes h and s refer to the human and structure, respectively. The human model is defined by the effective body mass (m_h, which is a fraction of the total human

body mass), the stiffness (k_h), the damping coefficient (c_h), and the actuator force F_a also known as driving force that represents a pair of action reaction forces generated by the human legs that act simultaneously on both the structure and the human. Additionally, the transmitted interaction force, denoted as F_{hsi}, is derived as follows:

$$F_{hsi} = c_h(\dot{x}_h - \dot{x}_s) + k_h(x_h - x_s). \tag{3.35}$$

Taking Laplace transforms of the Equations (3.33)–(3.35) and considering Equation (3.32), the following TFs are derived:

$$G_{HSI}(s) = \frac{F_{hsi}(s)}{s^2 X_s(s)} = \frac{-m_h(sc_h + k_h)}{s^2 m_h + sc_h + k_h}, \tag{3.36}$$

$$G_A(s) = \frac{F_{ha}(s)}{F_a(s)} = \frac{-s^2 m_h}{s^2 m_h + sc_h + k_h}, \tag{3.37}$$

with $G_{HSI}(s)$ being the TF between the human interacting force and the acceleration response of the structure and $G_A(s)$ being the TF between the human force without considering the movement of the structure and the driving force.

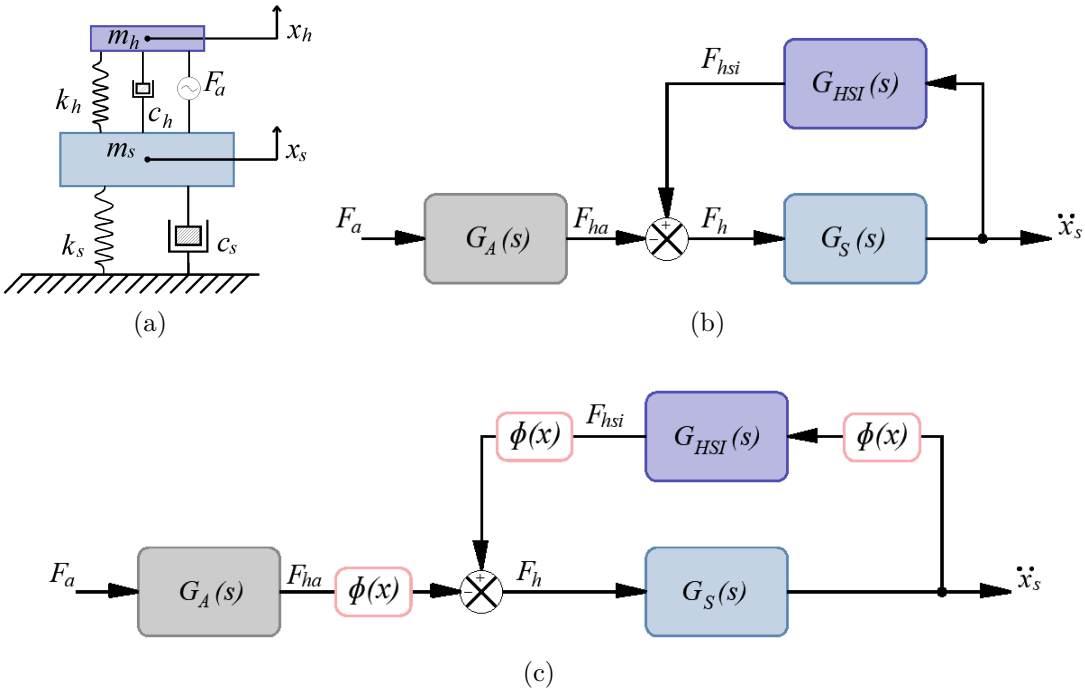

Figure 3.8: (**a**) Free body diagram for a SDOF structure. (**b**) Block diagram of the HSI model. (**c**) Block diagram considering a moving pedestrian.

Using Equations (3.32), (3.36) and (3.37), the HSI model for nonmoving actions (such as jumping or bouncing) can be represented as the block diagram of Figure 3.8b. To account for a pedestrian passing along the footbridge, the block diagram of Figure 3.8b can be modified according to the position of the pedestrian, as depicted in Figure 3.8c.

The force acting on the structure must be scaled by the modal shape $\varphi(x)$. Thus, the resultant force acting on the structure will be $\varphi(x)F_h$, in which $x = vt$ and the velocity of the MSDA system (v) depends on the gait frequency. Finally, it is worth mentioning that more than one vibration mode can be considered at the control point by modifying $G_S(s)$.

Due to the fact that each pedestrian has different modal parameters, a certain value of uncertainty is present in the system. Therefore, the TF of the structure including uncertainties (Equation (3.32)) can be replaced by the following expression:

$$\widehat{G}_S(s) = \frac{s^2 X_s(s)}{F_h(s)} = \frac{s^2}{s^2\widehat{m}_s + s\widehat{c}_s + \widehat{k}_s}, \tag{3.38}$$

where "$\widehat{\bullet}$" refers to uncertainty. Although one vibration mode is assumed, the extension to several vibration modes is straightforward by considering their contribution in TF (3.38).

This must also be applied to the TF associated with the interaction phenomenon (Equation (3.36)) and that associated with the human load (Equation (3.37)), yielding:

$$\widehat{G}_{HSI}(s) = \frac{F_{hsi}(s)}{s^2 X_s(s)} = \frac{-\widehat{m}_h(s\widehat{c}_h + \widehat{k}_h)}{s^2\widehat{m}_h + s\widehat{c}_h + \widehat{k}_h}, \tag{3.39}$$

$$\widehat{G}_A(s) = \frac{F_{ha}(s)}{F_a(s)} = \frac{-s^2\widehat{m}_h}{s^2\widehat{m}_h + s\widehat{c}_h + \widehat{k}_h}. \tag{3.40}$$

The driving force, F_a, which affects the structure and the pedestrian simultaneously, is defined as:

$$F_a(t) = Q\left(1 + \sum_{n=1}^{k} GLF_n \cdot sin(2\pi nft + \psi_n)\right) \tag{3.41}$$

where Q is the static load of the pedestrian, f is the pacing frequency, ψ_n is the phase angle of the n-th harmonic, k is the number of harmonics considered, and GLF (Generated Load Factor) is the coefficient of the harmonic force associated with the n-th harmonic [88]. As mentioned above (Figure 3.8c), this force is influenced by the pedestrian's position.

In order to take into account the uncertainty associated with the parameters that define the HSI model, N different samples of structures and pedestrian loads are analyzed. Every structure sample is crossed by one pedestrian whose pacing frequency is tuned to the worst case scenario. Therefore, the structure $\widehat{G}_s(s)$ is derived using $N = 50$, the generalized modal mass is assumed to follow a normal distribution $\mathcal{N}(405,\, 0.1^2)$, 405 kg being the mean and 0.1 the standard deviation. On the other hand, the natural frequency and damping ratio are assumed to follow a Weibull distribution, which is recommended to describe the stiffness and strength of pultruded FRP elements [91]. The former is characterized by a scale parameter $\alpha = 8.095$ and a shape parameter $\beta = 7.906$ whereas the latter is characterized by $\alpha = 1.616$ and $\beta = 12.153$. The lower and upper limits for the structure parameters are shown in Table 3.1. A wide variation range for the structure natural frequency is assumed. This is established on the basis of the following considerations: if the rolling supports are totally blocked, the natural frequency increases

by up to 9.13 Hz (that is, under higher rolling friction and or support deterioration, the roller may not be properly activated and the structural natural frequency increases significantly) and if a recycled rubber wearing layer (with a weight up to 60 kg/m^2) is placed over the deck, the natural frequency decreases to 5.15 Hz. The frequency response function for each of the N samples is represented in Figure 3.9, where it can be seen that the detuning effects of the control device could arise when only a nominal structure is considered. From Figure 3.9, it is concluded that 62% of the uncertain cases present natural frequencies between 6.5 and 8.5 Hz.

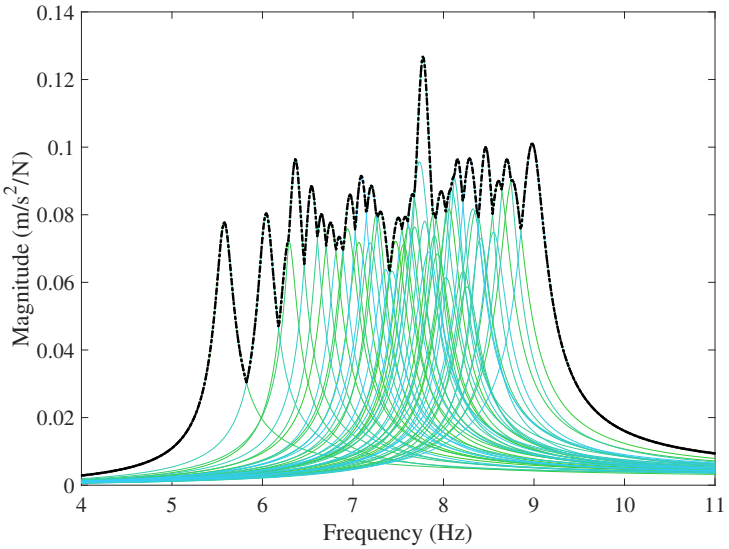

Figure 3.9: FRF behavior for all structures analyzed.

The equivalent properties of the pedestrian, mass and damping ratio, are considered to follow a normal distribution and a uniform distribution, respectively. The normal distribution of the mass is adopted as $\mathcal{N}(65.1, 5^2)$ and the damping ratio is set on the basis of the following limits: the lower limit is equal to 0.1 and the upper limit to 0.4 according to the literature [92]. Hence, based on the previous distributions, the properties of the HSI model are summarized in Table 3.1. Note that the frequency of the human body is chosen to be equal to the gait frequency, as suggested by Refs. [88, 93, 94]. The latter is assumed to be the natural frequency of the structure divided by four in order to affect directly the structure by the fourth harmonic. Therefore, the pedestrian excites the footbridge with up to his/her fourth harmonic. The following parameters, taken from Ref [88], have been adopted for the definition of the driving force, F_a (Equation 3.41): $Q = 686.70$ N; $GLF_1 = 0.1673$, $GLF_2 = 0.1787$, $GLF_3 = 0.1296$, $GLF_4 = 0.0315$, $\psi_1 = 0$, $\psi_2 = -\pi/2$, $\psi_3 = \pi$, and $\psi_4 = \pi/2$. As mentioned in Section 3.4.1, the MSDA system moves at a velocity depending on the gait frequency according to the expression $v = 1.271f - 1$ (m/s) [95].

Table 3.1: Parameters for the sensitivity analysis.

	Structure	**Value**	**Units**
m_s	Mass	[286.00 to 495.80]	kg
f_s	Frequency	[4.60 to 10.40]	Hz
ζ_s	Damping ratio	[0.86 to 1.83]	%
c_s	Damping coefficient	[279.40 to 931.10]	kg/s
k_s	Stiffness	[3.54 to 17.05]x10^5	N/m
	Human	**Value**	**Units**
m_h	Mass	[50.41 to 76.43]	kg
f_h	Frequency	$f_s/4$	Hz
ζ_h	Damping ratio	[10 to 40]	%
c_h	Damping coefficient	[164.38 to 643.50]	kg/s
k_h	Stiffness	[3.52 to 17.18]x10^3	N/m

3.4.2 Inertial control device with semi-active linear viscous damper

In order to evaluate the effectiveness of the STMD, its performance is compared against the passive TMD. The TMD has been defined widely in section 3.2, and its equation of motion and TF $G_T(s)$ have been presented there. Since the response of the TMD only depends on the transfer force by the structure, the HSI model does not influence the response of $G_T(s)$. Thus, the integration of a control device is straightforward.

Figure 3.10 shows the block diagram for the HSI (Figure 3.8b) model including the feedback loop of the TMD control force. Note that the TMD loop does not depend on the position of the pedestrian action.

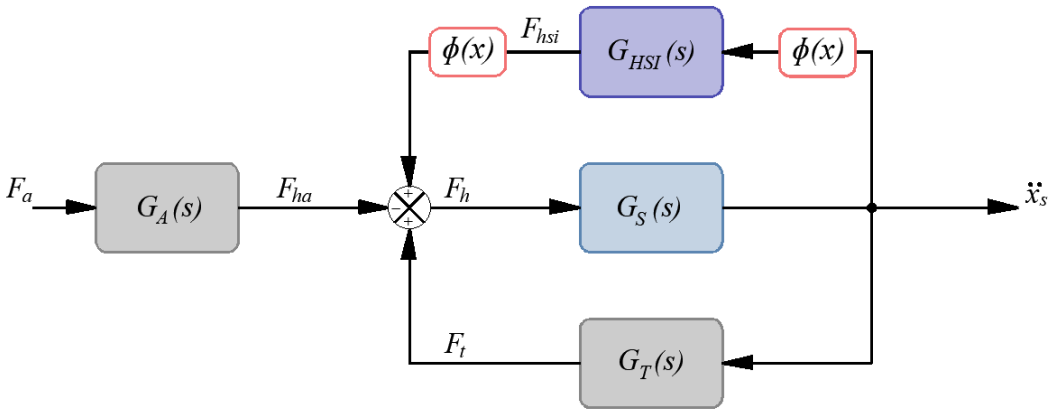

Figure 3.10: Block diagram of the HSI and TMD models.

The STMD has been defined in section 3.2.2, and its control law corresponds to an On-Off phase control. Similar to the the passive TMD, the STMD does not change its

behavior when the TMD model is considered. The passive part of the STMD reacts based on the transfer force by the structure, while the semi-active part of the STMD reacts based on the response of the structure and the inertial mass, according to the control law defined in section 3.3.

Figure 3.11 shows the block diagram for the HSI model with a STMD, where the transmitted force from the control device to the structure is obtained from the sum of the elastic force (linear and represented by its TF $G_K(s)$) and damper force (nonlinear and defined by the control law).

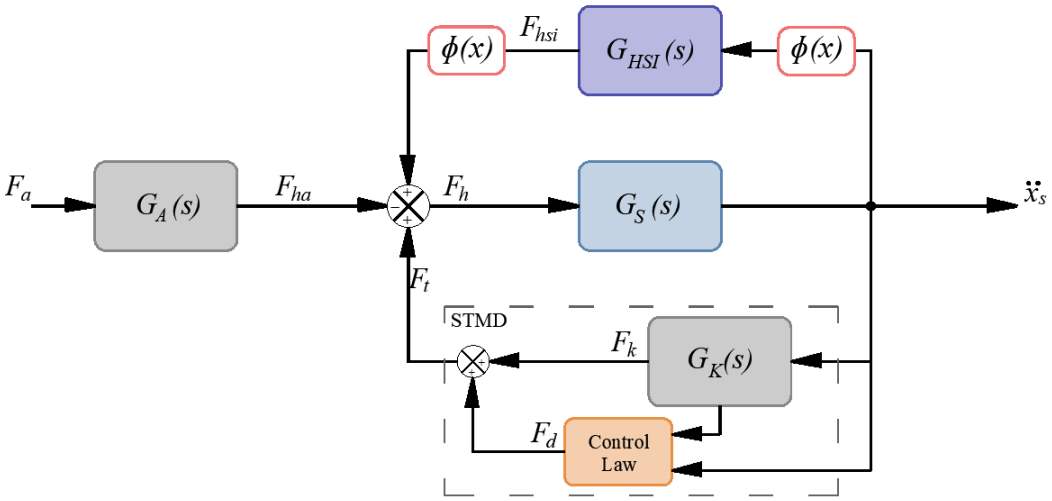

Figure 3.11: Block diagram of the HSI and STMD models.

3.4.3 Evaluation methodology and optimum design.

The proposed methodology consists of the optimum design of a TMD and a STMD by solving a multiobjective constrained optimization problem. Hence, the aim of the optimum design is to obtain an acceleration of the structure below the limit stated by guidelines while minimizing the inertial mass value and the size of the semi-active devices represented by its saturation force.

Three objective functions are estimated to be minimized through a multiobjective optimization problem. These are derived from the so-called performance indexes. The multiobjective constrained minimization problem is expressed as follows:

$$\text{find } \boldsymbol{\theta} \text{ such that minimizes } \boldsymbol{\Phi} = (\phi_1, \phi_2, \phi_3)$$
$$\text{s.t. } \begin{cases} \boldsymbol{\theta}_l \leq \boldsymbol{\theta} \leq \boldsymbol{\theta}_u \\ \ddot{x}_{s,max} \leq a_{lim} \end{cases}$$

where $\boldsymbol{\theta}$ are the design parameters defined between a lower $\boldsymbol{\theta}_l$ and upper $\boldsymbol{\theta}_u$ bound. The TMD design parameters are the mass (m_t), frequency (f_t), and damping ratio (ζ_t). The

STMD considers the same design parameters. However, the damping ratio is changed for the saturation force (F_{sat}). In the case of the damping ratio for the semi-active device, this parameter is defined in two states, $\zeta_{min} = 2\%$, and $\zeta_{max} = 50 \cdot \zeta_{min}$, so $\boldsymbol{\theta} = (m_t,\ f_t,\ \zeta_t \text{ or } F_{sat})$. ϕ_{1-3} are the three objective functions to be minimized; and $\ddot{x}_{s,max}$ is the maximum acceleration of the structure limited to a_{lim}.

The three objective functions, ϕ_{1-3}, are defined as:

$$\phi_1(\boldsymbol{z}, \boldsymbol{h}, \boldsymbol{\theta}) = w_1 J_{1,P} + w_2 J_{1,RMS}, \quad \text{with} \quad w_1 = w_2 = 0.5, \tag{3.42}$$

$$\phi_2(\boldsymbol{z}, \boldsymbol{h}, \boldsymbol{\theta}) = J_2, \tag{3.43}$$

$$\phi_3(\boldsymbol{z}, \boldsymbol{h}, \boldsymbol{\theta}) = J_3, \tag{3.44}$$

where $\boldsymbol{z} = [m_s, c_s, k_s]$, $\boldsymbol{h} = [m_h, c_h, k_h]$ are the structure and pedestrian parameters defining the HSI model and w_1 and w_2 are weighting factors. $J_{1,P}$, $J_{1,RMS}$, J_2, and J_3 are the performance indexes.

The first index is related to the ratio of maximum peak acceleration of the structure with and without the control strategy implemented (the peak acceleration without control is denoted as $\breve{\ddot{x}}_s$) whereas the second one does the same with the 1-s running Root Mean Square (RMS) acceleration. Thus, the first objective function ϕ_1 is a balance between the peak acceleration and the persistent acceleration (represented by the RMS acceleration). The third and fourth performance indexes consider the inertial mass and the damping force (TMD) or saturation force (STMD), respectively, which determine the damper size (affecting both the inertial mass and the MR damper needed). Therefore, the four performance indexes are calculated with the following expressions:

- Normalized Peak Acceleration:

$$J_{1,P} = \sum_{i=1}^{N} \left(\frac{max|\ddot{x}_s(t)|}{max|\breve{\ddot{x}}_s(t)|} \right),$$

- Normalized 1s-RMS Acceleration:

$$J_{1,RMS} = \sum_{i=1}^{N} \left(\frac{RMS(\ddot{x}_s(t))}{RMS(\breve{\ddot{x}}_s(t))} \right),$$

- Inertial Mass of the Control Device:

$$J_2 = m_t,$$

- Saturation force:

$$J_3 = F_{sat}.$$

with N being the number of samples. The F_{sat} of the TMD corresponds to the maximum damping force provided by the viscous damper for the whole set of structures and humans considered in the analysis.

The optimum design of the inertial control aims to reduce the vibration level of the footbridge, obtaining the lowest possible value to the aforementioned performance indexes. The value of a_{lim}, which should not be exceeded, is adopted as $a_{lim} = 1\,\mathrm{m/s^2}$ for both control devices (medium comfort) measured in the midspan of the footbridge.

In order to avoid falling into local minimal, a global optimization algorithm is employed to solve the minimization problem. In particular, the multiobjective Genetic Algorithm implemented in the software MATLAB (*gamultiobj* function) is used. An initial population of 50 individuals (parameter vectors with the design variables) are randomly created and iteratively modified according to the natural selection rules of the algorithm, which are based on the selection, crossover, and mutation mechanisms. The selection mechanism selects parents on the current population to create the next generation. Once the parents have been selected, the crossover and mutation mechanism create the new population. The fraction of the population created at the next generation by the crossover function is 0.8. The mutation makes small random changes in the individuals to provide genetic diversity and enable the genetic algorithm to search a broader space.

To carry out this process, the objective function runs a Simulink model, which simulates the human-structure-actuator interaction to calculate the maximum acceleration of the footbridge under the human load. The maximum number of iterations is set from a sensitivity analysis, giving a value of 50 iterations where the upper and lower limits in the population of the design variables for the TMD and the STMD are summarized in Table 3.2. At each iteration, the objective functions are assessed for the new population. When the acceleration $\ddot{x}_{s,max}$ measured at the midspan of the footbridge exceeds a_{lim}, a penalty is applied to the objective functions.

Table 3.2: Lower and upper bounds for the design variables of the inertial controller.

	Design Variable	**Lower Bound**	**Upper Bound**
m_t	Mass (kg)	10	45
f_t	Frequency (Hz)	1.00	10.00
ζ_t	Damping ratio (%)	1	50
F_{sat}	Saturation force (N)	10	5000

Once the minimization problem is carried out, the Pareto front is obtained. Each point forming the curve of the Pareto front represents a possible solution to the problem and the choice of the optimum among all of them may be transformed into a decision-making problem. The three objective functions considered in the problem prevent the classical representation of the Pareto front based on two objectives. Hence, the trade-off point cannot be illustrated and a multidimensional visualization method should be employed.

In this study, the Level Diagrams method proposed by Blasco et al. [96] is used, which allows representing the Pareto front according to proximity to the utopic point on the basis of a given norm. The following steps are carried out.

First, the three objective functions are normalized with respect to their maximum and minimum values to between 0 and 1 as follows:

$$\begin{aligned} &\phi_{i,max} = \max(\phi_i), \qquad \phi_{i,min} = \min(\phi_i) \quad i = 1,2,3 \\ &\bar{\phi}_i = \frac{\phi_i - \phi_{i,min}}{\phi_{i,max} - \phi_{i,min}}. \end{aligned} \tag{3.45}$$

Second, the Euclidean norm (2-norm), defined as $||\bar{\mathbf{\Phi}}||_2 = \sqrt{\sum_i^3 \bar{\phi}_i^2}$, is calculated for the three objective functions selected in this study.

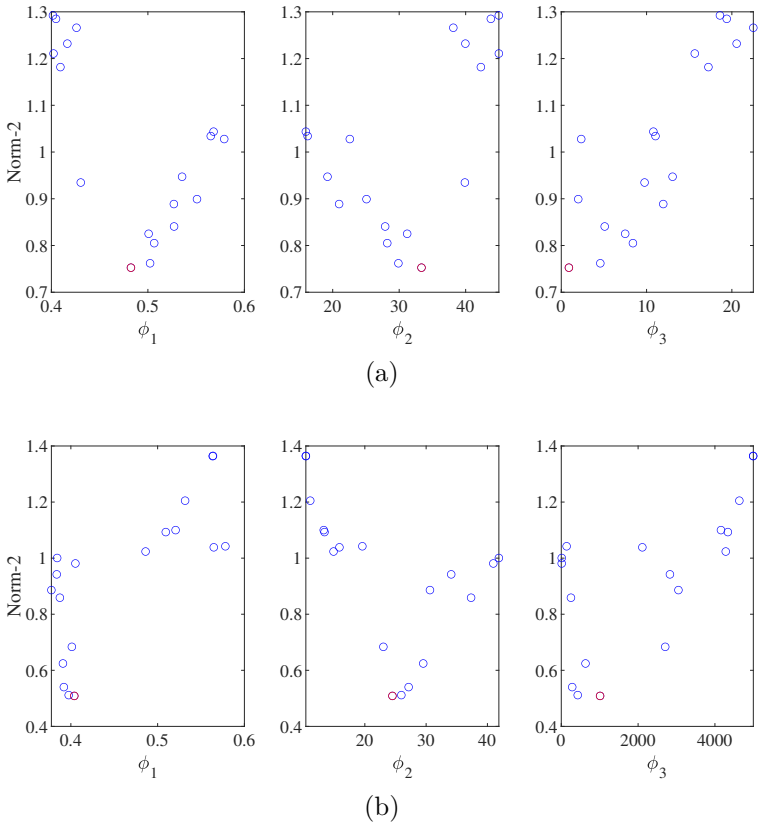

Figure 3.12: Pareto front obtained for the optimum design of the (**a**) TMD and (**b**) STMD. The selected optimum solution is marked in red.

The representation of the new Pareto front has a common Y axis representing the Euclidean norm, and each X axis corresponds to the values of the three objective functions. The optimum solution corresponds to the lowest value of the Y axis, i.e., the Euclidean

norm. This type of representation of the Pareto front is illustrated in Figure 3.12 for the TMD and the STMD. Once the method is applied, the optimum parameters of the TMD (mass, frequency, and damping ratio) and the STMD (mass, frequency, and saturation force), displayed in Table 3.3, are obtained. Note that the required mass ratio for the two devices is higher than the typical mass ratios employed for footbridges constructed with traditional materials. This fact is essentially due to the need to cancel vibrations in a very lightweight structure that may vibrate significantly under nonresonant actions due to the HSI. In case of the TMD, once the optimal parameters m_t, f_t, and ζ_t are obtained, the stiffness $k = (2\pi f_t)^2 m_t$ and the damping coefficient $c_t = 2m_t(2\pi f_t)\zeta_t$ are derived. In case of the STMD, once the optimal parameters m_t, f_t, and F_{sat} are obtained, the stiffness is derived and c_t is calculated from $\zeta = 0.02$. Finally, the control law is implemented using $c_{min} = c_t$ and $c_{max} = 50c_t$.

Table 3.3: Optimum parameters of the TMD and the STMD, and the value of the first objective function.

TMD		**Value**	
m_t	Mass	33.36	kg
f_t	Frequency	9.95	Hz
ζ_t	Damping ratio	1.03	%
c_t	Damping coefficient	42.96	kg/s
k_t	Stiffness	$1.30 \cdot 10^5$	N/m
ϕ_1	Objective function	0.48	-
STMD		**Value**	
m_t	Mass	24.50	kg
f_t	Frequency	6.15	Hz
c_{min}	Normal functioning	37.91	kg/s
c_{max}	Blocking functioning	1895.7	kg/s
k_t	Stiffness	$3.66 \cdot 10^4$	N/m
F_{sat}	Saturation force	1010.24	N
ϕ_1	Objective function	0.40	-

From Table 3.3, ϕ_1 has similar values in both cases, which indicates similar performance of the controlled structure. However, the inertial mass of the STMD is much lower than the one of the TMD (approximately a 27% reduction). Figure 3.13a shows a time history example of the dynamic response of the structure when a pedestrian crosses the footbridge. Figure 3.13b shows the Cumulative Distribution Function (CDF) of not exceeding the 1-s running RMS value and Figure 3.13c shows the CDF of the instant acceleration for the N cases run, giving good evidence of the effect of both control systems under uncertainties. Both control devices fulfill the constraint specified in the optimization algorithm but the STMD outperforms the TMD in terms of the mass (which is significantly smaller) without loss of effectiveness.

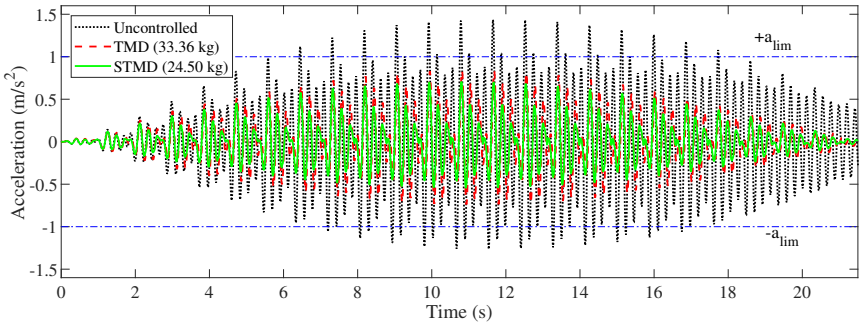

(a) Acceleration at midspan.

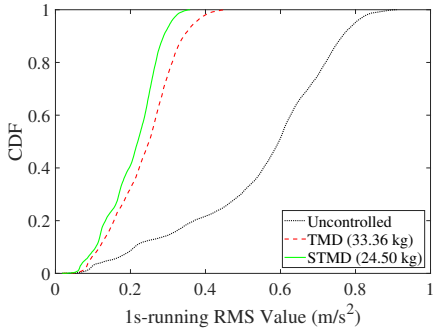

(b) CDF of the 1s-running RMS value of all the samples.

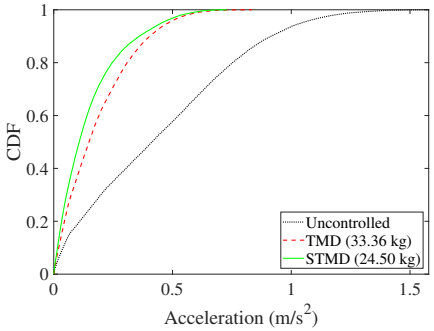

(c) CDF of the acceleration of all the samples.

Figure 3.13: Dynamic response of the bare and the controlled structure.

3.5 Semi-active inertial mass damper with magnetorheological damper

The assessment of the STMD carried out in Section 3.4, is developed herein by updating the ideal STMD to a real STMD. Thus, some considerations must be taken into account: (i) non-linear MR damper model; (ii) to introduce static noise on the measured signal used to include in the control law; (iii) implementation of an activation/deactivation rule; (iv) the implementation of a non-negligible dynamics of filters within the control law.

3.5.1 MR damper modeling

Several numerical models have been proposed to reproduce the response of an MR damper [52], where the Bingham and Bouc-Wen model are the most used. For example, the Bingham model is characterized by its simplicity and small number of parameters with a bi-linear behavior. The Bouc-Wen model considers the hysteretic behavior of the MR damper, the number of parameters for this type of model increases considerably improving the realistic response with respect to the first Bingham model.

In this case, the STMD installed in the structure takes into account the modal pa-

rameters obtained in the optimization process, modifying the semi-active viscous device by a MR damper RD-8041-1 of Lord Corporation, which has been identified in Barrera et al. [54] through a Bingham model, and those parameters are used in this section. Figure 3.14 shows the force velocity curve of this MR damper for several values of V. The MR damper is represented by the Bingham model through of the following equation:

$$F - f_o = F_c(V) \cdot sgn(\dot{x}) + c_o(V) \cdot \dot{x}, \tag{3.46}$$

where the parameters F and f_o are the total force of the MR damper and the preload force, respectively. Note that the preload force may be customized by the manufacturer. In this particular device, it was set to $f_0 = 20\,\text{N}$. The parameter F_c is the friction force whereas c_o is the damping coefficient, both dependent on the control voltage. The variable V is the control voltage applied to the MR damper (which is proportional to the current) and, according to the control law described in Equation 3.46, it can take a minimum or maximum value. In case of out MR damper, these values are 0.5 V and 5 V, respectively. Finally, the velocity $\dot{x}$ corresponds to the relative velocity between the STMD and the structure $(\dot{x}_t - \dot{x}_s)$.

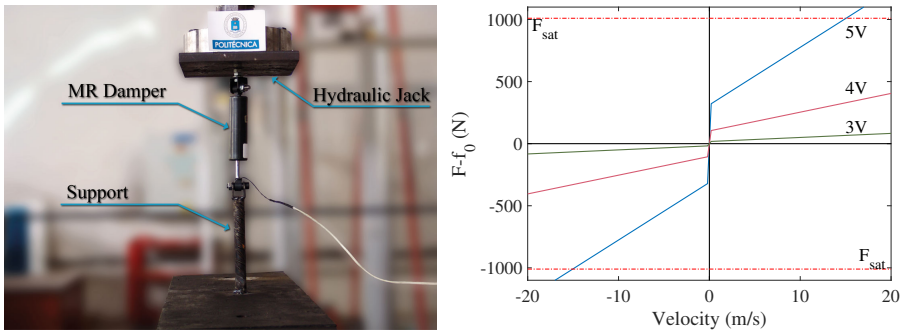

(a) (b)

Figure 3.14: (**a**) MR damper RD-8041-1 of Lord Corporation, (**b**)Force vs. velocity behavior of the MR damper.

3.5.2 Implementation of the control law

In order to account for the presence of noise in the signals, electrical noise has been added to the sensor measurement (structure and inertial mass acceleration, which are generally measured by accelerometers) yielding to noise-contaminated measurements [97]. Additionally, electrical noise is added to the control voltage generated by the control law. These noises are modeled as white noise within a predefined range: a noise peak value of $0.001\,\text{m/s}^2$ is assumed for the structure accelerometer; a noise peak value of $0.01\,\text{m/s}^2$ is assumed for STMD mass acceleration; and a noise peak value of 0.02 V is assumed for the control voltage. The peak noise values have been selected according to the available instrumentation to be used in a future implementation.

As commented before, the inertial mass and the structure acceleration are supposed to be measured. Now, the implementation of control law (Equation (3.30) considering the MR model (Equation (3.46)) is explained (and illustrated in Figure (3.15)). Three elements are proposed in the implementation: (i) low-pass filtering of both acceleration signals, (ii) a lossy integrator filter for velocity estimation, and (iii) an activation/deactivation rule.
To remove high-frequency noise and to avoid spillover instabilities, a second-order, low-pass Butterworth filter with a cut-off frequency of 20 Hz is applied to the acceleration used by the control law. Signals with frequencies above the cut-off frequency will be attenuated. The cut-off frequency must be at least twice the frequency of interest; otherwise, the acceleration records will shift in its phase, affecting the control law performance significantly. The low-pass Butterworth filter with a sampling frequency of 1000 Hz (the one used for numerical simulation and the expected one for the experimental implementation) is used and its Z-transform is as follows:

$$H_{low}(z) = \frac{0.0036z^2 + 0.0072z + 0.0036}{z^2 - 1.823 + 0.837}. \tag{3.47}$$

Integrator Filter

The relative velocity between the structure and the inertial mass is obtained by the integration of the acceleration signals. In Section 3.4.3, an ideal integrator $H_{int}(s) = 1/s$ was used. However, this type of integrator cannot be used experimentally since it is extremely sensitive for low-frequency components in real implementation [98]. A lossy integrator can maintain the magnitude and phase of an ideal integrator from a cut-off frequency, avoiding the high sensitivity at low frequencies, and removing signal offsets. Thus, the lossy integrator could be expressed through the following equation:

$$H_{int}(s) = \frac{s}{s^2 + 2s\zeta_i\omega_i + \omega_i^2}, \tag{3.48}$$

where ζ_i is the damping ratio of the integrator, which is chosen equal to 1, and ω_i is the cut-off frequency, which should be sufficiently smaller than the frequencies of interest in order to maintain the magnitude and phase. A cut-off frequency of $2\pi f_s/10$ has been adopted here. As in Equation (3.47), the Z-transform for a sampling frequency of 1000 Hz is derived:

$$H_{int}(z) = \frac{0.00099z - 0.00099}{z^2 - 1.99z + 0.99}. \tag{3.49}$$

Deactivation Rule

To prevent the MR damper from operating at low acceleration values, a deactivation rule has been adopted. This situation may occur under ambient loads. The application of On-Off control under low input signals may lead to instabilities (chattering problems) that are avoided by disconnecting the device. Additionally, the electrical consumption is reduced and the device lifespan is extended. For this case, the Off state is applied for 1-s-RMS

instant acceleration values of the structure lower than the threshold of $0.01\,\mathrm{m/s^2}$, so the input voltage to the MR damper is the minimum possible indicated by the manufacturer.

Figure 3.15 illustrates the block diagram of a structure with a HSI model and a semi-active control strategy. The noise in sensors, the low-pass filter, integrator filters, and the activate/deactivate rule have been included to represent a realistic scenario.

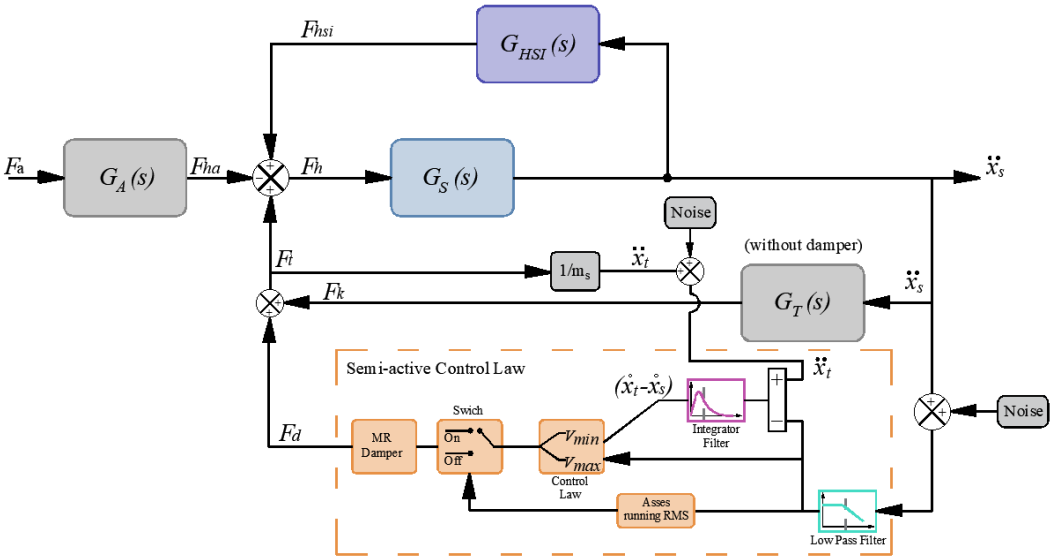

Figure 3.15: Block diagram of the HSI and STMD including all elements of the implementation and noisy signals.

3.5.3 Optimum design under realistic conditions

The application of the proposed design methodology is carried out again considering the MR model, noise-corrupted signals, and all the dynamics of the elements needed to experimentally implement the control law. Table 3.4 shows the optimum values obtained for the STMD MR (which includes all components mentioned before).

Table 3.4: Optimum parameters of the STMD MR.

STMD MR		**Value**	
m_t	Mass	24.38	kg
f_t	Frequency	6.00	Hz
k_t	Stiffness	$3.47 \cdot 10^4$	N/m
F_{sat}	Saturation force	88.27	N
ϕ_1	Objective function	0.48	-

The optimal values obtained are similar to those derived in Section 3.4.3 (Table 3.3, but the objective function ϕ_1 shows a reduction in the global performance of the STMD). In Figure 3.16, the three optimum controllers (TMD, STMD, and TMD MR) are compared.

Figure 3.16a shows the time history of acceleration for a particular case. Figure 3.16b,c shows the CDF for the 1-s-running RMS and instant acceleration for the N cases run, respectively. It can be observed that the STMD MR maintains the maximum values of acceleration under $1\,\mathrm{m/s^2}$, fulfilling strictly the constraint of the optimization problem. Three observations can be obtained at this point: (i) for the peak acceleration, the TMD and the STMD MRs show similar performances with a significant reduction in the inertial mass of the STMD (contributing thus to the lightness of the footbridge); (ii) for the TMD, it should be noted that ideal conditions have been assumed (dry friction, misaligned of the springs, nonlinear behavior of the viscous damper, and other experimental issues might reduce its performance) so a lower performance of the TMD is expected; (iii) the STMD MR slightly reduces its performance compared with the viscous STMD, as expected.

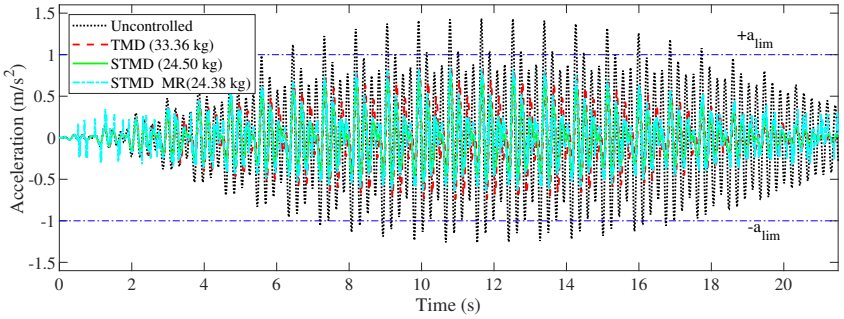

(a) Acceleration at midspan.

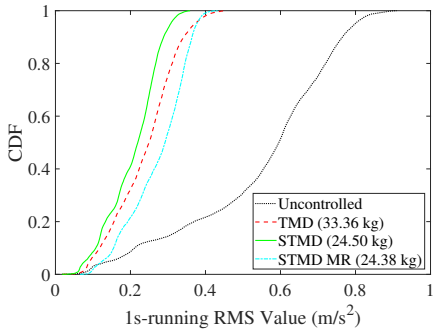

(b) CDF of the 1-s-running RMS value of all the samples.

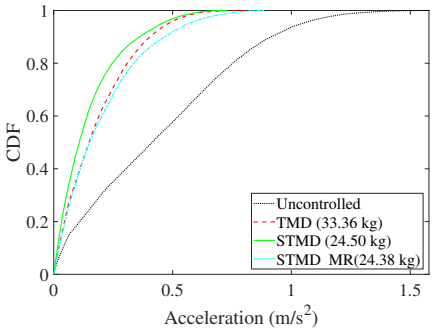

(c) CDF of the acceleration of all the samples.

Figure 3.16: Dynamic response of the footbridge with each control device.

Finally, the performance of the two STMDs is evaluated in terms of the objective function ϕ_1 under a real walking ground reaction force that is, in Figure 3.15, F_{ha} is now the vertical reaction force measured in an instrumented treadmill so that the input is not a pure harmonic action (see Figure 3.17). For this purpose, the footbridge cases with natural frequencies equal to 5.48, 7.63, and 10.39 Hz are considered. The natural frequency of 7.63 Hz corresponds to the natural frequency of the constructed footbridge (see Section 3.4.3).

The results are shown in Figure 3.18 and it is clearly observable the improvement obtained with the implementation of the STMDs, which achieves a substantial reduction of the acceleration. For the two cases analyzed under real walking excitation, it is shown how the performance of the STMD MR is degraded with respect to the viscous one, although this fact may be improved by implementing a continuous control law in future works.

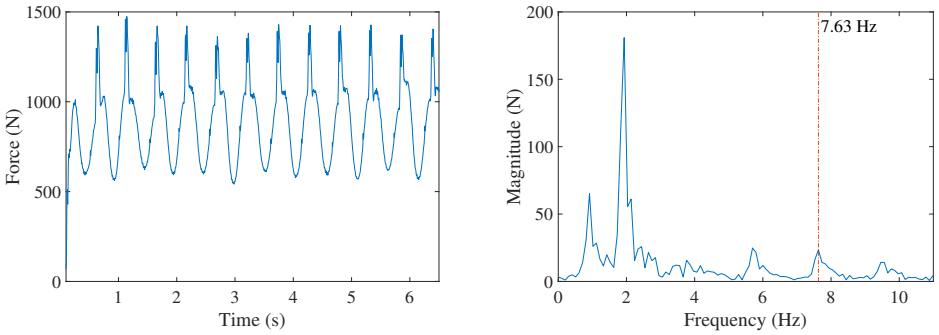

(a) Time history. (b) Fast Fourier Transform.

Figure 3.17: Vertical reaction force measured in an instrumented treadmill.

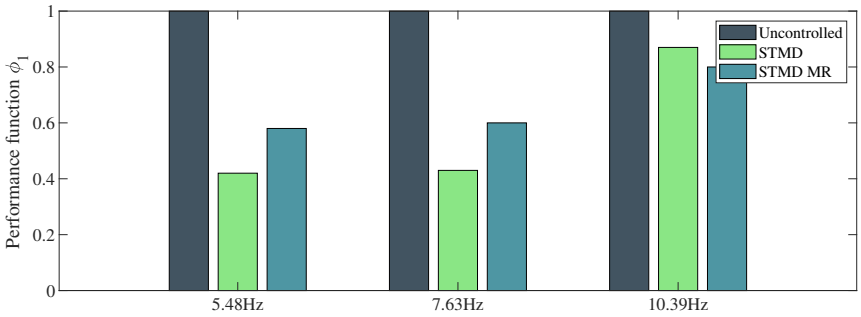

Figure 3.18: Objective function ϕ_1 of the optimum systems under different footbridge frequencies.

3.6 Experimental test

Once the numerical evaluation for the STMD was developed performed in Section 3.4, followed by an update to consider realistic conditions in Section 3.5, a series of experimental tests were conducted to validate the numerical model of the STMD with a phase control law.

To accomplish this goal, an STMD is attached to the lightweight FRP footbridge (Figure 3.7). The STMD presented in Figure 3.19 was configured with 26 Kg mass, four

springs with a stiffness of approximately 14 kN/m each, and two Sponge RD-1097-1 MR dampers from Lord Corporation.

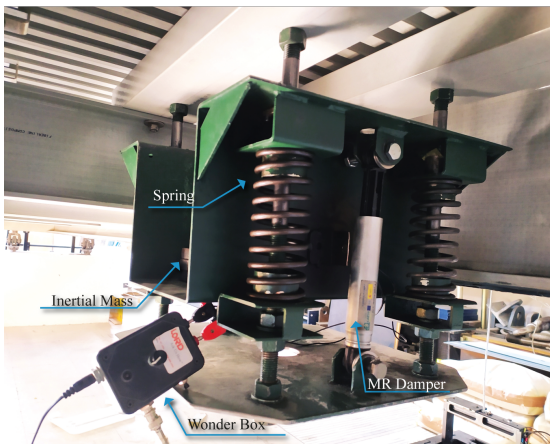

Figure 3.19: STMD under the lightweight FRP footbridge.

(a) Additional mass. (b) additional support.

Figure 3.20: Changes on the structure to introduces detuned effects.

The objective of the experimental tests is to evaluate the effectiveness of the STMD to control vibration levels when uncertainties on the structure are present in two main situations. i). Due to changes in the modal parameters, and ii) under pedestrian action by crossing the footbridge. To achieve the first situation, the natural frequency of the structure is changed to a lower value by increasing the mass of the structure. On the structure, six sandbags are included with 20 kg of weighing for each one to modify the natural frequency from 7.4 Hz to 6.2 Hz. This situation could occur in a lightweight structure if a group of pedestrians acts as a resting load. On the other hand, a simple support is incorporated near an edge to increase the stiffness of the footbridge and change the natural frequency from 7.4 Hz to 8.8 Hz. This situation could occur if the roller

support changes its natural behavior from a pinned support due to some natural degradation of the material. Taking into account that a control device is setting to achieve a frequency tuned of 7.4 Hz, the previous situations configure a “detuned below”and “detuned above”respectively. Figures 3.20a and 3.20b show the modification of the structure to achieve the modification of the natural frequency of the structure. If the control device (TMD or STMD) is setting to a frequency of 7.4 Hz and the natural frequency of the structure is below it (first situation)

In the second situation, one pedestrian is analyzed crossing by the footbridge with a tuned step frequency of 2.06 Hz, 1.85 Hz, and 2.2 Hz so that the third and fourth harmonic are 6.20 Hz, 7.40 Hz, and 8.8 Hz respectively. These frequencies pretend to be the same frequencies analyzed for the first situation considering the change from the original natural frequency of 7.40 Hz. Figure 3.21 shows two pedestrian walking on the structure with the aforementioned tuned step frequency.

(a) Pedestrian walking. (b) Pedestrian bouncing.

Figure 3.21: Structure under pedestrian effects.

3.6.1 Control strategies

The control law studied so far is the On-Off phase control, this control make work the semi-active devices from minimum to maximum response. However, the phase control is also evaluated replacing the On-Off control for a variable or continuous control. In this sense, with a continuous control, the response of the semi-active device would have intermediate values if a maximum force is not required.
According to Koo et al. [66], the On-Off control can be extended to a linear control with a pre-adjusted gain (G), which is previouly defined as a constant. The voltage control considering a linear behavior for the structure with STMD is given by:

$$v(t) = G \cdot \frac{\ddot{x}_s}{(\dot{x}_t - \dot{x}_s)}, \tag{3.50}$$

the relation between acceleration of the structure $\ddot{x}_s$ and relative velocity $(\dot{x}_t - \dot{x}_s)$ allows an increase or decrease in the voltage control correctly. If the denominator is higher, it

means that the structure and control system is tuned, in this case, a minimum damping force is required. Otherwise, if denominator is lower the system is detuned and a maximum damping force is required. The continuous control could be not effective if the pre-adjusted gain (G) is not correctly setting for the vibration level expected. Thus, the control voltage obtained will be maximum during all excitation event, experimenting a control strategy behaviors similar to an On-Off control.

To avoid this phenomena, the constant gain (G) is changed to a continuos time-variant as have been explained in section 2.3.4, and the continuos time-variant voltage control for the structure with the structure with STMD is defined as follows:

$$v(t) = \frac{v_{max}}{|\frac{\ddot{x}_s}{(\dot{x}_t - \dot{x}_s)}|_{T,max}} \cdot \frac{\ddot{x}_s}{(\dot{x}_t - \dot{x}_s)}. \tag{3.51}$$

3.6.2 Results experimental tests

In this section, the effectiveness of the phase control for semi-active inertial mass dampers under detuned behavior due to uncertain conditions defined in section 3.6 is evaluated. Three versions of phase control for the STMD are considered: *i)* STMD On-Off, with voltage control between $v_{min} = 0$ V and $v_{max} = 5$ V; *ii)* STMD with gain (G) constant; and *iii)* STMD with gain variable in time $G(t)$.

The FRP footbridge under a chirp signal, walking and bouncing effect generate by a pedestrian is analyzed with passive (TMD) and semi-active (STMD) control.

Chirp excitation

The structure has been forced to vibrate under a chirp signal that increase in frequency with time from 5 Hz to 10 Hz for a natural frequency of 6.2 and 7.4 Hz, while for a natural frequency of 8.8 Hz the frequency range of the chirp signal is 7 to 12 Hz. The results for the structure under chirp signal are presented below considering the TMD and STMD with the three phase control laws previously indicated.

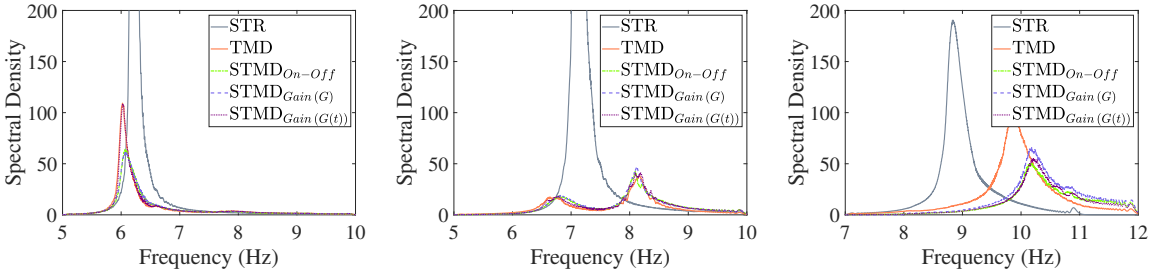

(a) PSD Structure at 6.2 Hz (b) PSD Structure at 7.4 Hz (c) PSD Structure at 8.8 Hz

Figure 3.22: PSD of the structure with passive and semi-active control, **a)** detuned below, **b)** tuned, **c)** detuned above.

Figure 3.22 shows Power Spectral Density (PSD) for the first analysis situation of the

structure. When the TMD or STMD is tuned regarding the natural frequency of the structure (3.22b), there is no significant difference between TMD and STMD response. On the other hand, for the case of detuning below (3.22a) and detuning above (3.22c) the STMD has the ability to reduce the amount of PSD developed by the system with respect to the TMD.

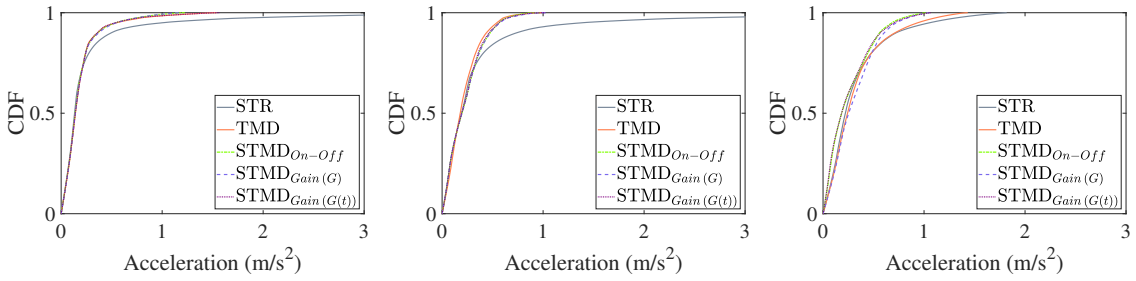

(a) CDF Structure at 6.2 Hz (b) CDF Structure at 7.4 Hz (c) CDF Structure at 8.8 Hz

Figure 3.23: CDF of acceleration of the structure with passive and semi-active control, **a)** detuned below, **b)** tuned, **c)** detuned above.

Figure 3.23 shows the CDF of the acceleration of the structure for the first analysis situation. For the first detuned case (Figure 3.23a), all control systems develop a similar behavior. For the tuned situation (Figure 3.23b) all control systems have similar responses without exceeding the limit of 1 m/s^2. Figure 3.23c shows how the STMD develops better performance than TMD with a 100% probability of not exceeding the acceleration of 1 m/s^2.

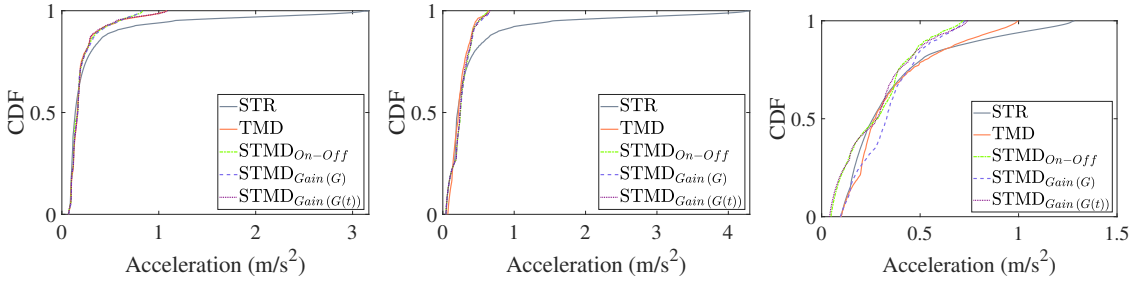

(a) CDF Structure at 6.2 Hz (b) CDF Structure at 7.4 Hz (c) CDF Structure at 8.8 Hz

Figure 3.24: CDF of RMS acceleration of the structure with passive and semi-active control, **a)** detuned below, **b)** tuned, **c)** detuned above.

Figure 3.24 confirms the behavior exhibited for the control systems in the CDF curve in Figure 3.23, but here is exposed in RMS acceleration values.

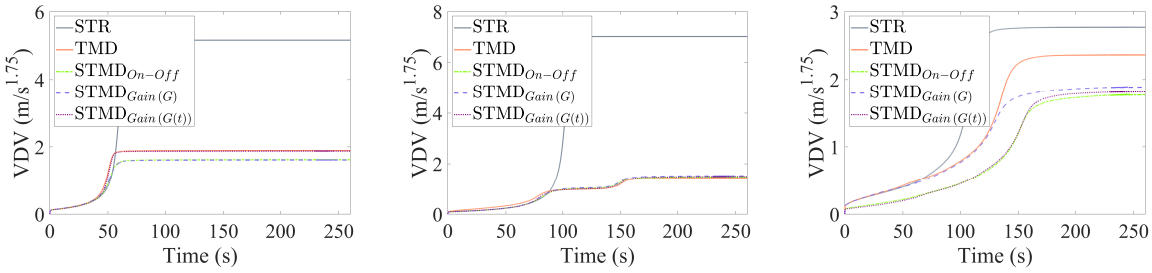

(a) VDV Structure at 6.2 Hz (b) VDV Structure at 7.4 Hz (c) VDV Structure at 8.8 Hz

Figure 3.25: VDV of the structure with passive and semi-active control, **a)** detuned below, **b)** tuned, **c)** detuned above.

Figure 3.25 represents the expected Vibration Dose Value (VDV) for the chirp signal in all analyzed systems. In Figure 3.25a the TMD and STMD with G(t) perform the same response for VDV evaluation. While for 3.25c the STMD performs a better response than TMD. One more time, for tuned situations (Figure 3.25b) all control systems have a similar behavior.

Walking excitation

In this section, one pedestrian has walked on the FRP footbridge with a tuned step frequency. First, at a frequency of 2.06 Hz to induces vibration on the structure at 6.20 Hz with its third harmonic. Followed by a step frequency of 1.85 Hz to induce vibration on the structure at 7.40 Hz with its fourth harmonic. Finally, with a step frequency of 2.20 Hz to induce vibration on the structure at 8.8 Hz with the fourth harmonic. In this sense, the detuned and tuned cases are achieved for one case mentioned for the second uncertainty situation.

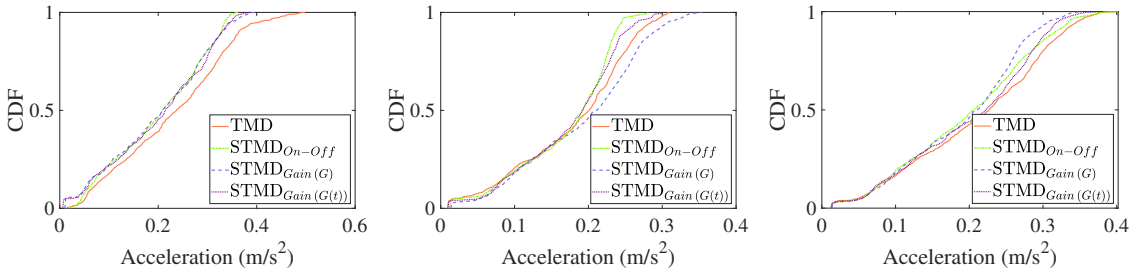

(a) CDF Structure at 6.2 Hz (b) CDF Structure at 7.4 Hz (c) CDF Structure at 8.8 Hz

Figure 3.26: CDF of RMS acceleration at 1 second for structure under walking excitation.

Figure **??** shows the CDF of the acceleration of the structure under a pedestrian walking at each step frequency mentioned previously. All control strategies prevent the

acceleration on the structure from exceeding 1 m/s^2. The STMD performs better control than the TMD, which is best appreciated in terms of RMS acceleration in the CDF curve presented in Figure 3.26.

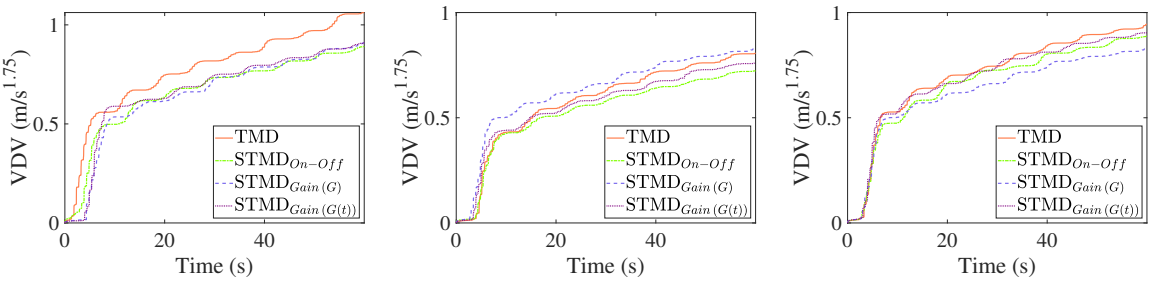

(a) VDV Structure at 6.2 Hz (b) VDV Structure at 7.4 Hz (c) VDV Structure at 8.8 Hz

Figure 3.27: VDV of acceleration for structure under walking excitation.

Figure 3.27 shows that VDV is less for STMD. For a step frequency of 2.06 Hz (figure 3.27a), the STMDs perform a similar response for all phase control laws. For step frequencies of 1.85 Hz and 2.20 Hz (figure 3.27b and figure 3.27c respectively), the same enhacement behavior is appreciable, although the response between phase control laws is not similar, it is better than for TMD.

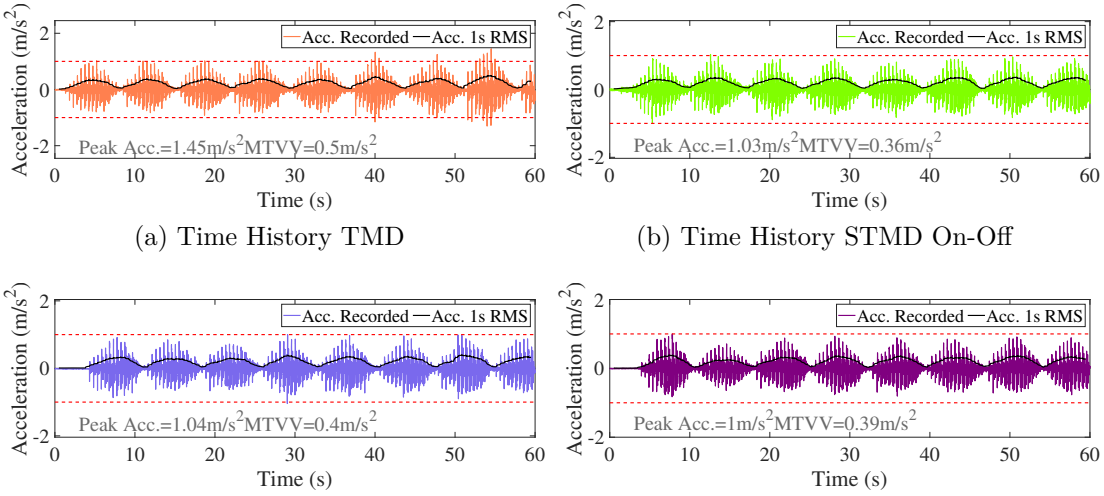

(a) Time History TMD (b) Time History STMD On-Off

(c) Time History STMD Gain (G) (d) Time History STMD Gain (G(t))

Figure 3.28: Time History recorded for pedestrian walking at 2,06 Hz of step frequency.

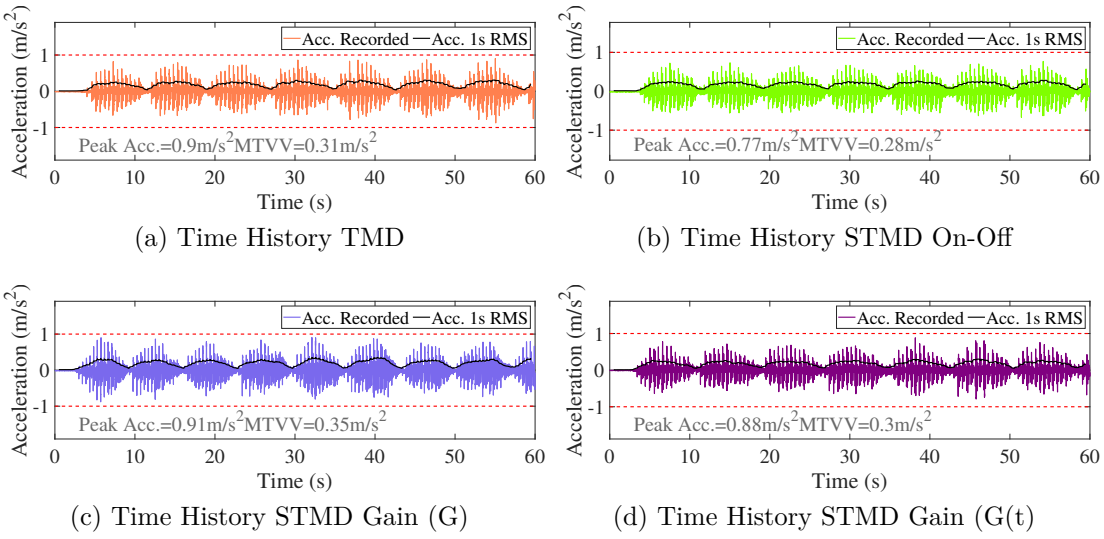

(a) Time History TMD (b) Time History STMD On-Off

(c) Time History STMD Gain (G) (d) Time History STMD Gain (G(t)

Figure 3.29: Time History recorded for pedestrian walking at 1,85 Hz of step frequency.

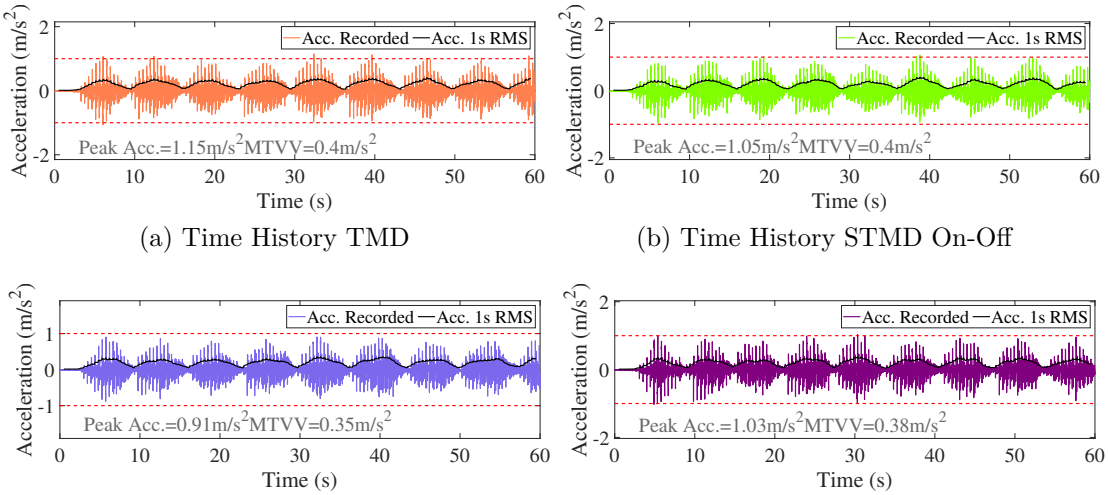

(a) Time History TMD (b) Time History STMD On-Off

(c) Time History STMD Gain (G) (d) Time History STMD Gain (G(t)

Figure 3.30: Time History recorded for pedestrian walking at 2,2 Hz of step frequency.

Bouncing excitation

Bouncing excitation occurs when one pedestrian or crowd of pedestrians makes their bodies jump. Figure 3.31 illustrates the CDF curve for this type of action, where for detuned cases (figures 3.31a and 3.31c) the STMD experiences less probability of exceeding acceleration than the TMD. For the tuned case (figure 3.31b), all control systems perform the same behavior.

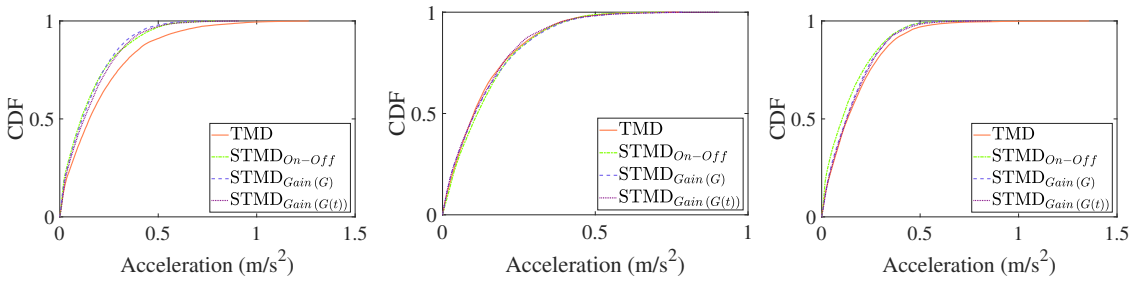

(a) CDF Structure at 6.2 Hz (b) CDF Structure at 7.4 Hz (c) CDF Structure at 8.8 Hz

Figure 3.31: CDF of acceleration for structure under bouncing excitation.

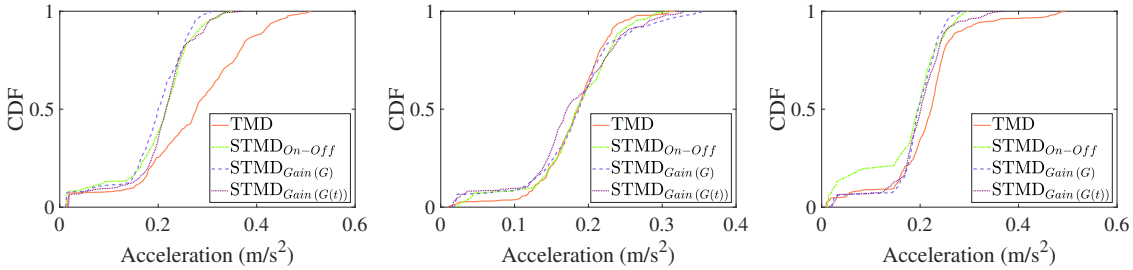

(a) CDF Structure at 6.2 Hz (b) CDF Structure at 7.4 Hz (c) CDF Structure at 8.8 Hz

Figure 3.32: CDF of RMS acceleration at 1 second for structure under bouncing excitation.

For RMS acceleration values presented in Figure 3.32, the STMD controls the vibration level better than the TMD. However, for tuned situations, the STMD loses effectiveness with respect to TMD.

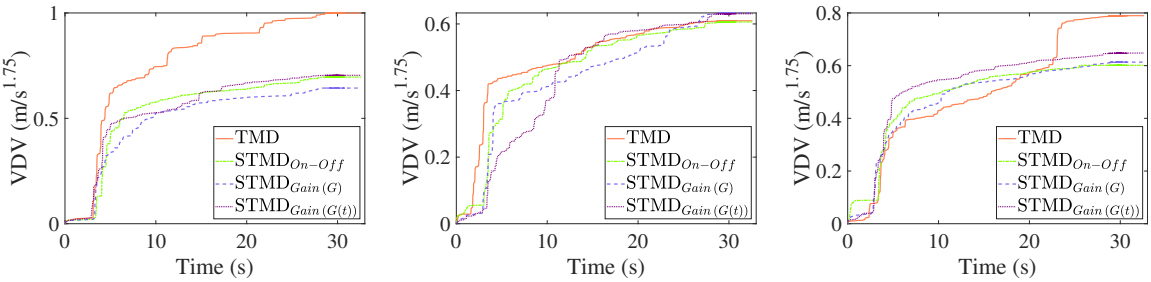

(a) VDV Structure at 6.2 Hz (b) VDV Structure at 7.4 Hz (c) VDV Structure at 8.8 Hz

Figure 3.33: VDV of acceleration for structure under bouncing excitation.

Figure 3.33 shows how for detuned cases the TMD experiences a vibration dose greater than the STMD (Figure 3.33a and 3.33c). For tuned cases (figure 3.33b), the control system responds similarly without manifesting a considerable diference. In this sense, the effectiveness of the STMD in controlling vibration dose for detuned cases is considerable

with respect to the TMD.

Figures 3.34, 3.35, and 3.36 present the recorded measurement of the bouncing action on the structure for each step frequency and each control system. In these cases, the STMD developed successful vibration control behavior, keeping the peak acceleration level below 1 m/s^2. Unfortunately, the TMD cannot provide vibration level reduction in detuned cases. Moreover, the Maximum Transient Vibration Value (MTVV) values for all phase control laws are similar for both tuned and detuned cases.

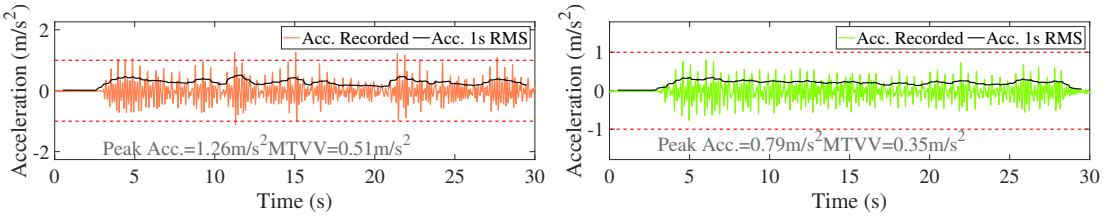

(a) Time History TMD

(b) Time History STMD On-Off

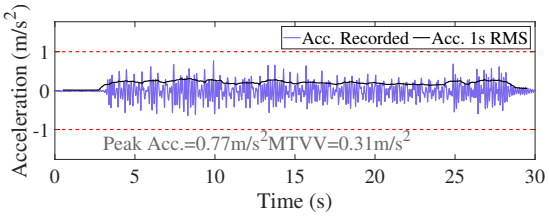

(c) Time History STMD Gain (G)

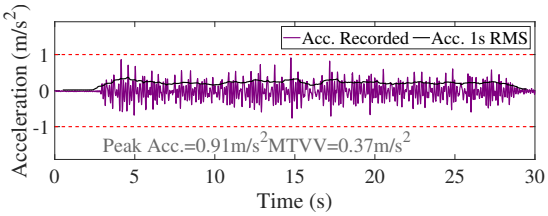

(d) Time History STMD Gain (G(t))

Figure 3.34: Time History recorded for pedestrian bouncing at 2,06 Hz of step frequency.

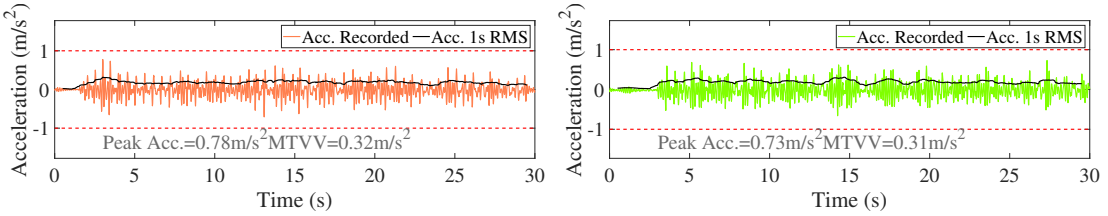

(a) Time History TMD

(b) Time History STMD On-Off

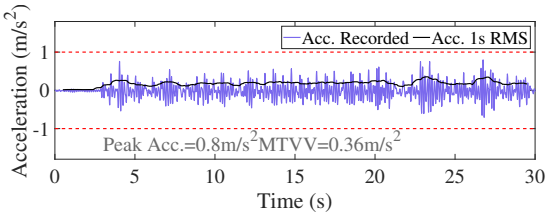

(c) Time History STMD Gain (G)

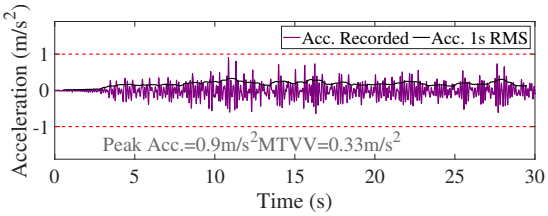

(d) Time History STMD Gain (G(t))

Figure 3.35: Time History recorded for pedestrian bouncing at 1,85 Hz of step frequency.

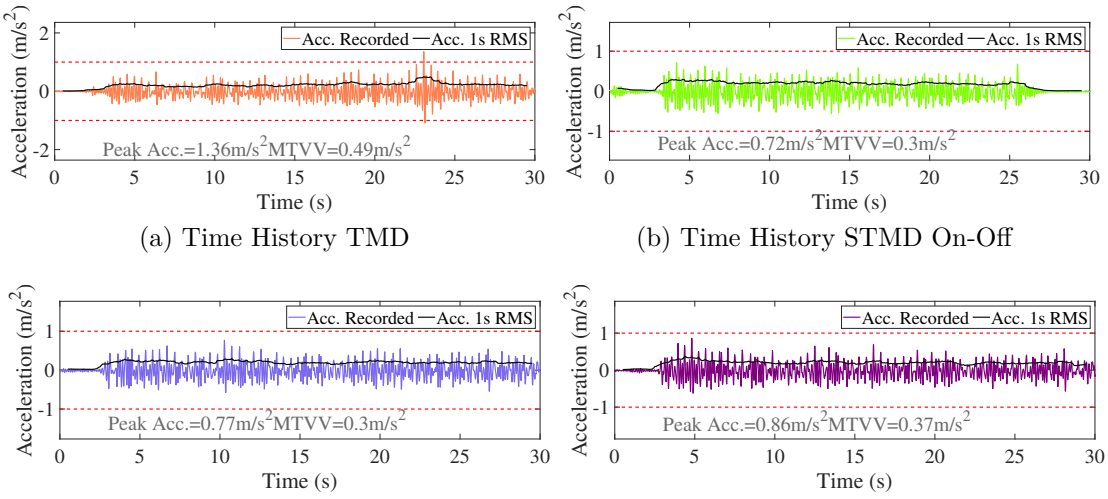

(a) Time History TMD

(b) Time History STMD On-Off

(c) Time History STMD Gain (G)

(d) Time History STMD Gain (G(t)

Figure 3.36: Time History recorded for pedestrian bouncing at 2,2 Hz of step frequency.

Chapter 4

Phase Control in Base Isolation Systems

This chapter introduces in section 3.1 a brief chronology of the base seismic isolation system since its discovery, first applications, and the different versions developed. In section 3.2 the concept of a base isolation system has been defined mathematically, and at the same time, the behavior for each type of isolator has been presented. The phase control over the base isolation system is introduced employing the ideal device described in section 3.2.2, and finally, an update to real approximation has been carried out in section 3.4 taking into account the bidirectional response of the isolator with a numerical model of a real semi-active device.

4.1 Introduction

The effect of vibrations on the structure have been an issue for many years. However, the use of vibration control strategies has also been adopted. The first register of a structure with a control strategy corresponds to the Artemis temple in Ephesus (Turkey) around the 6th century, where the structure was built over a layer of sand and stone to decouple the structure from the foundation [99]. Another example corresponds to the structures built in Lahijan (Iran), which are above layers of wooden beams, allowing each layer to roll over the others [100]. J. Bechtold and Jules Touaillon [30], through U.S. patents, documented these strategies officially as a new method to build structures with earthquake-proof capacity.

The concept of decoupling the structure from its foundation is known nowadays as base seismic isolation. According to Makris and Kelly [30, 101], the Tun Abdul Razak Research Center was the first to work on the mechanics of rubber bearing for vibration isolation of buildings. This type of passive device has been widely applied in the United Kingdom to isolate buildings from rail traffic vibration. The first one was the Albany Court building in London in 1966, followed by Grafton 16, which was built close to railway lines with the full-time operation. The Glasgow Royal Center Hall in Scotland and the International

Convention Center in Birmingham (England), were also built over isolation devices due to their location founded above two underground railway lines. For these cases, the source is characterized by its vibration to high frequencies (25 to 50 Hz), which generate vertical ground motion affecting the structure. The rubber bearing was designed with a vertical natural frequency of one-third of the lowest frequency of the vibration source.

To mitigate the vibration on the structure, the fundamental frequency of the isolator must be lower than the frequency of the vibration mode to be controlled, the lateral flexibility characteristic of the rubber bearings makes them the perfect device to mitigate earthquake effects because the rubber bearing reaches a fundamental frequency lower than the fundamental frequency of the structure, and the frequency content characteristic of earthquakes.

Makris et al. [30] have mentioned the elementary school in Skopje, Republic of Northern Macedonia, as the first building constructed with a base seismic isolation system. Years later, the application of base seismic isolation is reported in countries such as France and South Africa, where rubbers bearing has been used; Russia with the implementation of egg-shaped steel bearing; New Zealand improving the bridge bearings behavior including hysteretic dampers [102, 103], and the United States developing the new generation of the rubber bearings well-known as high-damping rubber bearings [104].

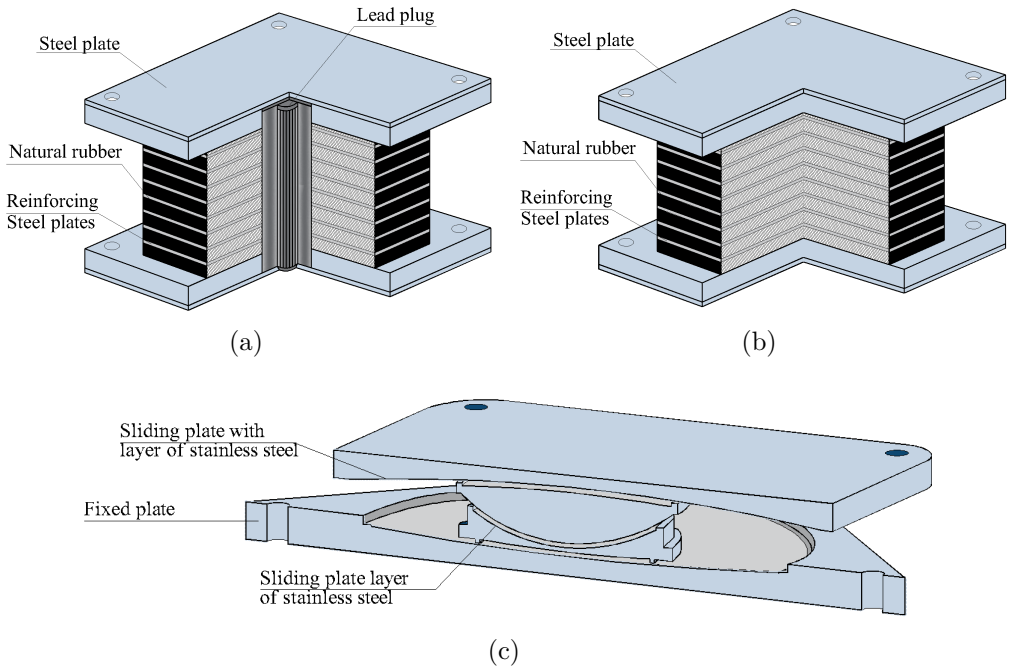

Figure 4.1: Isolators device. **a)** Lead Rubber Bearing (LRB),**b)** Natural (NRB) or High Damping Rubber Bearing (HDRB), and **c)** Frictional pendulum system (FPS)

Based on previous works, new generations of base isolation devices have been devel-

oped, with linear or Nonlinear behavior, such as LRB, Natural Rubber Bearing (NRB) or HDRB, and FPS, among the best-known (see Figure 4.1). Much research has been done on the analysis and implementation of base isolation devices. Turkington et al. [105] have carried out a parametric study of bridge superstructure supports on LRB. This system was analyzed under the effect of "El Centro"earthquake, and "The Parkfield"earthquake. Eem and Hahm [106] studied the application of LRB to nuclear power plants, evaluating the extreme performance of the LRB through full-scale dynamic tests. Hwang et al. [107] proposed two analytic models for HDRB, then these were tested in a shaking table to predict seismic response.

Deringöl et al. [108] have investigated the use of HDRB for steel buildings with different design properties to mitigate the seismic effects. The evaluation of the HDRB was carried out considering a variation on the main properties of the HDRB, such as period, effective damping, and post-yield stiffness ratio, achieving the best isolation model for a period and effective damping ratio high, and low post-yield stiffness ratio. Li et al. [127] studied the effect of the ground motion duration in a reinforced concrete frame isolated with HDRB considering the stiffness degradation of the HDRB under cyclic loading. This stiffness degradation increases under earthquakes with high intensity and long-duration ground motions.

Mokha et al. [128] have developed an experimental study on a frictional pendulum system considering two bearings materials, which modify its friction coefficient. In both cases, the isolated system was capable to resist strong earthquake motion. Then, new versions of the frictional pendulum system were developed, known nowadays as the Double Friction Pendulum System (DFPS), and even a Triple Friction Pendulum System (TFPS), which was studied by Fenz [129] and Weber [130] respectively.

4.2 Base seismic isolation system

Seismic isolation device allows the decoupling of the structure from the foundation introducing a flexible additional node at the base of the structure. This device is characterized by its high vertical stiffness and low lateral stiffness, in this way, the fundamental frequency of the isolated system is predominated by the frequency of the isolator. A structure with a single degree of freedom with a base isolator device may be analyzed as a system of two degrees of freedom (see Figure 4.2a), where the equations of motion are given by:

$$m_s\ddot{x}_s + c_s(\dot{x}_s - \dot{x}_a) + k_s(x_s - x_a) = -m_s\ddot{x}_g, \tag{4.1}$$

$$m_a\ddot{x}_a + c_a\dot{x}_a + k_a x_a - c_s(\dot{x}_s - \dot{x}_a) - k_s(x_s - x_a) = -m_a\ddot{x}_g, \tag{4.2}$$

where the variables m_a, c_a, and k_a are the mass, damping, and stiffness of the isolator respectively. The mass m_a includes the self-mass of the isolation device and the superstructure over the isolation device. $\ddot{x}_a$, $\dot{x}_a$, and x_a are acceleration, velocity, and displacement of the isolator. $\ddot{x}_g$ is the acceleration of the ground due earthquake motion. The parameters of the superstructure have been defined in section 3.2.

If the behavior associated with the isolator is analyzed as an external force, the equation of motion 4.1 takes the following form:

$$m_s\ddot{x}_s + c_s\dot{x}_s + k_s x_s = -m_s\ddot{x}_g + F_a, \quad \text{with} \quad F_a = c_s\dot{x}_a + k_s x_a. \tag{4.3}$$

If the isolator act as a rigid solid with low deformability, velocity and displacement of the isolator could be zero, therefore F_a will be approximately zero and the input on the structure will be the total earthquake force. In this sense, it is necessary that the response of the isolator helps to reduce the input force on the structure, which is possible to achieve through a large displacement associated with a flexible behavior.

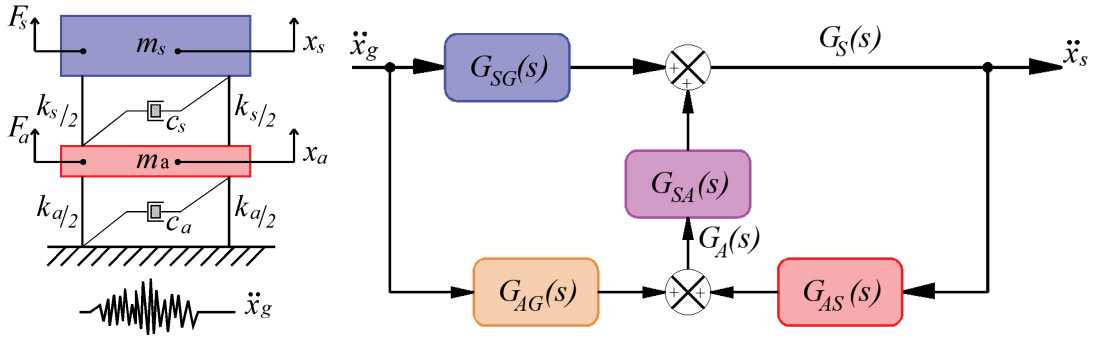

Figure 4.2: (**a**) Free body diagram for an SDOF with linear isolation, (**b**) Block diagram of the structure with linear isolation system.

The system of a structure of a single degree of freedom with an isolation device can also be analyzed as a closed loop using the Laplace domain (see Figure 4.2b). Based on equations 4.1 and 4.2, the respectively TF are given by:

$$X_s(s) = \frac{-s^2 m_s X_g(s)}{(s^2 m_s + sc_s + k_s)} + \frac{X_a(s)(sc_s + k_s)}{(s^2 m_s + sc_s + k_s)}, \tag{4.4}$$

$$X_a(s) = \frac{-s^2 m_a X_g(s)}{(s^2 m_a + s(c_a + c_s) + (k_a + k_s))} + \frac{X_s(s)(sc_s + k_s)}{(s^2 m_a + s(c_a + c_s) + (k_a + k_s))}, \tag{4.5}$$

where the TF for the structure between the input force and the isolation device, respectively, can be expressed as follows:

$$G_S(s) = G_{SG}(s) + G_{SA}(s), \tag{4.6}$$

where $G_{SG}(s)$ and $G_{SA}(s)$ in terms of acceleration are:

$$G_{SG}(s) = \frac{\ddot{X}_s(s)}{\ddot{X}_g(s)} = \frac{-s^2 m_s}{(s^2 m_s + sc_s + k_s)}, \tag{4.7}$$

$$G_{SA}(s) = \frac{\ddot{X}_s(s)}{\ddot{X}_a(s)} = \frac{(sc_s + k_s)}{(s^2 m_s + sc_s + k_s)}, \tag{4.8}$$

while the TF for the isolation device between input force and the structure, respectively, are given by:

$$G_A(s) = G_{AG}(s) + G_{AS}(s), \tag{4.9}$$

where $G_{AG}(s)$ and $G_{AS}(s)$ are:

$$G_{AG}(s) = \frac{\ddot{X}_a(s)}{\ddot{X}_g(s)} = \frac{-s^2 m_a}{(s^2 m_a + s(c_a + c_s) + (k_a + k_s))}, \tag{4.10}$$

$$G_{AS}(s) = \frac{\ddot{X}_a(s)}{\ddot{X}_s(s)} = \frac{(sc_s + k_s)}{(s^2 m_a + s(c_a + c_s) + (k_a + k_s))}. \tag{4.11}$$

However, the analysis through TF only works for a linear system, the non-linear system does not have TF defined. For the isolation device as LRB, NRB, and HDRB, many researchers have studied hysteretic behavior to achieve represent their behavior through equivalent systems. These equivalent systems allow obtaining an effective stiffness and equivalent viscous damping to analyze these types of isolators as linear systems. On the other hand, the FPS performs damping through coulomb friction, therefore, its behavior is non-linear and must be analyzed under other conditions.

A brief description of the design of the equivalent linear and non-linear devices is presented in the following sections:

4.2.1 Elastomeric isolators

All linear and non-linear isolation devices are usually designed to perform a specific displacement. This displacement is obtained from the displacement response spectrum for a desired period on the isolated system (structure + isolation device).

The rubber material used in NRB, LRB, and HDRB allows large displacements, although this material is highly non-linear and exhibits viscoelastic thixotropic constitutive properties [110], is possible analysis the rubber bearings as a linear device through equivalent properties which could be obtained from its hysteretic behavior (see figure 4.3).

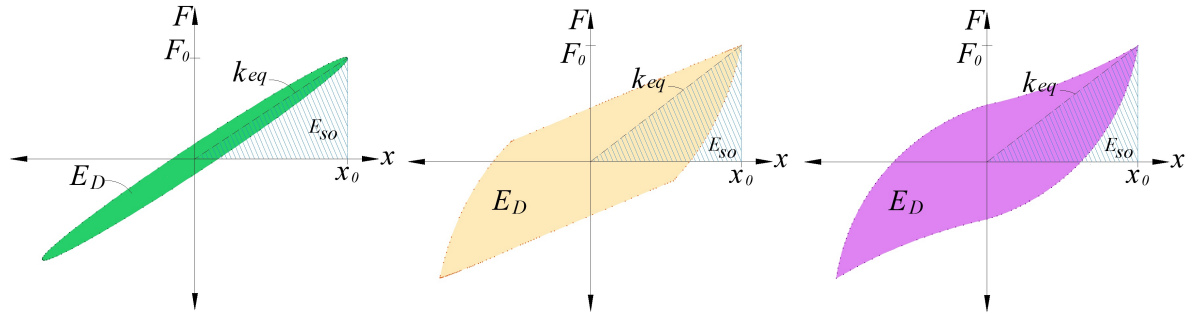

(a) Natural rubber bearing (b) Lead rubber bearing (c) High damping rubber bearing

Figure 4.3: Hysteretic curves for rubber bearings

If the stiffness is defined as $k = F/x$, from each hysteretic curve in Figure 4.3 the stiffness obtained is equivalent, while the equivalent damping coefficient ζ_{eq}, defined in section 3.9 of A. Chopra [111], is acquired from the elastic energy (E_{so}) and the dynamic energy (E_D) in one closed hysteretic loop as $\zeta_{eq} = \frac{E_D}{\pi E_{so}}$.

The numeric hysteretic curve for each type of rubber bearing system mentioned can be built through the following equations:

Natural Rubber Bearing

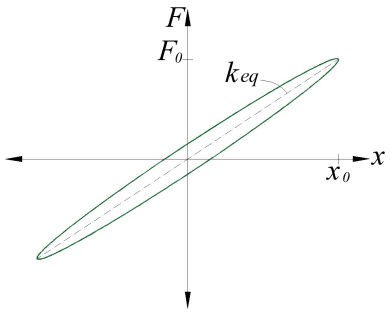

Lateral Stiffness:

$$k_{eq} = \frac{G_{eq} \cdot A}{H},$$

Vertical Stiffness:

$$k_v = \frac{E_c \cdot A}{H},$$

$$E_c = \frac{E(1 + 2kS^2)}{1 + E(1 + 2kS_1^2)/E\infty},$$

where G_{eq} is the shear module. A is the area of the bearing. H is the height of the bearing. E_c is the instantaneous compression modulus of the rubber. k modulus rubber. S factor shape if it is rectangular, circular or square.

Lead Rubber Bearing

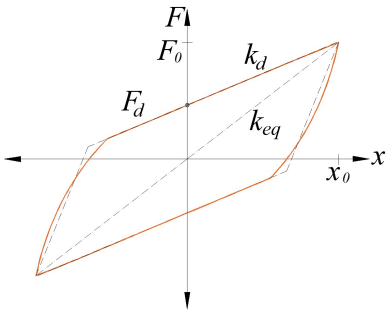

Lateral Stiffness:

$$F_d = C_{qd} \cdot \sigma_L \cdot A_L,$$

$$k_d = (k_r + k_p),$$

$$k_r = \frac{G_{eq} \cdot A_r}{H},$$

$$k_p = \frac{\alpha_p \cdot A_p}{H},$$

$$k_{eq} = \frac{F_d}{\gamma \cdot H} + k_d,$$

Vertical Stiffness:

$$k_v = \frac{\alpha_v \cdot E_c \cdot A}{H},$$

where C_{qd} is the correlation factor due strain. A_L the area of the lead. σ_L : the shear stress at yield of lead. k_r the shear stiffness of laminated. k_p the additional shear stiffness by lead plug. A_r the effective plane area. A_p the lead plug plane area. γ the shear strain. α_v the young's modulus correction factor and $A : A_r + A_p$

High Damping Rubber Bearing

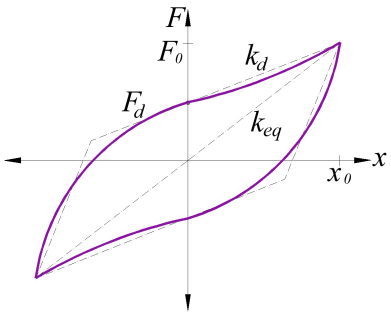

Lateral Stiffness:

$$k_{eq} = \frac{G_{eq} \cdot A}{H},$$

$$F_d = u \cdot k_{eq} \cdot H \cdot \gamma,$$

$$k_d = k_{eq} \cdot (1 - u),$$

Vertical Stiffness:
Similar to natural rubber bearing.

where G_{eq} is the shear module dependent on shear strain amplitude and u dependent on shear strain amplitude.

4.2.2 Friction pendulum isolator

The sliding devices or FPS can not be represented through the TF such as in equation 3.37 and 3.38. In the case of the sliding device, the friction coefficient depends directly on the sign of the velocity; even the self friction coefficient changes at each time step depending on the velocity on the plate [129]. Therefore, the sliding device has to be analyzed in the time domain. The force equation for an FPS is given by:

$$F = k_h x_a \pm F_f, \tag{4.12}$$

the variable k_h is the horizontal stiffness of the FPS define in equation (4.13), which directly depends on the effective radius R_{eff}; while at the same time, R_{eff} depends on the curvature of the concave plate and the radius R that depends on the fundamental period of the FPS defined in equation (4.14).

$$k_h = \frac{W}{R_{eff}}, \tag{4.13}$$

$$R = g\left(\frac{T}{2\pi}\right)^2. \tag{4.14}$$

Figure 4.4 shows the geometry parameters for a FPS with and without restraining ring.

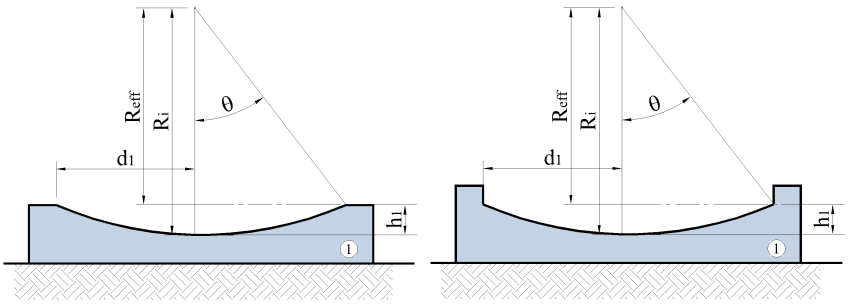

(a) (b)

Figure 4.4: Geometric parameters. **(a)** FPS, **(b)** FPS with ring

According to Ponzo [122] and Domenico [121], the friction force F_f develops two phases, pre-sliding and sliding. The mathematical expression for each phase is given by:

$$F_f = \begin{cases} k_h \cdot d & \text{Pre-sliding} \\ sign(\dot{x}_a) \cdot \mu \cdot W & \text{Sliding} \end{cases}, \tag{4.15}$$

in which the stiffness k_h will be present during the pre-sliding phase, and is characterized by a very high initial value, about two orders of magnitude larger than the sliding stiffness k_a. The parameter μ is the dynamic friction coefficient, defined as $\mu(\dot{x}_a) = \mu_{max} - (\mu_{max} - \mu_{min})e^{-a|\dot{x}_a|}$. Nevertheless, for this thesis this variable will be considered as constant.
The velocity $\dot{x}_a$ will be analyzed in either direction according to the displacement of the upper plate. During earthquake excitation, the friction force acts in the opposite direction. However, once the earthquake has ended and the sliding stiffness is reaching the centered position, the friction force will act against this behavior. This effect could produce a residual displacement for a high value of friction coefficient at the sliding surface.

Many researchers have studied the response of the FPS, considering equivalent damping for an FPS as in the case of the rubber bearings, which could be simple in the case of a first-generation FPS. However, second (DFPS) and third TFPS) generation of FPS, perform a hysteretic behavior with different slopes according to the geometry of the plates, and the friction coefficient in each surface (see Figure 4.5 and 4.6). In this sense, this type of isolators should be analyzed in the time domain.

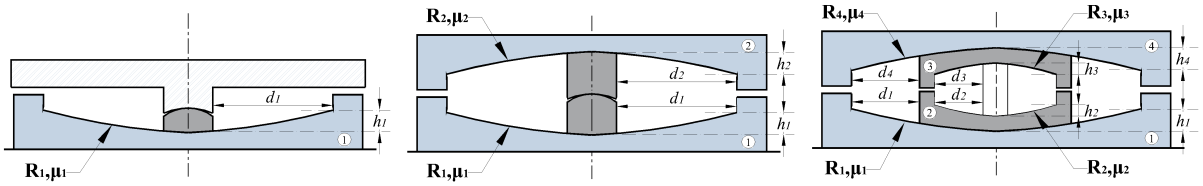

(a) Simple FPS (b) Double FPS (c) Tripe FPS

Figure 4.5: Generations of FPS

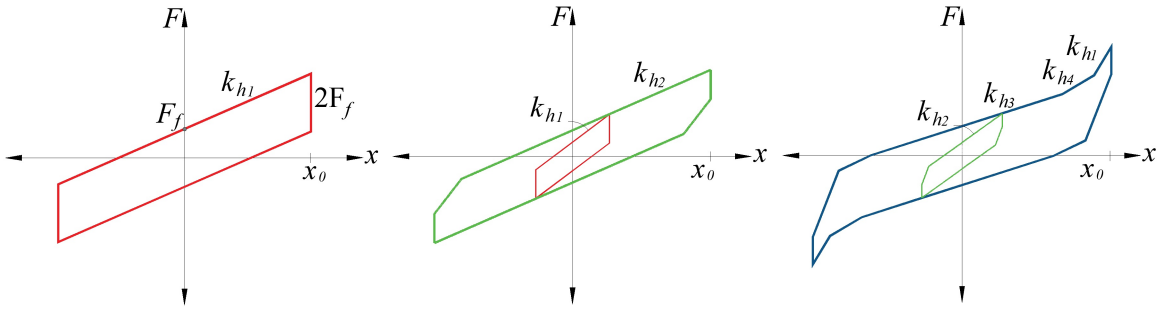

(a) FPS (b) Double FPS (c) Triple FPS

Figure 4.6: Hysteretic curves of FPS

4.3 Semi-active isolation system

A SDOF model of a structure with an isolator system formed by an FPS and a viscous damper is adopted as shown in Figure 4.7, where m_s, c_s and k_s are the mass, damping coefficient and stiffness of the structure, x_s and x_a are the structure and bearing plate displacement relative to the base movement and $\ddot{x}_g$ is the ground acceleration.

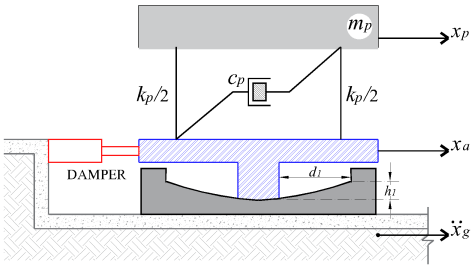

Figure 4.7: Schematic model of an isolated-structure with a friction pendulum system (FPS) and a damper.

In this section the study of a SFPS is carried out considering three models: (i) the structure with an FPS modelled by k_a, F_f and a bearing plate mass, m_a, (ii) the structure with an FPS and a viscous damper with a damping coefficient c_a, denoted as FPS+VD, and (iii) the structure with an FPS and a time-varying damping coefficient which is updated following a particular semi-active control law, denoted as FPS+SD. Figure 4.8 illustrates these aforementioned cases.

The equation of motion of a structure modeled as a SDOF subjected to a base movement is:

$$m_s\ddot{x}_s + c_s(\dot{x}_s - \dot{x}_a) + k_s(x_s - x_a) = -m_s\ddot{x}_g, \tag{4.16}$$

where " $\dot{}$ "and " $\ddot{}$ "indicates the derivatives for velocity and acceleration, respectively. Note that Equation (4.16) is the same for the three cases presented in Figure 4.8.

The equation of motion of the bearing plate considering a mass of m_a is now derived for the three cases. For the case of a single FPS isolator, this equation is as follows:

$$m_a\ddot{x}_a + F_f(sign(\dot{x}_a)) + k_a x_a - c_s(\dot{x}_s - \dot{x}_a) - k_s(x_s - x_a) = -m_a\ddot{x}_g, \tag{4.17}$$

for the FPS+VD is:

$$m_a\ddot{x}_a + c_a\dot{x}_a + F_f(sign(\dot{x}_a)) + k_a x_a - c_s(\dot{x}_s - \dot{x}_a) - k_s(x_s - x_a) = -m_a\ddot{x}_g, \tag{4.18}$$

in which c_a is a fixed damping coefficient of the viscous damper, and finally, for the FPS+SD, the equation takes the following form:

$$m_a\ddot{x}_a + c_{semi}\dot{x}_a + F_f(sign(\dot{x}_a)) + k_a x_a - c_s(\dot{x}_s - \dot{x}_a) - k_s(x_s - x_a) = -m_a\ddot{x}_g, \quad (4.19)$$

in which $c_{semi}(t)$ is continuously updated following a control law. Two semi-active control laws are studied in this paper: phase control and energy-predictive-based control law.

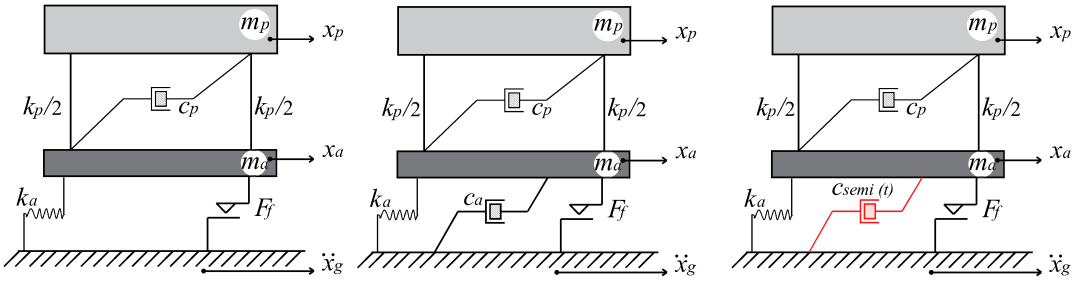

(a) FPS (b) FPS+VD (c) FPS+SD

Figure 4.8: Considered Models.

4.4 Control laws

In this section two control laws are considered, the aim consists of evaluating the effectiveness of the phase control law whose operation depends on the measurement of two control points, while the Energy-Predictive-Based control requires considering the response of all degrees of freedom on the structure. Each control law is explained in the next sections.

4.4.1 Phase control for semi-active isolation systems

The semi-active control law proposed by Koo et al. [66] for semi-active TVAs has been reformulated to semi-active vibration isolation. More concretely, the concept of the displacement-based groundhook control law has been applied to the relative movement between the ground and the bearing plate. Figure 4.9 illustrates the phase control logic.

Basically, according to the ground displacement (or the concave plate displacement) and the relative velocity between the ground and the bearing plate, when both are separating, the damper force should pull the structure to the equilibrium point (ON), and, when both are coming together, the damper force should leave the structure free to reach to the equilibrium point (OFF). Thus, assuming absolute magnitudes the following phase control law is derived:

$$\begin{array}{lll} x_g \cdot (\dot{x}_g - \dot{x}_a) \geq 0 & \Rightarrow & c_{min} \quad \text{(normal functioning)} \\ x_g \cdot (\dot{x}_g - \dot{x}_a) < 0 & \Rightarrow & c_{max} \quad \text{(blocking functioning)} \end{array}, \quad (4.20)$$

in which c_{min} indicates normal functioning and the control law is disabled, and c_{max} indicates blocking functioning and the control law maximizes the damper force.

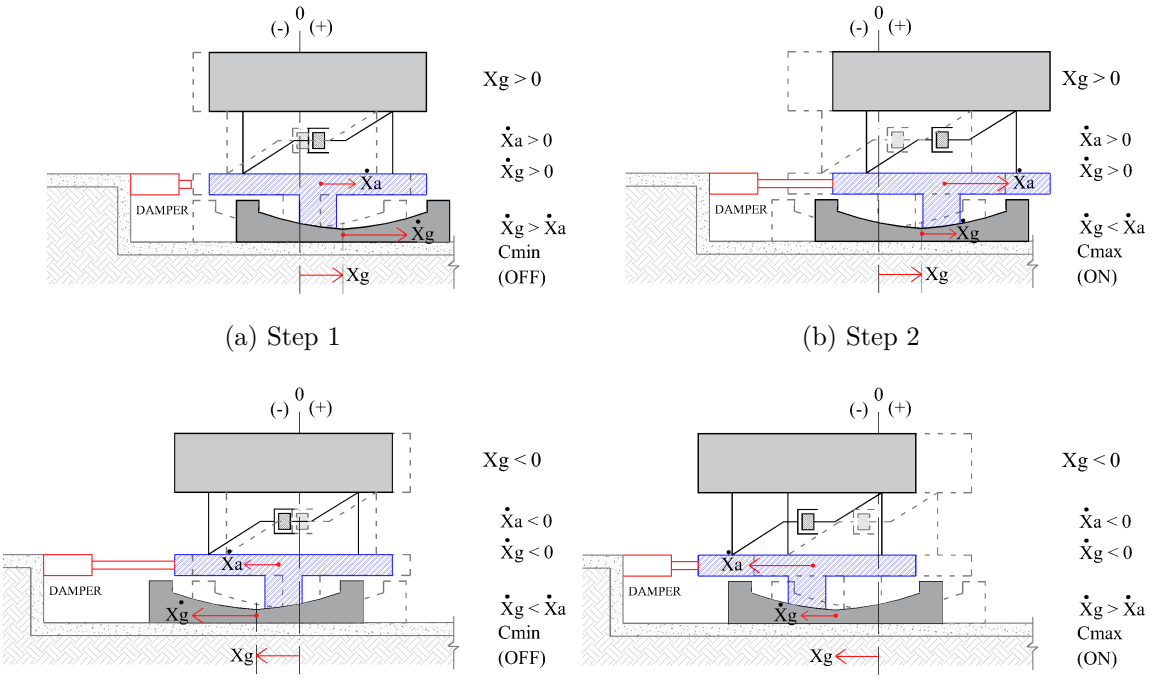

(a) Step 1 (b) Step 2

(c) Step 3 (d) Step 4

Figure 4.9: Illustrations of the phase control logic.

The groundhook-based phase control can be modified by substituting ground displacement by ground acceleration and changing the sign of Inequation (4.20). Furthermore, since relative magnitudes to the base movement are assumed (Equations (4.16)-(4.19)), the phase control law adopted in this work is as follows:

$$\begin{aligned} \ddot{x}_g \cdot (\dot{x}_a) \geq 0 \quad &\Rightarrow \quad c_{min} \quad \text{(normal functioning)} \\ \ddot{x}_g \cdot (\dot{x}_a) < 0 \quad &\Rightarrow \quad c_{max} \quad \text{(blocking functioning)} \end{aligned} . \tag{4.21}$$

Note that this control law is fairly simple and clearly geared to practical implementation due to the measured real-time magnitudes: the concave plate acceleration (instead of its displacement) and the bearing plate velocity.

4.4.2 Full-state feedback control

Zelleke and Matsagar [112] have recently presented an energy-predictive-based control law applied to semi-active TVAs. Taking as the main assumption that the ground acceleration remains constant for a time interval (sampling time), the energy is computed for both

c_{min} and c_{max}. Thus, the estimation of mechanical energy, which is usually known in the energy-based design methodology as the elastic vibrational energy [113], is derived. Hence, the prediction which produces the minimum mechanical energy provides the desirable damping for the time interval considered. This assumption is mathematically expressed as:

$$\ddot{x}_g(t + \Delta t) = \ddot{x}_g(t), \tag{4.22}$$

with Δt being the sampling time and t indicates a time instant. Thus, under this assumption, the mechanical energy estimated at the next time instant is:

$$\check{E}_m(t + \Delta t) = \check{E}_k(t + \Delta t) + \check{E}_e(t + \Delta t), \tag{4.23}$$

in which E_m, E_k, and E_e are the mechanical, kinetic, and elastic strain energy, respectively, and "ˇ"indicates that it is an estimated value. So, the control law can be defined as:

$$\begin{array}{lcll} \check{E}_m(t + \Delta t, c_{min}) < \check{E}_m(t + \Delta t, c_{max}) & \Rightarrow & c_{min} & \text{(normal functioning)} \\ \check{E}_m(t + \Delta t, c_{min}) > \check{E}_m(t + \Delta t, c_{max}) & \Rightarrow & c_{max} & \text{(blocking functioning)} \end{array}. \tag{4.24}$$

Some remarks about this control law are: (i) contrary to the phase control, the global isolated-structure behavior is considered, (ii) the implementation requires to measure the movement of all the degrees of freedom, (iii) the displacement needed for the computation of elastic energy is difficult to be measured experimentally, (iv) since this is a model-based control law, a real-time response accurate model is needed and consequently, the computational burden will be a critical issue, and finally, (v) the energy computation may include the isolator energy or not.

4.5 Performance assessment of the semi-active isolation system

The proposed methodology for the design of the isolator is presented hereafter. It consists of a two-step design process that makes use of two different excitations (serviceability and design earthquake), which are firstly described in Section 4.5.1. Secondly, different Performance Indexs (PIs) are defined for both their use within the design process and comparison between design cases. Thirdly, a sensitivity analysis is undergone in Section 4.5.2 in order to motivate the design process presented in Section 4.5.2.

4.5.1 Earthquake excitation

To carry out the design of the isolator, two excitations are considered taking into account the different requirements depending on the level of the ground motion: (i) low-intensity ground motion, denoted as serviceability earthquake and (ii) design earthquake for a particular seismic zone. Several synthetic artificial accelerograms are generated from a

design spectrum (which is taken here from the Maximum Considered Earthquake (MCE) as it is defined in code American Society of Civil Engineering (ASCE) 7-16 [114]).

Serviceability Earthquake

The excitation signal considered for low-intensity ground motion corresponds to earthquakes of intensity less or equal to type VI, with a magnitude from $5.0 < \text{Mw} < 5.6$ and acceleration (g) between 0.06 to 0.07, characterized by causing minor damages and a maximum of 120 earthquakes per year. Thus, the Livermore earthquake of magnitude Mw = 5.5, that shocked the San Francisco Bay in January 1980, have been used here. Figure 4.10 shows the input ground acceleration of this earthquake.

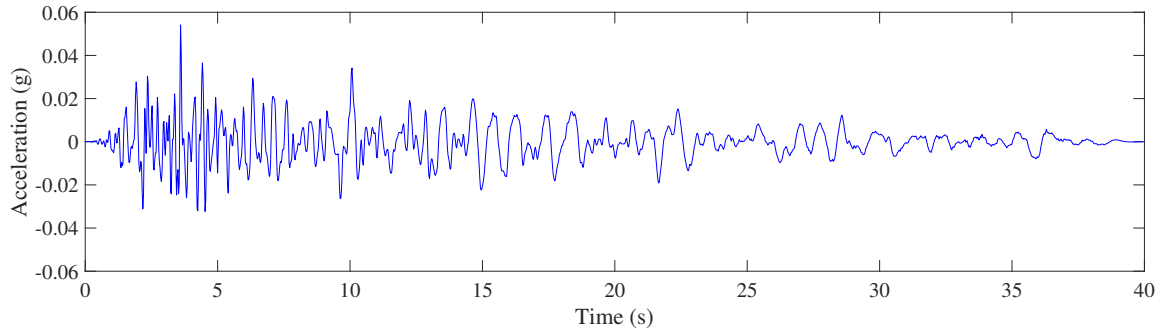

Figure 4.10: Input ground acceleration of the serviceability earthquake (Livermore earthquake, 1980).

Design Earthquake

The second input considered is the ground acceleration due to the design earthquake. The response of the structure with the isolator to this excitation becomes crucial for the design. Therefore, 15 artificially generated earthquakes obtained from the decomposition of the MCE defined in ASCE 7-16 with different random phase angle for each frequency are used. All of them have a Peak Ground Acceleration (PGA) of 0.40 g, resulting in an intensity between VIII and IX and a magnitude around Mw = 7.

The ACELSIN© [115] software, which makes use of the methodology proposed by Gasparini and Vanmarcke [116], is used to obtain the time histories for each artificial earthquake. This methodology uses the decomposition of the spectrum shown by a black line in Figure 4.11a to generate fifteen accelerograms corresponding to the same seismic zone. Each Time History (TH) is also integrated and superposed over the design spectrum in the same figure. The methodology also requires an intensity function (that is, a TH envelope), obtained from an earthquake, of similar magnitude and at the same location, to be applied to each of the generated THs. In this case, "El Centro Earthquake", which corresponds to the same seismic zone and magnitude of the MCE, is chosen to illustrate the methodology. A sequence with all of them is shown in Figure 4.12a. A zoom of the seventh event is plotted in Figure 4.12b. In order to check how these events fit the MCE, the spectra obtained from each individual TH are overlapped in Figure 4.11a. Finally,

Figure 4.11b shows the all Fast Fourier Transforms (FFT) of each artificial earthquake event in order to show their frequency content.

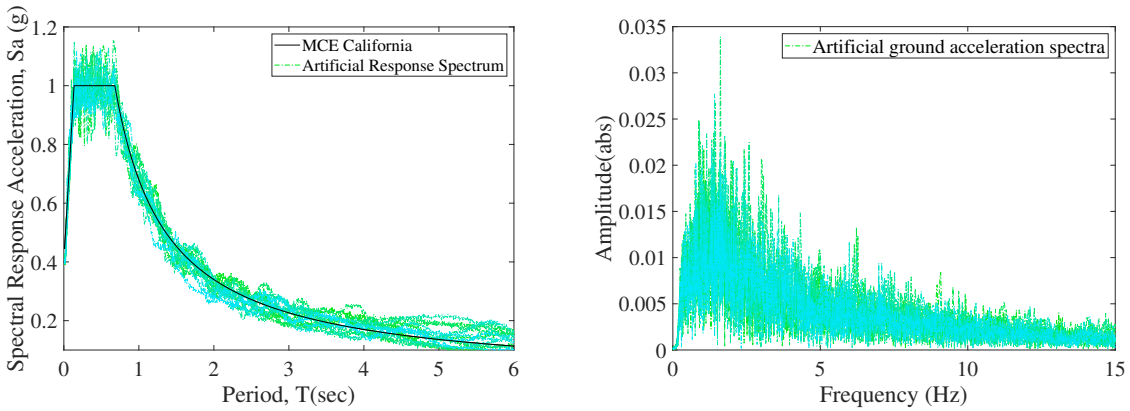

(a) Design response spectrum and response spectra (b) FFT of the artificial earthquakes

Figure 4.11: Design response spectrum and Fast Fourier Transforms (FFT) of the input ground acceleration.

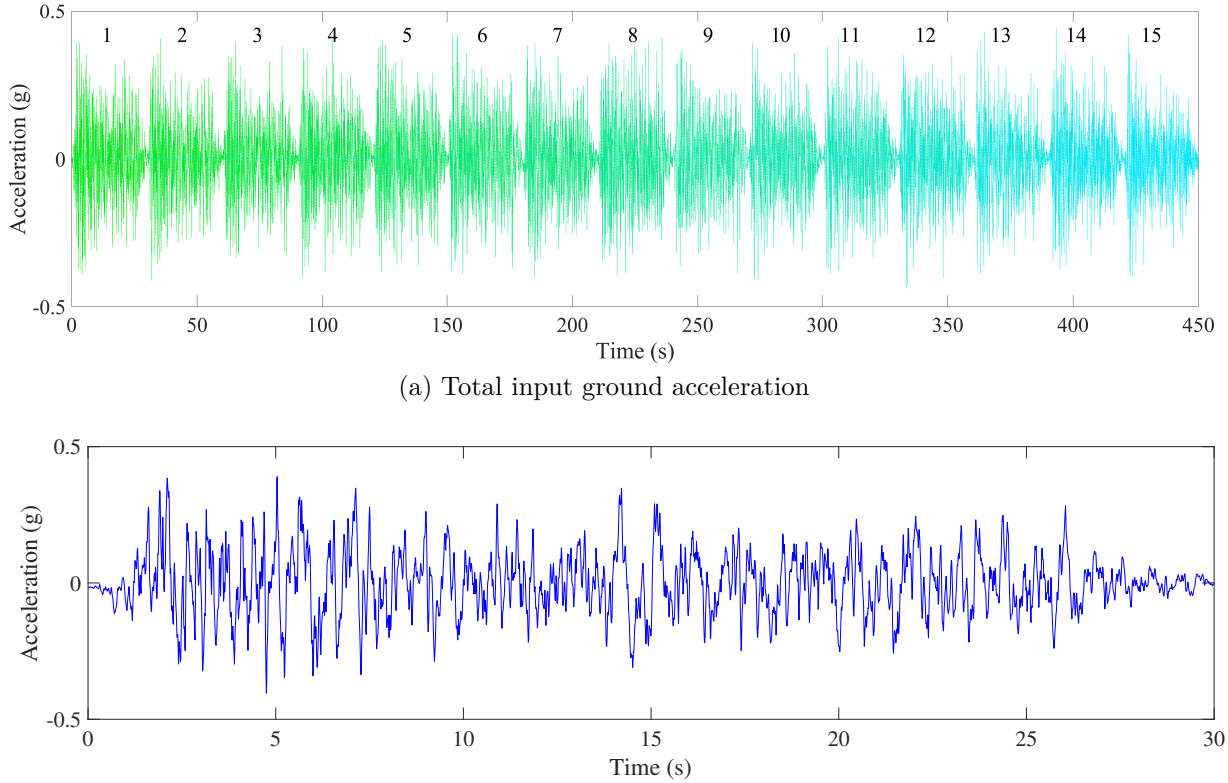

(a) Total input ground acceleration

(b) Ground acceleration of the seventh event

Figure 4.12: Input ground acceleration of the design earthquake.

4.5.2 Performance analysis and optimization problem

This section introduces the PIs used to evaluate the isolator performance and to define the performance function for the optimization problem. The PIs are the structure acceleration (J_1), the base displacement (bearing plate displacement) (J_2), the inter-story drift (J_3), and the mechanical energy (J_4). The subindexes P and RMS will indicate peak value and root mean square value, respectively, of the PIs. Additionally, the subindexes S and T will indicate the integral value of the mechanical energy only of the structure and of the total system (isolator + structure), respectively. Each PIs is normalized to the response of the non-isolated structure identified by symbol " $\widehat{}$ ", thus, ($\ddot{\widehat{x}}_s$, $\widehat{x}_s$, $\widehat{E}_m$) are the acceleration, displacement, and mechanical energy of the non-isolated structure, respectively. Different from the former magnitudes, the bearing displacement (x_a) is normalized to the minimum value of displacement capacity "d_1 "(see Figure 4.4), obtained for the maximum frequency limit (that is, the minimum plate size) of the FPS within the optimization process. Therefore, J_2 will penalize greater sizes of the FPS. Hence, the definition of the PIs is as follows:

→ Normalized Peak Acceleration

$$J_{1,P} = \frac{max|\ddot{x}_s(t)|}{max|\ddot{\widehat{x}}_s(t)|},$$

→ Normalized RMS Acceleration

$$J_{1,RMS} = \frac{RMS(\ddot{x}_s(t))}{RMS(\ddot{\widehat{x}}_s(t))},$$

→ Normalized Bearing Displacement

$$J_{2,P} = \frac{max|x_a(t)|}{max|d_1(t)|},$$

→ Normalized RMS Bearing Displacement

$$J_{2,RMS} = \frac{RMS(x_a(t))}{RMS(d_1(t))},$$

→ Normalized Structure Drift

$$J_{3,P} = \frac{max|x_s(t) - x_a(t)|}{max|\widehat{x}_s(t)|},$$

→ Normalized RMS Structure Drift

$$J_{3,RMS} = \frac{RMS(x_s(t) - x_a(t))}{RMS(\widehat{x}_s(t))},$$

→ Normalized Mechanical Energy Structure

$$J_{4,S} = \frac{\int_0^t E_{m,S}(t)\,dt}{\int_0^t \widehat{E}_{m,S}(t)\,dt},$$

→ Normalized Mechanical Energy System

$$J_{4,T} = \frac{\int_0^t E_{m,T}(t)\,dt}{\int_0^t \widehat{E}_{m,S}(t)\,dt}.$$

Sensitivity Analysis

Previously to set the design process, a sensitivity analysis is carried out. Firstly, the single FPS (Figure 4.8a) is analyzed under the serviceability earthquake in order to study how the friction coefficient affects the FPS under low-intensity earthquakes. Thus, a value of μ will be chosen in order to avoid breakaway effects. Secondly, the FPS+VD and the phase-controlled FPS+SD are studied using the value of μ obtained in the first analysis. For the passive one, the viscous damping c_a with respect to the frequency of the pendulum f_a is studied. For the smart version, the unblocking damping (normal functioning) c_{min} with respect to f_a is analyzed (see Equation (4.21)).

Table 4.1 summaries the parameters adopted for the sensitivity analysis.

Table 4.1: Parameters for the sensitivity analysis.

Modal Parameters			
Structure		**Value**	
m_s	Mass	24,000	kg
f_s	Frequency	2.0	Hz
ζ_s	Damping ratio	1.0	%
c_s	Damping	6031.9	kg/s
k_s	Stiffness	3789.9×10^3	N/m
FPS+VD/FPS+SD		**Value**	
m_a	Mass	240	kg
f_a	Frequency	[0.50 to 1.10]	Hz
μ	Friction coefficient	[0.01 to 0.20]	%
c_a	Viscous damper	$[0.01c_s$ to $0.50c_s]$	kg/s
c_{min}	Semi-active damper	$[0.01c_s$ to $0.50c_s]$	kg/s
c_{max}	Semi-active damper	$10c_s$	kg/s

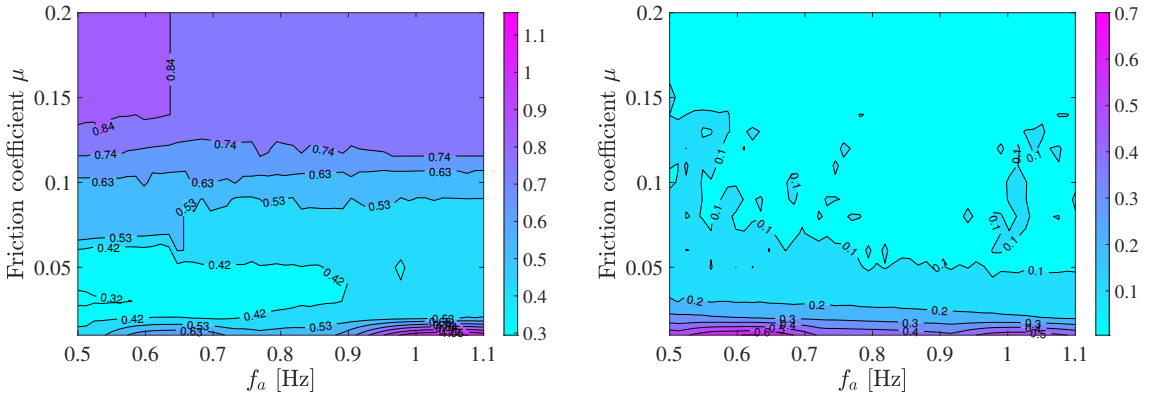

(a) $J_{1,P}$ (b) $J_{2,P}$

Figure 4.13: Sensitivity analyses. Response of the single FPS under the serviceability earthquake.

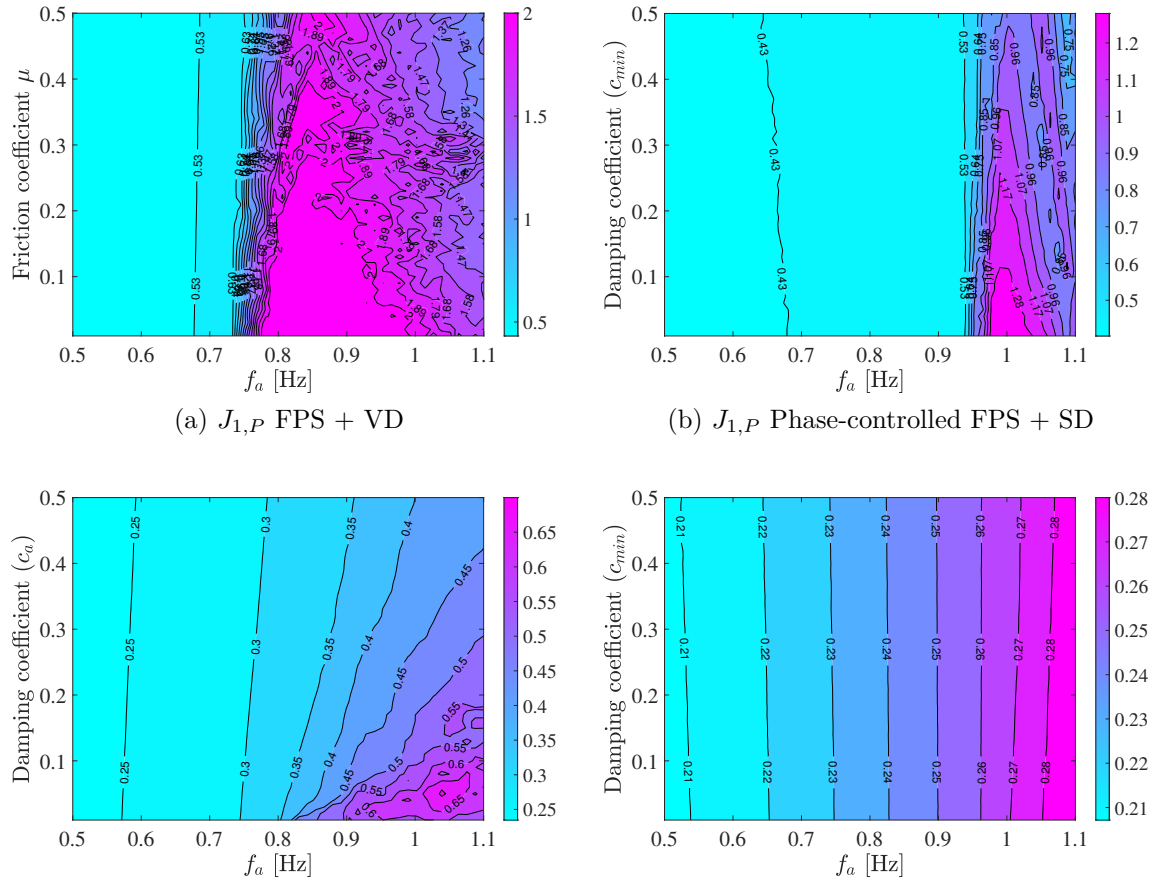

(a) $J_{1,P}$ FPS + VD (b) $J_{1,P}$ Phase-controlled FPS + SD

(c) $J_{1,RMS}$ FPS + VD (d) $J_{1,RMS}$ Phase-controlled FPS + SD

Figure 4.14: J_1 for FPS+VD and phase-controlled FPS+SD under the design earthquake.

$J_{1,P}$ and $J_{2,P}$ are shown in Figure 4.13 for the single FPS under the serviceability earthquake. It can be observed that a low friction coefficient between 0.03 - 0.06 provides better performance under the low-intensity earthquake. In Figure 4.13a, the peak acceleration $J_{1,P}$ is shown, and values of $J_{1,P}$ between $0.32 - 0.53$ can be achieved for all f_a values if $\mu \in (0.03, 0.06)$. Focusing on $J_{2,P}$ (Figure4.13b), a higher displacement demand occurs for μ values lower than 0.03. From Figure 4.13a, it can be observed that higher values of μ produces a stepwise degradation of the performance and will get the isolator involved in undesirable residual displacements leading to breakaway effects.

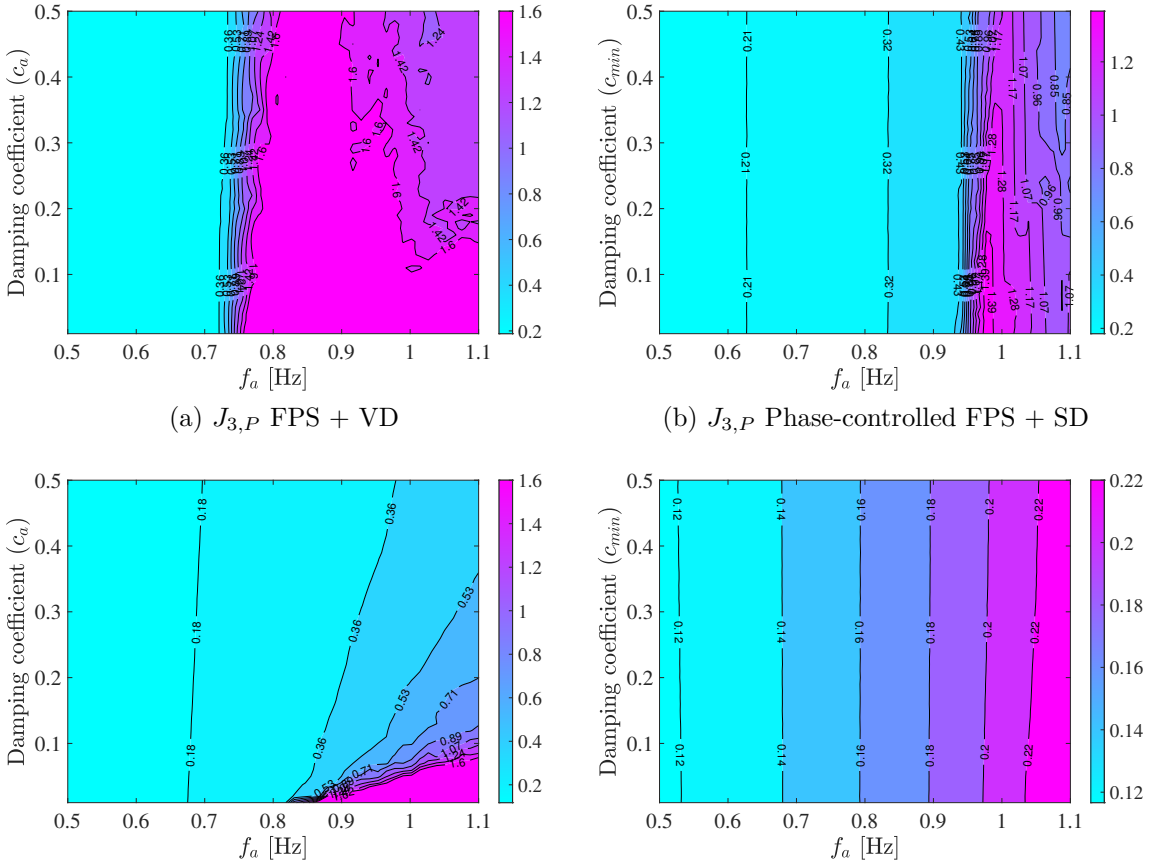

(a) $J_{3,P}$ FPS + VD

(b) $J_{3,P}$ Phase-controlled FPS + SD

(c) $J_{3,RMS}$ FPS + VD

(d) $J_{3,RMS}$ Phase-controlled FPS + SD

Figure 4.15: J_3 for FPS+VD and phase-controlled FPS+SD under the design earthquake.

Now, the sensitivity analysis for the FPS+VD and for the phase-controlled FPS+SD are carried out using $\mu = 0.05$. Figures 4.14 and 4.15 show the contour plots of J_1 and J_3 for both cases. The values of J_1 are significantly smaller for the semi-active version. In both cases, from smaller plate sizes than a particular one, the isolated structure performance (Figure 4.14a,b) may be worse than the non-isolated one. However, the semi-active controlled version improves the performance for a broad range of plate sizes. From Figure 4.14b, it can be observed that the performance of the FPS+SD is almost constant from a

minimum size of the FPS (maximum value of f_a). Hence, any f_a smaller than 0.85 Hz will provide the best performance. From the RMS values (Figure 4.14d), the isolator shows a performance that is almost independent of c_{min}. However, this fact does not happen with the passive version (Figure 4.14c). Additionally, the influence of f_a (the concave plate size) is quite low for a semi-active case. Interestingly, the contour plots for J_3, the inter-story drift, show similar qualitative behavior to J_1, showing a robust behavior for the semi active version.

Finally, it is worthy to mention that the contour plots obtained for phase-controlled and energy-controlled FPS+SD are quite similar. As an example, and for comparison with Figure 4.15d, Figure 4.16 shows $J_{3,RMS}$ for the energy-controlled FPS+SD.

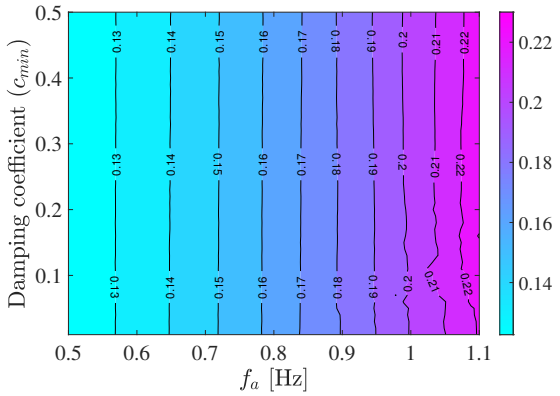

Figure 4.16: $J_{3,RMS}$ for energy-controlled FPS+SD under the design earthquake.

A two-step design process based on minimizing two performance functions ϕ_1 and ϕ_2 is proposed. The objective is to design, firstly the friction coefficient μ and secondly, the plate size (the pendulum natural frequency f_a) and the normal functioning damping coefficient c_a (for the passive version), or c_{min} (for the semi-active version). The first step consists of minimizing a performance function ϕ_1 and obtaining the optimum friction coefficient μ for the single FPS (without damper) under serviceability conditions in such a way that good re-centering capacity is assured. In a second step, under the design earthquake, the frequency of the pendulum and the normal function damping coefficient are obtained by minimizing a performance function ϕ_2. Thus, the two-step design process is as follows:

- Step 1. Single FPS (Figure 4.8a) under the serviceability earthquake. The performance function ϕ_1 is defined as:

$$\phi_1(\underline{z}, \mu, f_a) = a_1 J_{1,P} + a_2 J_{2,P}, \tag{4.25}$$

in which $\underline{z} = [m_s, k_s, c_s, m_a]$, $a_1 = a_2 = 0.50$ are the weighting factors. The optimum value of μ for the range of f_a (plate sizes) considered is calculated from the:

$$\min_{\mu} \quad \phi_1(\underline{z}, \mu, f_a) \tag{4.26}$$

$$\text{suject to } f_a(\underline{z}) \in [f_{a,min}; f_{a,max}], \forall_\mu \in [\mu_{min}; \mu_{max}]. \tag{4.27}$$

- Step 2. FPS+VD or FPS+SD (Figure 4.8b,c) under the design earthquake. The performance function ϕ_2 is defined as:

$$\phi_2(\underline{z}, c_{min}, f_a) = \sum_{i=1}^{3} a_i J_{i,P} + \sum_{i=1}^{3} b_i J_{i,RMS}, \tag{4.28}$$

with $\sum_{i=1}^{3}(a_i + b_i) = 1$ and $\underline{z} = [m_s, k_s, c_s, m_a, \mu, c_{max}]$, where a_i and b_i are the weighting factors to balance the effects between the peak and RMS PIs, respectively. Generally speaking, ϕ_2 is a performance function that considers a balance between structural magnitudes (J_1 and J_3), acceleration and inter-story drift, and the plate displacement J_2, since this magnitude is normalized to the minimum plate size displacement. The minimization of ϕ_2 will reduce simultaneously, the structural magnitudes and the plate size. In this sense, the continuous movement of the bearing plate ($J_{2,RMS}$) should not be penalized ($b_2 = 0$), while the peak value of the plate displacement ($J_{2,P}$) should be penalized ($a_2 = 1/6$) in order to choose the minimum plate size that provides good performance (as it was shown in Figures 4.14 and 4.15).

Regarding the structure performance, ϕ_2 pays attention mainly to the peak of the inter-story drift $J_{3,P}$ ($a_3 = 1/3$) since this magnitude is crucial to avoid structural damages during the event. The remainder of the PIs, peak and RMS structure acceleration ($J_{1,P}$, and $J_{1,RMS}$) and the RMS of the inter-story drift are equally penalized (1/6) with a weight factor which is half of the peak of the inter-story drift. Thus, the optimum damping coefficient c_a for FPS+VD or c_{min} for FPS+SD (when the MR damper is normally functioning), and the pendulum natural frequency f_a(which defines the plate size) are calculated from the minimization of ϕ_2 as follows:

$$\min_{c_{min}, f_a} \quad \phi_2(\underline{z}, c_{min}, f_a), \tag{4.29}$$

$$\text{suject to } f_a(\underline{z}) \in [f_{a,min}; f_{a,max}], c_{min} \in [0; c_{max}]. \tag{4.30}$$

Note that $c_{min} = c_a$ in Equation (4.29) if the FPS+VD is being designed. Note also that the proposed design process requires two sequential inputs, first, a low-intensity earthquake followed by a design earthquake corresponding to the considered seismic area. The selection of the design earthquake according to current codes has been explained in Section 4.5.1.

4.5.3 Design, results and analysis

The optimization process for the design of the isolated-structure is now applied to the structure described in Table 4.1. The isolator parameters considered for the optimization

are also presented in the table. The optimization process has been run for three cases: (i) FPS+VD in which the optimization parameters are, f_a and c_a, (ii) FPS+SD with phase control and (iii) FPS+SD with energy-predictive-based control. The optimization parameters for the last two cases are f_a and c_{min} (which corresponds to a damping ratio ζ_{min}).

From Step 1 of the optimization problem, a friction coefficient of $\mu = 0.05$ has been obtained. Note that this value is the same for the three cases. Thus, Table 4.2 collects the configuration parameters once Step 2 is run and the minimum values of the performance function (ϕ_2) (Equation (4.29)) together with its reduction with respect to the non-isolated structure. Furthermore, for comparison reasons, two more cases are included in this table, the optimum single FPS using $\mu = 0.05$ (low-friction FPS) and $\mu = 0.20$ (high-friction FPS), which correspond to the optimum friction coefficients for the serviceability and design earthquake, respectively. Note that, when a single FPS is subjected to the design earthquake, the optimum performance function is achieved for the maximum possible friction coefficient μ_{max} ($\mu = 0.20$) used within the optimization problem (see Table 4.1).

Table 4.3 summarizes the results obtained for all the PIs. The PI based on the mechanical energy, $J_{4,S}$ and $J_{4,T}$ are also presented in the table.

Table 4.2: Optimum parameters for the isolator configurations studied.

System	f_a	μ	$\zeta_{(c_a,c_{min})}$	ϕ_2	**Reduction (%)**
Non-isolated structure	-	-	-	0.833	0.00
$FPS_{\mu=0.05}$	0.671	0.05	-	0.834	0.00
FPS+VD	0.647	0.05	0.500	0.791	5.04
FPS+SD (Phase control)	0.684	0.05	0.480	0.564	32.29
FPS+SD (Energy control)	0.745	0.05	0.240	0.571	31.45
$FPS_{\mu=0.20}$	0.671	0.20	-	0.529	36.49

Table 4.3: Performance indexes (PIs) for the optimum configurations under the design earthquake.

System	$J_{1,P}$	$J_{1,RMS}$	$J_{2,P}$	$J_{2,RMS}$	$J_{3,P}$	$J_{3,RMS}$	$J_{4,S}$	$J_{4,T}$
Non-isolated structure	1.000	1.000	-	-	1.000	1.000	1.000	1.000
$FPS_{\mu=0.05}$	0.522	0.446	3.111	0.975	0.313	0.297	0.848	0.178
FPS+VD	0.478	0.419	3.015	0.886	0.286	0.263	0.692	0.141
FPS+SD (Phase control)	0.434	0.359	1.891	0.469	0.239	0.225	0.209	0.052
FPS+SD (Energy control)	0.473	0.385	1.778	0.413	0.273	0.245	0.173	0.051
$FPS_{\mu=0.20}$	0.476	0.408	1.420	0.257	0.274	0.321	0.081	0.033

From Tables 4.2 and 4.3, it can be observed that both semi-active designs behave better than the FPS+VD and much better than the FPS with $\mu = 0.05$. To achieve similar results as to the semi-active version with the single FPS, much higher values of

μ are needed, and consequently, the behavior under lower intensity earthquakes will be drastically affected. Paying attention to $J_{3,P}$, which is the main PI considered within the performance function, the phase-controlled FPS+SD shows the best performance, achieving a reduction of 76%.

The CDF curves for the bearing plate displacement and for the inter-story drift using the optimum configurations of Table 4.2 under the design earthquake (Figure 4.17) and the serviceability earthquake (Figure 4.18) are computed and plotted. The CDFs indicate the percentage of time of non-exceedance of a value of the considered magnitude.

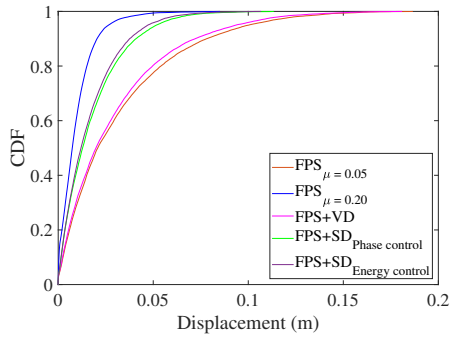

(a) CDF of the bearing displacements

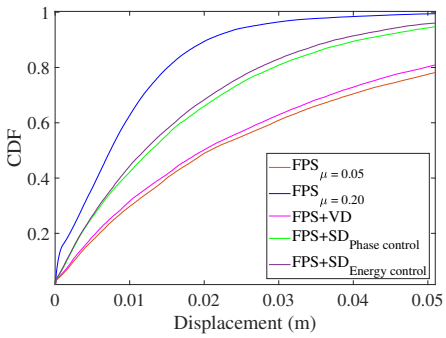

(b) Zoom CDF of the bearing displacements

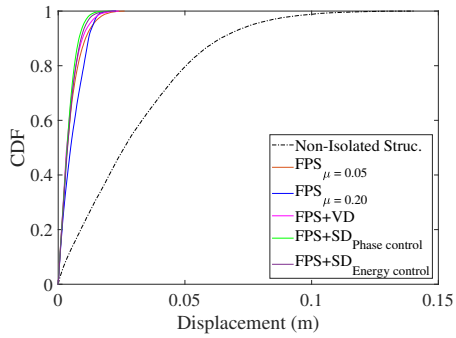

(c) CDF of the drift response of the structure

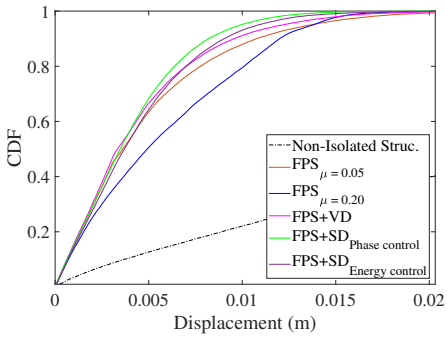

(d) Zoom to CDF of the drift response of the structure

Figure 4.17: Cumulative distribution function (CDF) of bearing plate displacement and drift under the design earthquake.

Figure 4.17a,b show that the FPS with high friction exhibits much minor bearing plate displacements in comparison with the FPS+VD, both semi-active versions, and the FPS with low friction. The FPS+VD and FPS with low friction show more displacement. FPS+SD with phase control and energy-predictive-based control have similar behavior and present minor displacement than the FPS+VD. From Figure 4.17c,d, it can be observed that the FPS+VD presents more capacity to control the drift than the single FPS and similarly, the semi-active versions show better performance than the FPS+VD. Finally, the phase-controlled FPS+SD always behaves slightly better than the energy-predictive-based one.

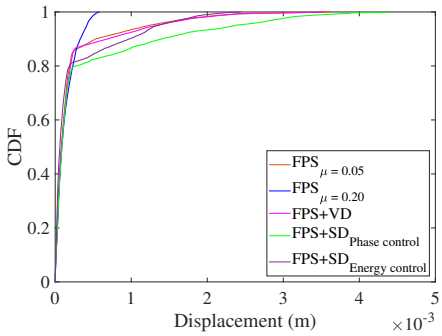

(a) CDF of the bearing displacements

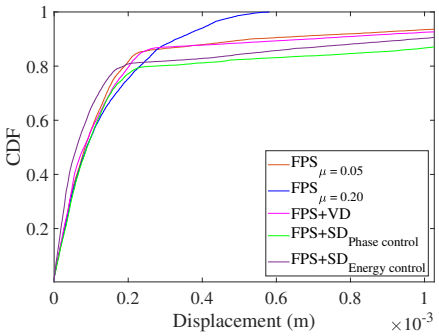

(b) Zoom CDF of the bearing displacements

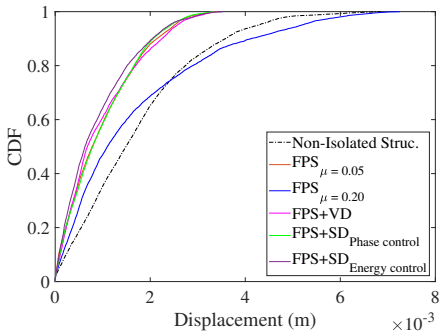

(c) CDF of the drift response of the structure

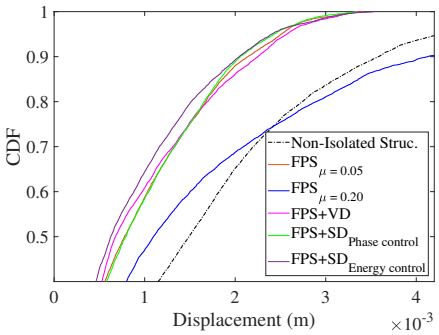

(d) Zoom to CDF of the drift response of the structure

Figure 4.18: CDF of bearing plate displacement and drift under the serviceability earthquake.

Figure 4.18 shows the same plots as those of Figure 4.17 but for the serviceability earthquake. Now, it is clearly appreciated that all the low-friction FPSs show similar performance in terms of the drift. The high friction FPS is unable to filter out low-intensity earthquakes.

4.5.4 Performance under several earthquakes

The isolator configurations studied in the previous section (Table 4.2) are now numerically tested under eight selected earthquakes. As an example, the input ground acceleration, the structure acceleration, the bearing plate displacement and the inter-story drift responses for one of the earthquakes, the Northridge earthquake (17 January 1999, magnitude of 6.7 Mw) are plotted in Figure 4.19. All configurations are effectively working for the range of maximum ground acceleration. When the earthquake intensity is reduced, the high-friction-coefficient FPS tends to behave as the non-isolated structure, that is, it is unable to filter out the input ground motion. Moreover, it can be observed that both semi-active strategies perform in a similar way. Indeed, the CDFs for the bearing plate displacement and the inter-story drift are computed in Figure 4.20. Similar conclusions as for Figure 4.19 can be stated from this figure.

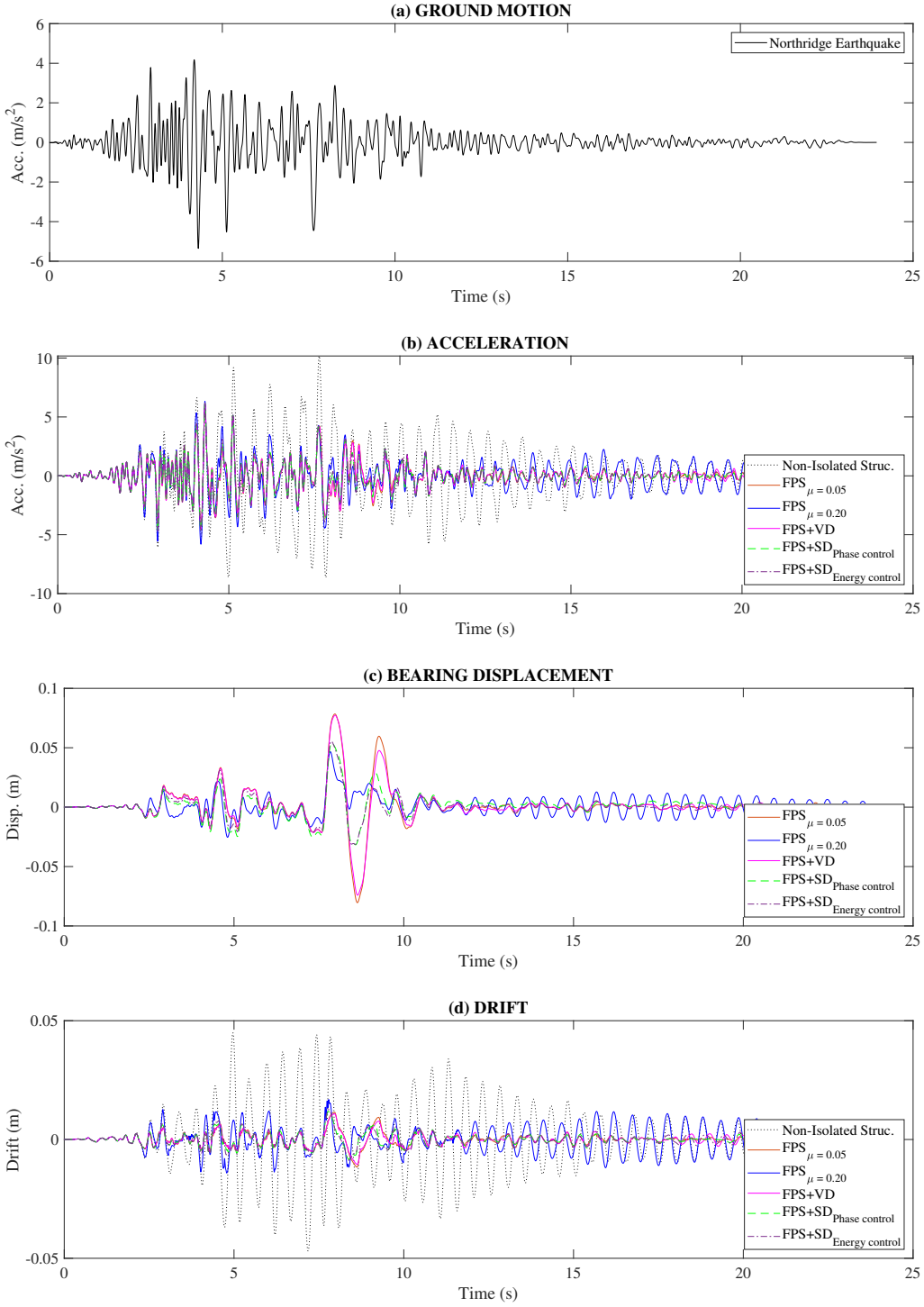

Figure 4.19: Time history to Northridge earthquake for the five isolator configurations studied.

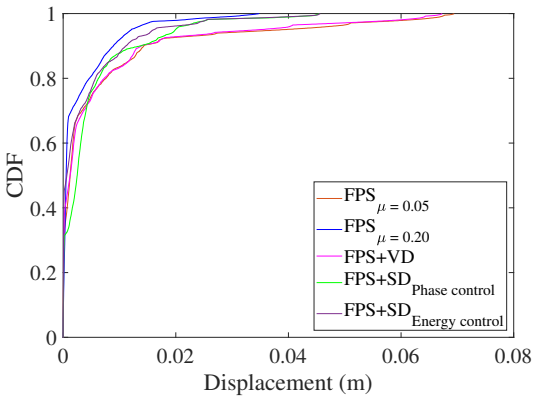

(a) CDF curves of the bearing displacements

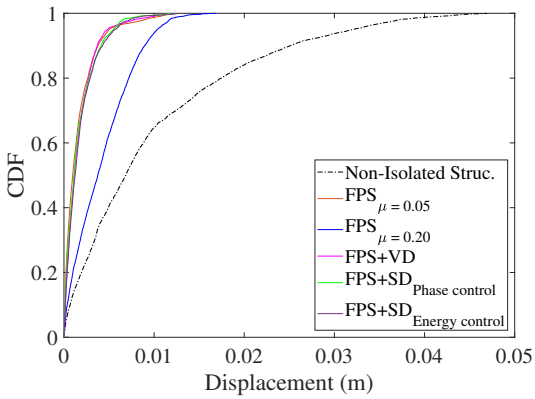

(b) CDF curves of the inter-story drift

Figure 4.20: CDF curves under the Northridge earthquake.

Table 4.4: Response under selected earthquakes.

Earthquake	**System**	$J_{1,P}$	$J_{1,RMS}$	$J_{2,P}$	$J_{2,RMS}$	$J_{3,P}$	$J_{3,RMS}$	$J_{4,S}$	$J_{4,T}$	ϕ_2
	Non-isolated	1.000	1.000	-	-	1.000	1.000	1.000	1.000	0.833
	$FPS_{\mu=0.05}$	0.760	0.554	0.071	0.013	0.492	0.544	0.408	0.318	0.486
Livermore	FPS+VD	0.776	0.580	0.056	0.009	0.495	0.566	0.395	0.336	0.495
5.8 Mw	$FPS+SD_{Phase}$	0.648	0.433	0.078	0.018	0.482	0.455	0.369	0.233	0.434
USA	$FPS+SD_{Energy}$	0.655	0.547	0.050	0.008	0.482	0.532	0.345	0.297	0.458
	$FPS_{\mu=0.20}$	1.133	1.072	0.010	0.003	1.059	1.068	1.287	1.190	0.900
	Non-isolated	1.000	1.000	-	-	1.000	1.000	1.000	1.000	0.833
	$FPS_{\mu=0.05}$	0.864	0.763	0.069	0.019	0.441	0.486	0.418	0.310	0.511
Imp. Valley	FPS+VD	0.868	0.760	0.052	0.017	0.432	0.479	0.390	0.298	0.504
6.5 Mw	$FPS+SD_{Phase}$	0.897	0.761	0.069	0.023	0.460	0.453	0.426	0.285	0.517
USA	$FPS+SD_{Energy}$	0.855	0.773	0.065	0.016	0.487	0.515	0.415	0.330	0.530
	$FPS_{\mu=0.20}$	0.953	1.288	0.110	0.011	1.656	1.484	2.459	2.255	1.191
	Non-isolated	1.000	1.000	-	-	1.000	1.000	1.000	1.000	0.833
	$FPS_{\mu=0.05}$	0.352	0.177	0.793	0.114	0.140	0.123	0.166	0.049	0.288
Corinth	FPS+VD	0.346	0.176	0.766	0.113	0.132	0.123	0.160	0.046	0.279
6.6 Mw	$FPS+SD_{Phase}$	0.345	0.178	0.820	0.114	0.148	0.127	0.158	0.046	0.294
GREECE	$FPS+SD_{Energy}$	0.303	0.185	0.618	0.087	0.157	0.140	0.113	0.044	0.260
	$FPS_{\mu=0.20}$	0.332	0.267	0.597	0.067	0.258	0.248	0.124	0.077	0.327
	Non-isolated	1.000	1.000	-	-	1.000	1.000	1.000	1.000	0.833
Northridge	$FPS_{\mu=0.05}$	0.597	0.407	1.156	0.239	0.248	0.181	0.766	0.202	0.473
6.69 Mw	FPS+VD	0.596	0.405	1.126	0.227	0.231	0.176	0.684	0.180	0.461
USA	$FPS+SD_{Phase}$	0.588	0.392	0.863	0.152	0.245	0.176	0.340	0.116	0.418
	$FPS+SD_{Energy}$	0.602	0.408	0.759	0.133	0.268	0.185	0.294	0.115	0.415
	$FPS_{\mu=0.20}$	0.607	0.514	0.581	0.098	0.357	0.370	0.274	0.180	0.464
	Non-isolated	1.000	1.000	-	-	1.000	1.000	1.000	1.000	0.833

Continued on the next page

Table 4.4: Response under selected earthquakes.

Earthquake	System	$J_{1,P}$	$J_{1,RMS}$	$J_{2,P}$	$J_{2,RMS}$	$J_{3,P}$	$J_{3,RMS}$	$J_{4,S}$	$J_{4,T}$	ϕ_2
	$FPS_{\mu=0.05}$	0.338	0.221	0.827	0.190	0.125	0.126	0.234	0.065	0.294
El Centro	FPS+VD	0.333	0.221	0.803	0.190	0.117	0.125	0.230	0.062	0.286
6.9 Mw	$FPS+SD_{Phase}$	0.344	0.220	0.824	0.175	0.129	0.132	0.197	0.057	0.296
USA	$FPS+SD_{Energy}$	0.312	0.227	0.617	0.143	0.145	0.147	0.155	0.057	0.266
	$FPS_{\mu=0.20}$	0.392	0.279	0.465	0.090	0.218	0.240	0.116	0.073	0.302
	Non-isolated	1.000	1.000	-	-	1.000	1.000	1.000	1.000	0.833
	$FPS_{\mu=0.05}$	0.231	0.204	0.239	0.049	0.161	0.189	0.131	0.054	0.198
Irpinia	FPS+VD	0.243	0.213	0.251	0.049	0.159	0.199	0.132	0.057	0.204
6.9 Mw	$FPS+SD_{Phase}$	0.242	0.218	0.241	0.047	0.163	0.205	0.124	0.057	0.205
ITALY	$FPS+SD_{Energy}$	0.261	0.230	0.206	0.038	0.182	0.219	0.107	0.059	0.213
	$FPS_{\mu=0.20}$	0.510	0.511	0.200	0.030	0.455	0.502	0.315	0.268	0.439
	Non-isolated	1.000	1.000	-	-	1.000	1.000	1.000	1.000	0.833
	$FPS_{\mu=0.05}$	0.523	0.360	0.279	0.056	0.164	0.239	0.289	0.0974	0.288
Iwate	FPS+VD	0.522	0.362	0.286	0.057	0.161	0.240	0.301	0.098	0.289
6.9 Mw	$FPS+SD_{Phase}$	0.554	0.373	0.294	0.056	0.183	0.255	0.292	0.105	0.307
JAPAN	$FPS+SD_{Energy}$	0.577	0.383	0.239	0.043	0.199	0.276	0.223	0.105	0.312
	$FPS_{\mu=0.20}$	0.735	0.561	0.218	0.026	0.438	0.516	0.345	0.281	0.484
	Non-isolated	1.000	1.000	-	-	1.000	1.000	1.000	1.000	0.833
	$FPS_{\mu=0.05}$	0.488	0.227	0.438	0.047	0.080	0.084	0.043	0.018	0.233
Darfield	FPS+VD	0.484	0.229	0.411	0.047	0.076	0.087	0.044	0.019	0.227
7.0 Mw	$FPS+SD_{Phase}$	0.491	0.233	0.421	0.047	0.088	0.090	0.043	0.019	0.235
NEW	$FPS+SD_{Energy}$	0.512	0.237	0.324	0.037	0.109	0.095	0.035	0.019	0.231
ZEALAND	$FPS_{\mu=0.20}$	0.579	0.303	0.312	0.027	0.186	0.201	0.062	0.051	0.295

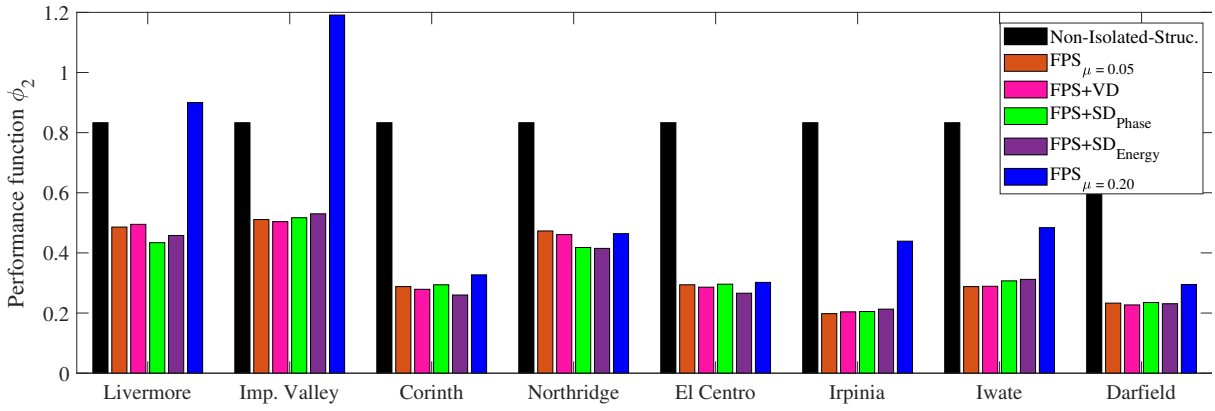

Figure 4.21: Performance function ϕ_2 of the configurations studied for the eight earthquakes.

Table 4.4 shows the PIs achieved for the eight selected earthquakes. They are located in the USA (North American plate), Japan (Pacific plate), New Zealand (Indo-Australian

plate), and finally Italy and Greece (Eurasian plate) [117]. An important point to highlight is that the influence of the TH record and the frequency content in earthquakes, with similar intensity, may change drastically the system response. As an example, if one compares Corinth and Imperial Valley events, the last one is shorter, with broader frequency content, lower PGA, and high RMS value than the first one. The results of this table are summarized in terms of the performance function ϕ_2 in Figure 4.25.

4.5.5 Performance discussion

The performance of the different configurations is further studied hereof. Firstly, the performance for a range of concave plate radii is studied. Secondly, the performance for the same concave plate is analyzed, and finally, the robustness of the isolator configurations under variation of the friction coefficient μ is studied.

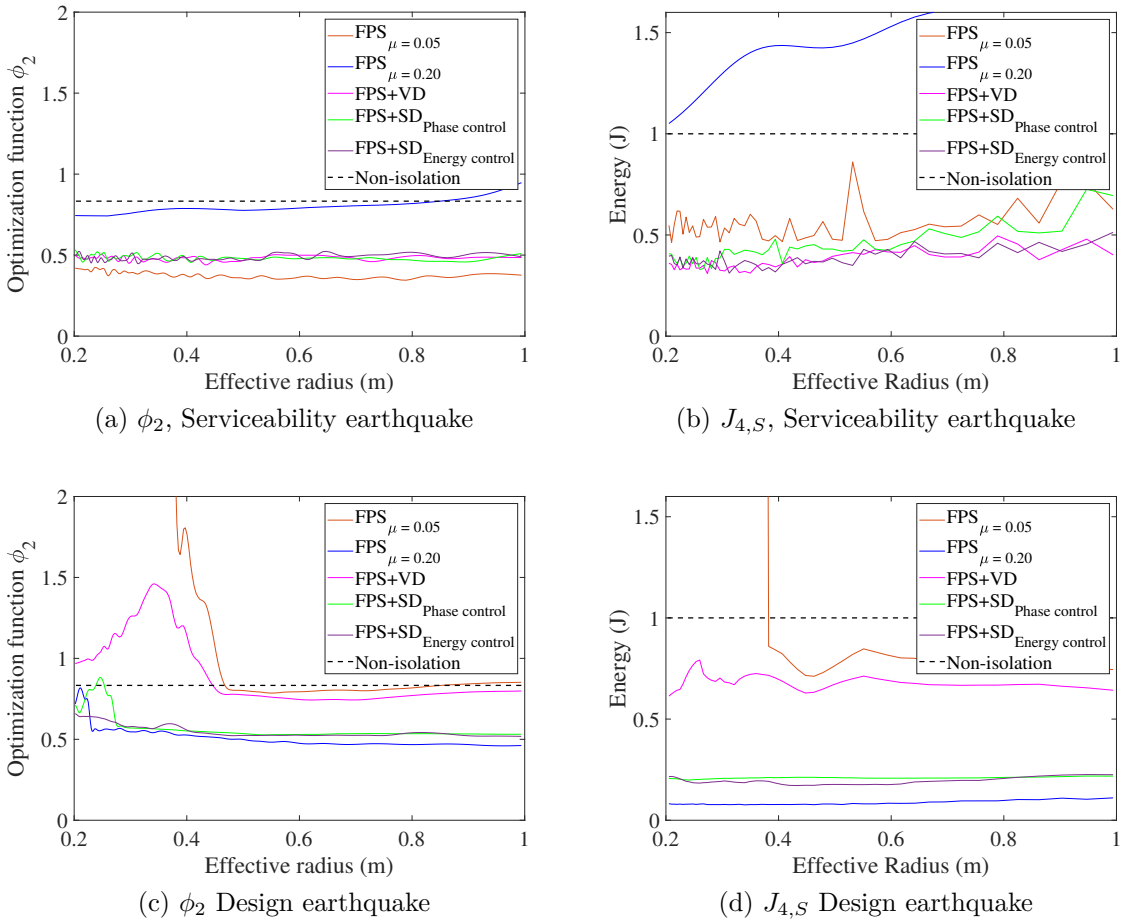

(a) ϕ_2, Serviceability earthquake

(b) $J_{4,S}$, Serviceability earthquake

(c) ϕ_2 Design earthquake

(d) $J_{4,S}$ Design earthquake

Figure 4.22: Performance function ϕ_2 and structure energy for a range of effective FPS radii.

Figure 4.22 shows the performance function ϕ_2 and the normalized structure mechani-

cal energy $J_{4,S}$ for the serviceability earthquake and for the design earthquake, considering a range of concave plate radii (in consonance with the minimum and maximum value of the pendulum natural frequency f_a). It can be concluded that the semi-active damper of the FPS acts when needed, avoiding stroke saturation under large ground motions, and showing low friction performance under low ground motions. From Figure 4.22a,b, it can be observed that the high-friction FPS cannot cope with low ground motions. From Figure 4.22c,d, it can be observed that small plate sizes for the semi-active versions can also be really effective. Additionally, for the low-friction single FPS and the FPS+VD, for small plate sizes, the performance is even worse than the one of the non-isolated structure.

Table 4.5 summarizes the optimization function values and the improvement obtained for each isolation system with the same concave plate size (R_{eff}) under the serviceability and design earthquake. The semi-active isolators are effective for both earthquakes while the FPS+VD and the low-friction FPS are only effective for the serviceability earthquake and the high-friction FPS only works for the design earthquake.

Table 4.5: Summary of the results for the same effective radius size.

Serviceability Earthquake						
System	$\boldsymbol{R_{eff}}$	$\boldsymbol{f_a}$	$\boldsymbol{\mu}$	$\boldsymbol{\zeta_{(c_a,c_{min})}}$	$\boldsymbol{\phi_2}$	**Reduction (%)**
$FPS_{\mu=0.05}$	0.300	0.867	0.05	-	0.491	50.90
FPS+VD	0.300	0.867	0.05	0.500	0.504	49.60
FPS+SD (Phase control)	0.300	0.867	0.05	0.480	0.480	52.00
FPS+SD (Energy control)	0.300	0.867	0.05	0.240	0.470	53.00
$FPS_{\mu=0.20}$	0.300	0.867	0.20	-	0.930	7.00
Design Earthquake						
System	$\boldsymbol{R_{eff}}$	$\boldsymbol{f_a}$	$\boldsymbol{\mu}$	$\boldsymbol{\zeta_{(c_a,c_{min})}}$	$\boldsymbol{\phi_2}$	**Reduction (%)**
$FPS_{\mu=0.05}$	0.300	0.867	0.05	-	5.614	0.00
FPS+VD	0.300	0.867	0.05	0.500	1.476	0.00
FPS+SD (Phase control)	0.300	0.867	0.05	0.480	0.608	39.20
FPS+SD (Energy control)	0.300	0.867	0.05	0.240	0.612	38.80
$FPS_{\mu=0.20}$	0.300	0.867	0.20	-	0.599	40.10

The performance function ϕ_2 for the configuration studied is plotted for the range of the friction coefficient μ used for the optimization problem (see Figure 4.23). Clearly, it is observed that the single FPS needs a low friction coefficient ($\leq$0.07) in order to cope with the serviceability earthquake. On the other way around, the FPS needs a high friction coefficient ($\geq$0.17) to be able to dissipate the energy demand of the design earthquake. The passive FPS and the semi-active ones are robust to changes in the friction coefficient, and the semi-active versions are working effectively for both earthquakes.

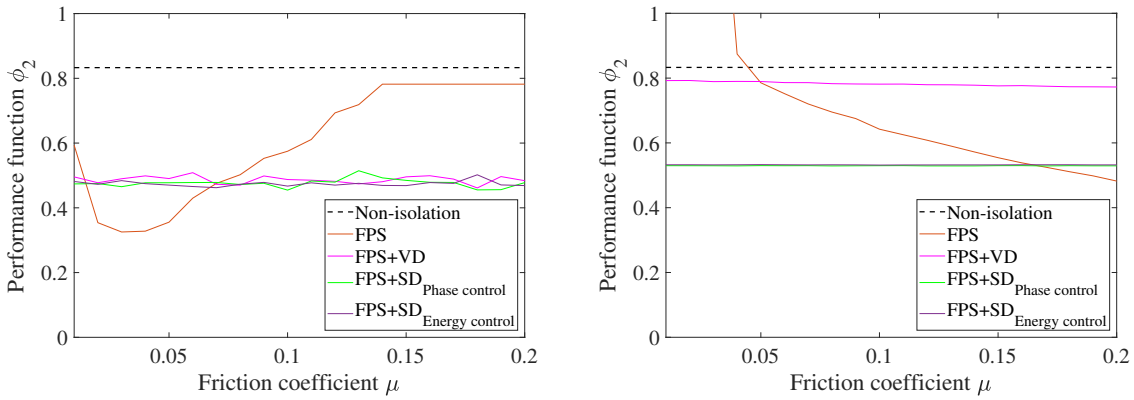

(a) ϕ_2 under serviceability earthquake (b) ϕ_2 under design earthquake

Figure 4.23: Performance function ϕ_2 and structure energy for a range of effective FPS radii.

4.6 Semi-active isolation system under realistic conditions

The first approximation of the SFPS for a single degree of freedom with an ideal semi-active control was carried out in the previous sections. This section updates the SDOF to a three-dimensional structure (see Figure 4.24).

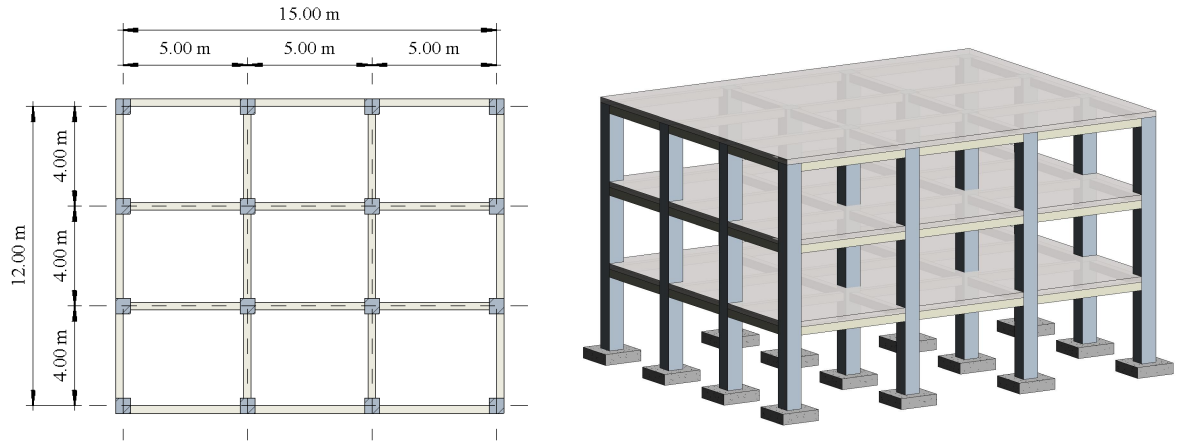

(a) floor top view (b) Isometric view

Figure 4.24: Three-dimensional benchmark structure.

The semi-active isolation system suffers the following modifications: i) The unidirectional behavior for the semi-active isolation system now considers the bidirectional behavior. ii) the control system introduces the realistic conditions studied in section

3.5, iii) the characteristic hysteretic behavior of the MR damper is included in the SFPS through a tangential model. Finally, the response of the benchmark structure with an SFPS is evaluated using a sensitivity analysis and real earthquake records for an ideal control, an On-Off control, and a continuous control.

4.6.1 Bidirectional benchmark structure and equivalent models

One spatial structure has 6 degrees of freedom by node, 3 of displacement, and 3 of rotation. At the same time, there are N number of nodes by M number of floors. Thus, a real structure could have (6xNxM) degrees of freedom. This type of structure can be transformed into an equivalent system through condensation methods static or dynamic, which can simplify the number of degrees of freedom of the structure, without loss the most relevant information about the real response of the structure. Figure 4.25 shows a squematic representation when a reduction on the degrees of freedom is applied.

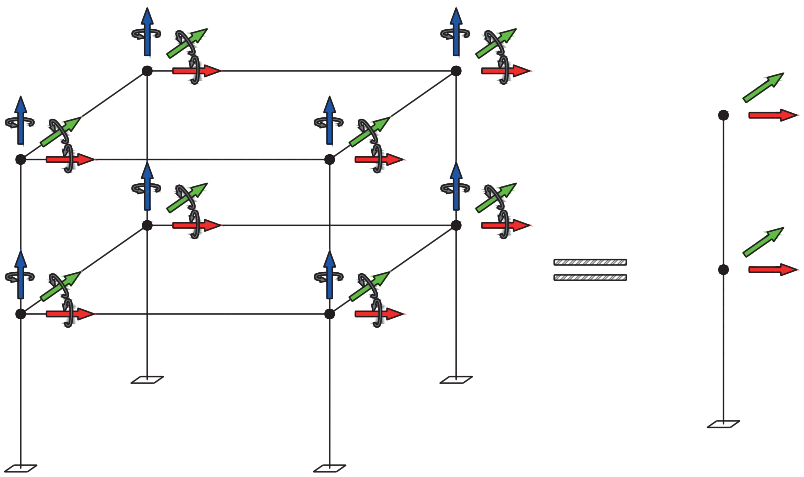

Figure 4.25: Schematic representation of a reduced-order model (ROM).

This method is called Reduced-Order Model (ROM), different approaches have been developed depend on the known and unknown variables, or how complex is the structure [119, 118]. The method proposed by Seto [120] lumps the modal parameters of a structure, and thus allows omit those high modes that for cases of the seismic engineer or the base isolation system have minor relevance. Besides, the use of these methods simplifies the system for application in the controllers-design that requires feedback of the response.

One approximation to obtain a ROM consist in solve the eigenvalue problem, which determinate the frequencies and vibration modes. The process proposed by Chopra in [119] is present here as follow:
The equation of motion for system with negligible damping system can be expressed as:

$$m\ddot{x} + kx = 0, \tag{4.31}$$

where m and k are the mass and stiffness, respectively. $\ddot{x}$ and x are the acceleration and displacement. The relationship with the modal domains is defined by $x = \phi q$. The modal vector ϕ is time-invariant, while q is the displacement variation described through a harmonic function in the modal domain.

If $\ddot{x} = \phi\ddot{q}$ and $\ddot{q} = -\omega^2 q$, the equation 4.31 in the modal domain is given by:

$$\left[-\omega^2 m\phi + k\phi\right] q = 0, \tag{4.32}$$

if $q = 0$ it mean that system does not have movement. Thus, the angular frequencies (ω) and modal shape ϕ must satisfy the following condition:

$$k = \phi^{-1}\omega^2 m\phi. \tag{4.33}$$

Equation 4.33 is called the eigenvalue equation, which allows obtaining the angular frequencies ω and modal shapes ϕ when m and k are known. Otherwise, if a lump mass matrix (m), modal shape (ϕ), and angular frequencies (ω) are known, the new matrix stiffness is obtained for the ROM system.

For N degrees of freedom the matrix eigenvalue equation is defined as follows:

$$K = \phi^{-1}\omega^2 M\phi, \tag{4.34}$$

where matrices ϕ, ω y M takes the following shape:

$$\phi_{i,j} = \begin{pmatrix} \phi_{1,1} & \phi_{1,2} & \cdots & \phi_{1,j} \\ \phi_{2,1} & \phi_{2,2} & \cdots & \phi_{2,j} \\ \vdots & \vdots & \ddots & \vdots \\ \phi_{i,1} & \phi_{i,2} & \cdots & \phi_{i,j} \end{pmatrix}, \omega = \begin{pmatrix} \omega_1 & 0 & \cdots & 0 \\ 0 & \omega_i & \cdots & 0 \\ \vdots & \vdots & \ddots & \vdots \\ 0 & 0 & \cdots & \omega_n \end{pmatrix}, M = \begin{pmatrix} m_1 & 0 & \cdots & 0 \\ 0 & m_i & \cdots & 0 \\ \vdots & \vdots & \ddots & \vdots \\ 0 & 0 & \cdots & m_n \end{pmatrix}.$$

The choice of the natural frequencies and modal shapes in equation 4.34 have to be coherent with the desired behavior to be reproduced through the ROM, and its values can be known from the mathematical model of the three-dimensional structure. If the torsional effects wish to be analyzed, an additional degree per floor must be considered, including the frequency for the torsional mode and its corresponding modal shape.

4.6.2 Semi-active bidirectional condition

In this section, the bidirectional behavior of the SFPS is now considered. Two semi-active dampers are required and implemented in each perpendicular direction of the SFPS, as shown in Figure 4.26.

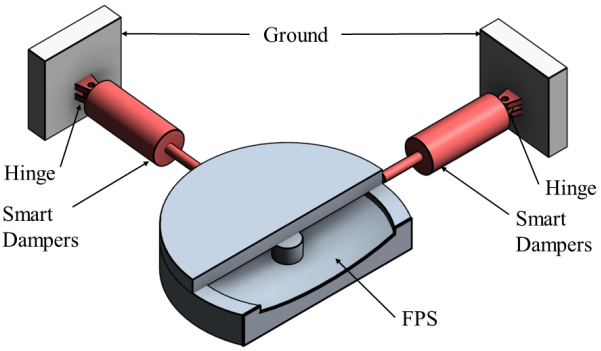

Figure 4.26: Isometric representation of a SFPS.

The equation of motion 4.19 defined in section 4.3 must be updated to consider the bidirectional effect on the friction forces and the semi-active damper. The equation of motion that evaluates the bidirectional behavior in the SFPS is given by:

$$m_a\ddot{x}_a + F_{x'_a x_a} + F_{x'_a y_a} + F_{fx}(sign(\dot{x}_a)) + k_a x_a - c_s(\dot{x}_s - \dot{x}_a) - k_s(x_s - x_a) = -m_a\ddot{x}_g, \quad (4.35)$$

$$m_a\ddot{y}_a + F_{y'_a y_a} + F_{y'_a x_a} + F_{fy}(sign(\dot{y}_a)) + k_a y_a - c_s(\dot{y}_s - \dot{y}_a) - k_s(y_s - y_a) = -m_a\ddot{y}_g, \quad (4.36)$$

The friction force F_{fx} and F_{fy} in sliding state is defined as follows:

$$F_{fx} = \mu W \frac{\dot{x}_a}{\sqrt{\dot{x}_a^2 + \dot{y}_a^2}}, \quad (4.37)$$

$$F_{fy} = \mu W \frac{\dot{y}_a}{\sqrt{\dot{x}_a^2 + \dot{y}_a^2}}, \quad (4.38)$$

The SFPS now consider its bidirectional behavior. Thus, two semi-active dampers are required in each perpendicular direction as show in Figure 4.26. The equation about the passive device has been defined in section 4.2.2.

The variables $F_{x'_a x_a}$, $F_{x'_a y_a}$, $F_{y'_a y_a}$, and $F_{y'_a x_a}$ are the components of forces performed by each damper once the upper plate is away from the origin. The angles θ_1 and θ_2 show in figure 4.27 are associated with the damper position and x_a and y_a global axes, respectively.

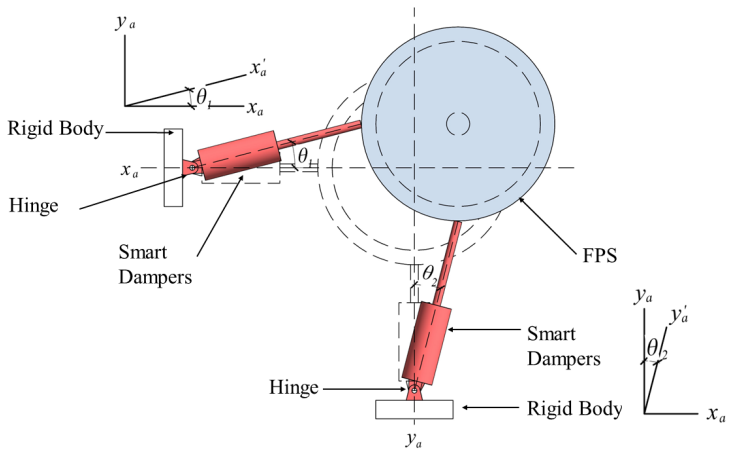

Figure 4.27: Global and local axes for SFPS outside the center position

The force components of each damper are defined as follows:

$$F_{x'_a x_a} = c_{semi}(t) \cdot \dot{x}'_a \cdot cos\theta_1; \quad F_{x'_a y_a} = c_{semi}(t) \cdot \dot{x}'_a \cdot sin\theta_1, \tag{4.39}$$

$$F_{y'_a y_a} = c_{semi}(t) \cdot \dot{y}'_a \cdot cos\theta_2; \quad F_{y'_a x_a} = c_{semi}(t) \cdot \dot{y}'_a \cdot sin\theta_2, \tag{4.40}$$

the variables $\dot{x}'_a$ and $\dot{y}'_a$ are the velocity of each piston acting in the local axes. This variables are introduce to obtain the component of force for the global axes.

4.6.3 Realistic control system

In order to turn the numerical model of the SFPS into a realistic model, the sponge RD-1097-1 Damper has been identified. The MR damper has been subjected to experimental tests with controlled voltage, frequency, and amplitude. The voltage changes from 0 to 2 V with increments every 0.25 V. The frequency starts at 1 Hz and ends at 7 Hz, switching every 1 Hz. The amplitude configured is ±3, 7, and 11 mm.

Experimental tests have allowed the identification of a Tangential model dependent on voltage and maximum velocity (v_m). The harmonic displacement reported in each experimental test was derived to obtain velocity and acceleration. The parameters identified for the MR damper were scaled to achieve a force of 2000 kN, one order of magnitude larger than the MR damper used by Spencer in [126]. The tangential model parameters are presented below:

$$\alpha = (14.478(V) + 1.233) \cdot (-0.002v_m^2 + 0.608v_m + 7024.92),$$

$$\delta = 0.5472(V) + 0.4354; \quad \beta = \frac{2.9106}{v_m^{0.8621}},$$

$$c_0 = 1.4962(V) + 0.9767; \quad k = 0.20; \quad f_0 = 0.01.$$

Figure 4.28 shows the block diagram representation for the numerical model of the SFPS. This block diagram includes the realistic conditions that will be present for implementing the control law defined in section 3.5 for the STMD.

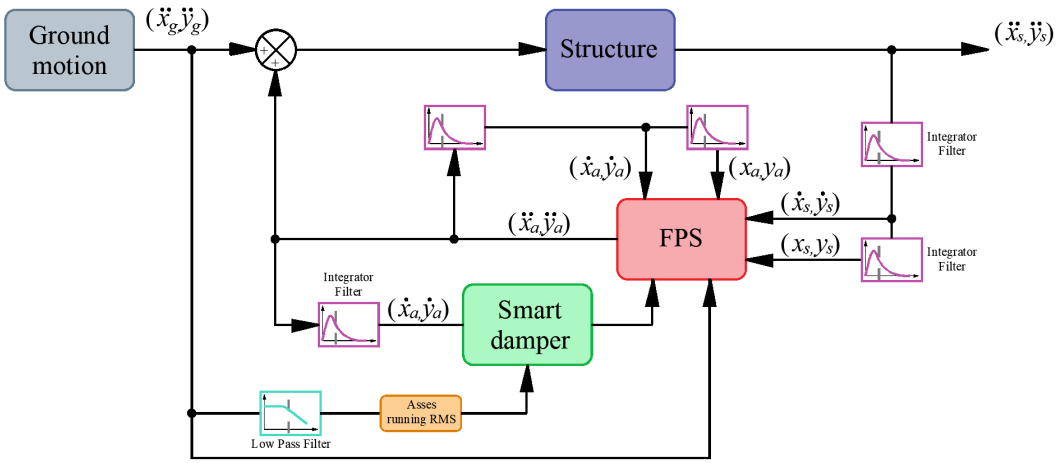

Figure 4.28: Block Diagram for realistic SFPS

The control system includes a low-pass Butterworth filter of fourth-order to remove the noise from the ground motion. It was defined with a cutoff frequency of 10 Hz. The Z-transform for this filter is given by:

$$H_{low}(z) = \frac{8.985\text{x}10^{-7}z^4 + 3.594x10^{-6}z^3 + 5.391x10^{-6}z^2 + 3.594x10^{-6}z + 8.985x10^{-7}}{z^4 - 3.836z^3 + 5.521z^2 - 3.534z + 0.8486}. \tag{4.41}$$

The Integrator filter to obtain velocity $\dot{x}_a$ of the FPS with a cutoff of one-twentieth times the first frequency of the benchmark structure is present through the Z-transform as follows:

$$H_{int}(z) = \frac{0.00099z - 0.00099}{z^2 - 1.999z + 0.999}. \tag{4.42}$$

Finally, the deactivation rule is considered with the 1-s-RMS instant acceleration values as defined in section 3.5.2.

4.6.4 Low-frequency earthquakes

In order to analyze the response of the SFPS under resonance effects, a second type of seismic excitation is considered. Earthquake motions provided by regions close to an active fault and grounds with a wave propagation velocity of 360 m/s are characterized by low-frequency content. Figure 4.29a shows the response spectrum obtained from the United States Geological Survey (USGS), exactly from their "Earthquake Hazard Program"by selecting a location near the Hayward Fault in California and a C/D site class [123]. This

response spectrum is compared against the MCE defined in section 4.5.1, and it is evident as the Low-frequency Earthquake (LFE) provide an acceleration (g) higher than the MCE for the same period.

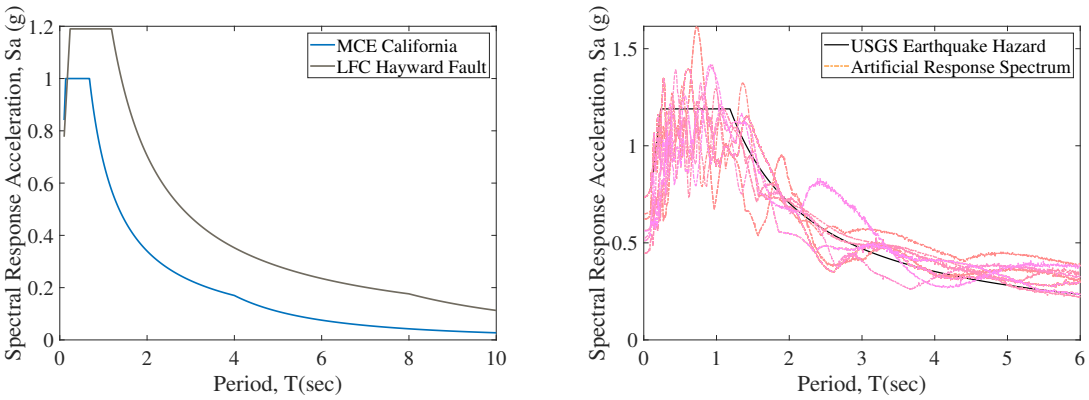

(a) Design response spectrum and response spectra

(b) FFT of the artificial earthquakes

Figure 4.29: Design response spectrum and Fast Fourier Transforms (FFT) of the input ground acceleration.

Similar to the design procedure carried out in section 4.5, a serie of 15 artificial earthquakes are defined based on the low-frequency response spectrum (see Figure 4.29b). This input force will be considers acting in each global direction of the superstructure, and although the input signal is the same in both directions, the response of the structure is not similar due to it has a different global stiffness value in each direction. Figure 4.30 shows the 15 artificial earthquakes that will be used to analyze the response of the isolation system under a resonance effect.

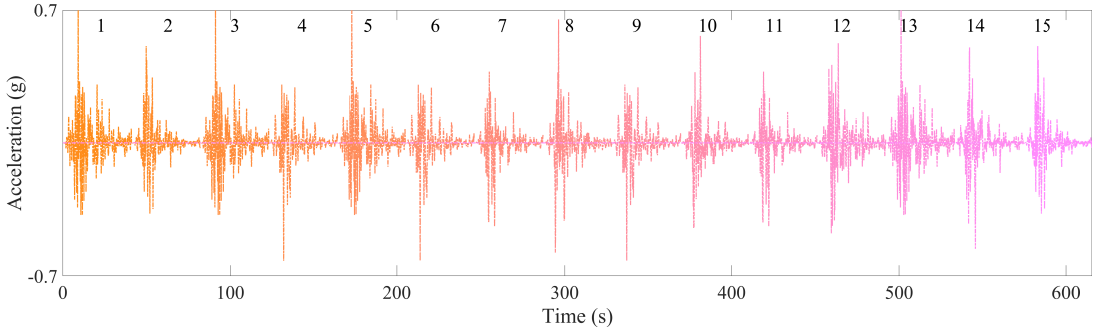

Figure 4.30: Input ground acceleration for LF earthquakes.

4.6.5 Bidirectional performance analysis

4.6.5.1 Bidirectional FPS

In this section, a sensitivity analysis is performed under the bidirectional effect of MCEs and LFEs. First, an FPS was analyzed, followed by the SFPS. The sensitivity analysis takes into account the frequency of the isolator (f_a) and the friction coefficient (μ) for the FPS, while for the SFPS, the friction coefficient is considered constant to analyze the dominant variable of the semi-active device considered. Figure 4.31 shows the response in terms of $J_{1,P}$ at each floor under both types of earthquake excitation.

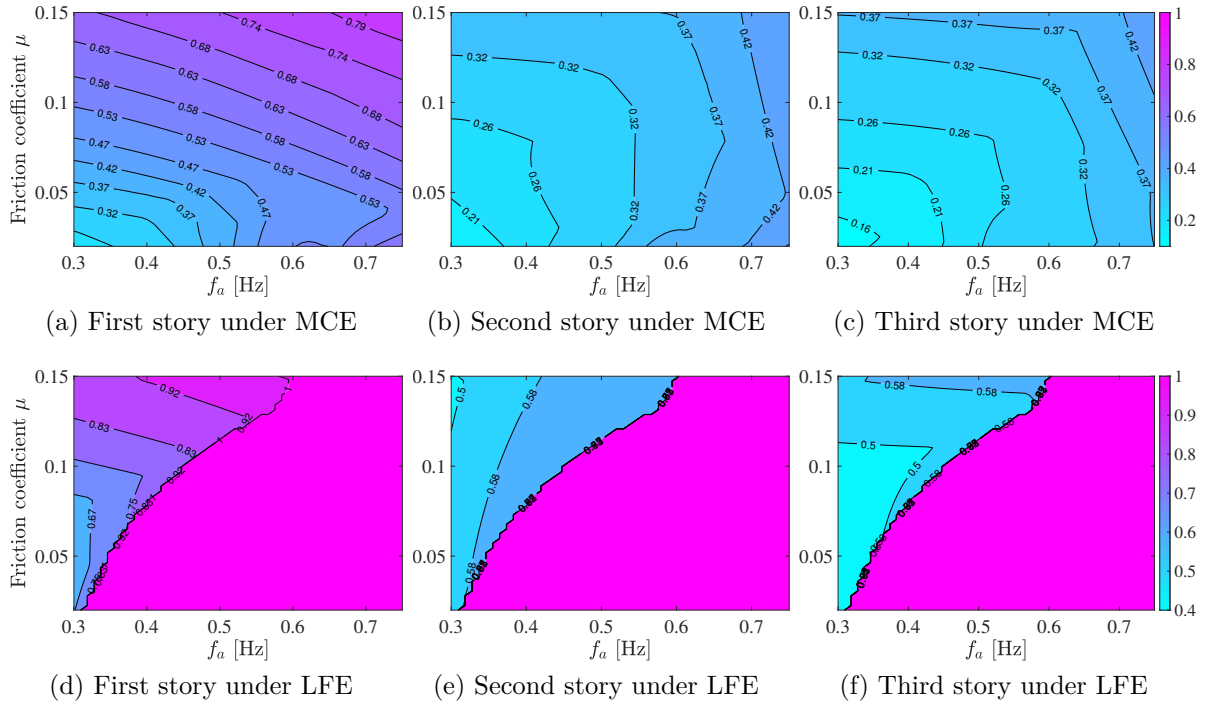

(a) First story under MCE (b) Second story under MCE (c) Third story under MCE

(d) First story under LFE (e) Second story under LFE (f) Third story under LFE

Figure 4.31: Sensitivity analysis. $J_{1,P}$ for bidirectional FPS.

The optimal parameters for the FPS under MCE are obtained for the minimum friction coefficient and frequency. Figures 4.31a to 4.31c present the sensitivity analysis under MCE, and it is possible to see how the same pattern is repeated for all three stories. In this case, the low friction tends to develop sudden increase of peak acceleration for f_a values greater than 0.3Hz. Figures 4.31d to 4.31f show that the isolation effect is obtained for values of friction coefficient greater than 3%, where the isolation system may adopt higher frequency values at the same time that the friction coefficient must be adopted.

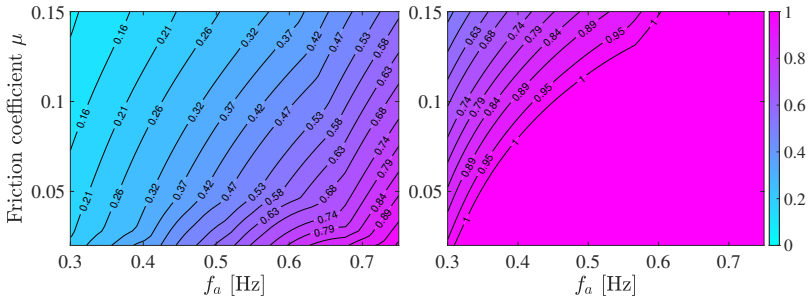

(a) Bearing displacements under MCE

(b) Bearing displacements under LFE

Figure 4.32: Sensitivity analysis. $J_{2,P}$ for bidirectional FPS.

Figure 4.32 show the response of J_2 under MCE and LFE, respectively. The optimum response for both ground motions is obtained for high friction. Low friction could work for the MCE cases, while for LFE, the bearing displacement reaches the geometry edge, producing impact with the restraining ring. In Figure 4.32a, the FPS does not reach the geometry edge if any frequency is analyzed for the pendulum. Thus, an FPS designed under an MCE criterion choosing a pendulum frequency greater than 0.3Hz posed a risk of performing instability under the LFE criterion as Figure 4.32b demostrated.

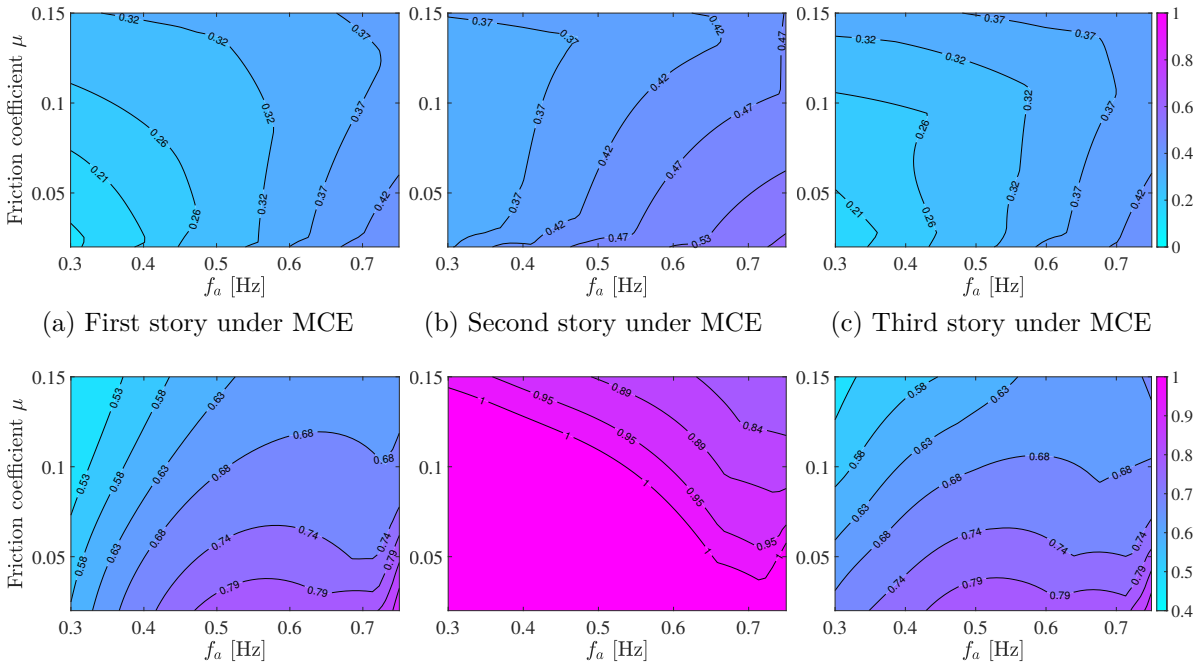

(a) First story under MCE

(b) Second story under MCE

(c) Third story under MCE

(d) First story under LFE

(e) Second story under LFE

(f) Third story under LFE

Figure 4.33: Sensitivity analysis. $J_{3,P}$ for bidirectional FPS.

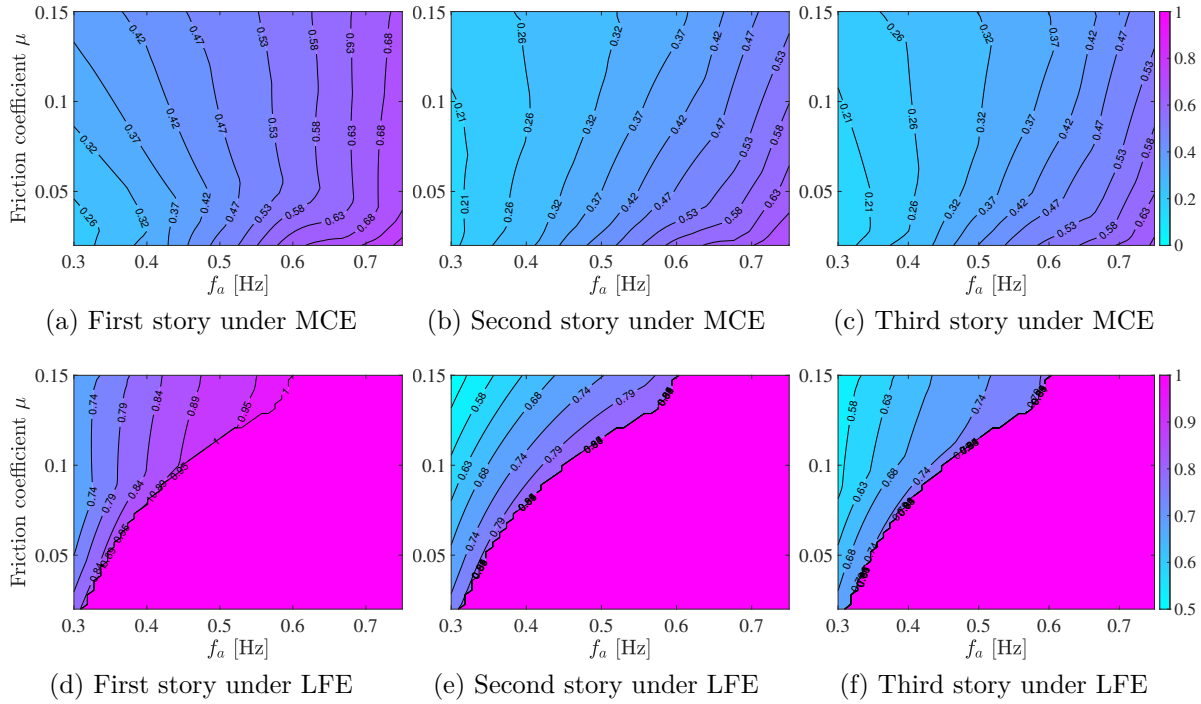

(a) First story under MCE (b) Second story under MCE (c) Third story under MCE

(d) First story under LFE (e) Second story under LFE (f) Third story under LFE

Figure 4.34: Optimization function ϕ_1 for bidirectional FPS.

Figure 4.33 shows the response of $J_{3,P}$ under MCE and LFE. The same pattern given in $J_{1,P}$ and $J_{2,P}$ is shown here. The second story of the structure with FPS experiences lateral displacement greater than the non-isolated structure.

The first performance function is presented in Figure 4.34, where the combination of the performance indices $J_{1,P}$ and $J_{2,P}$ are considered based on the equation 4.25.

The minimum performance index under MCE is obtained by selecting the minimum friction and frequency in the pendulum. Besides, for other frequencies, the FPS can dissipate energy. The performance function ϕ_1 for the LFE shows the same pattern expressed in figures 4.31 and 4.32, where the plate-to-ring impact, produced by the resonance effect, jeopardizes the system and requires an overdemand capacity for the structure or end in a collapse situation if the FPS does not have restraining ring (see figure 4.4a).

4.6.5.2 Bidirectional SFPS

Based on the previous results for the FPS, a friction coefficient of 10% is used in the FPS, and three configurations for the semi-active control in the SFPS are considered: i) an ideal semi-active device with an On-Off control, ii) a realistic semi-active device with an On-Off control, and iii) a realistic semi-active device with a continuous $G(t)$ control.

A factor gain (f_g) is included within the minimum damping c_{min} and limited to the factor gain considered for the maximum damping c_{max} in the first configuration. This f_g is evaluated through the sensitivity analysis to determine the optimum c_{min}. At the same

time, for the realistic semi-active device, the variable to be analyzed is the voltage (V) on the MR damper. The damping coefficients are defined as follows:

$$c_{max} = 1000 \cdot 2m_a(2\pi \cdot f_s)^2 \cdot \zeta, \tag{4.43}$$

$$c_{min} = f_g \cdot 2m_a \cdot (2\pi \cdot f_s)^2 \cdot \zeta, \tag{4.44}$$

$$\text{with} \quad \zeta = 2\% \quad \text{and} \quad 0 \leq f_g \leq 1000.$$

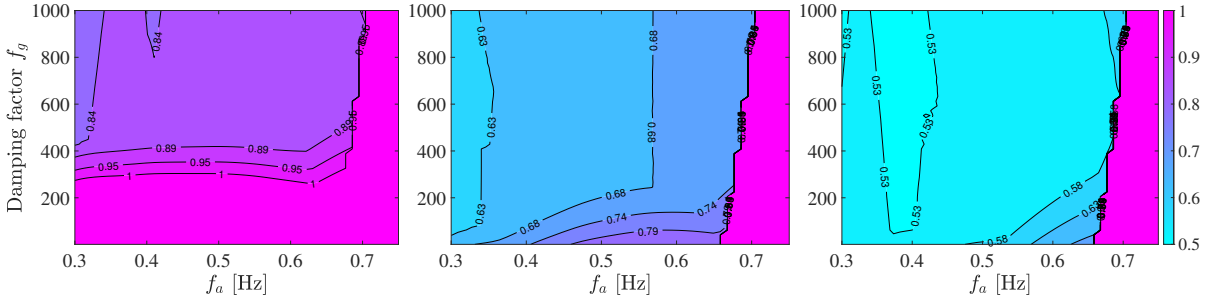

(a) First story under LFE (b) Second story under LFE (c) Third story under LFE

Figure 4.35: Sensitivity analysis. $J_{1,P}$ for bidirectional SFPS with ideal phase control.

From figures 4.31 to 4.34, it is possible to notice that the FPS loses effectiveness under LFE due to the resonant effect, which produces large bearing displacement with associated impact. From Figure 4.35, it can be observed that, with a minimum damping factor of 350 at least, the SFPS with an ideal phase control has a robust behavior, including for a minor size compared with the passive version. From Figure 4.36, the smart damper provides the best performance for all stories. The additional damping in the system affects in two ways the response of the structure with the passive device. First, controlling the lateral displacement of the second story, and second, improving the response of the first and third story with low minimum damping (c_{min}), and allowing to choose a smaller plate size.

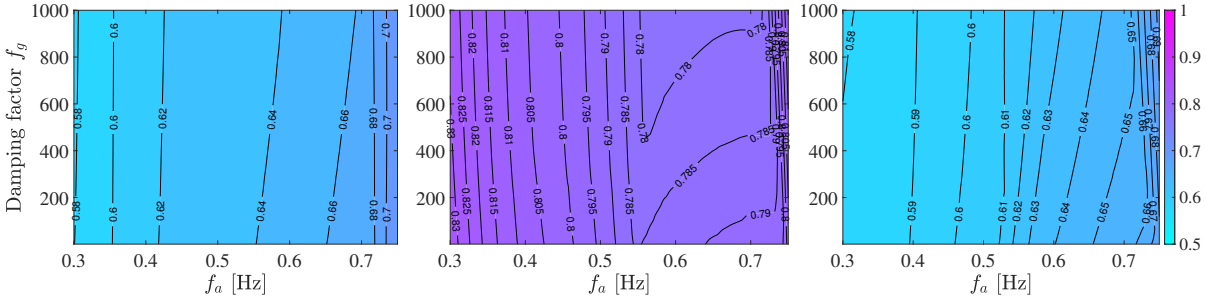

(a) $J_{3,P}$ First story under LFC (b) $J_{3,P}$ Second story under LFC (c) $J_{3,P}$ Third story under LFC

Figure 4.36: Sensitivity analysis. $J_{3,P}$ for SFPS with ideal phase control under LF earthquakes

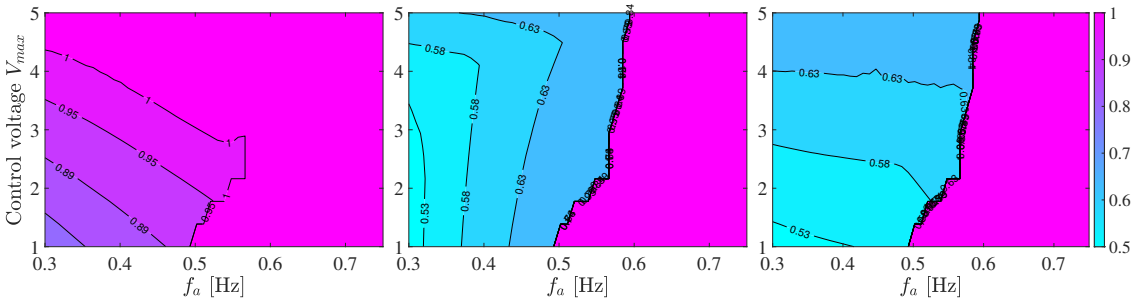

(a) First story under LFE (b) Second story under LFE (c) Third story under LFE

Figure 4.37: Sensitivity analysis. $J_{1,P}$ for bidirectional SFPS with On-Off control.

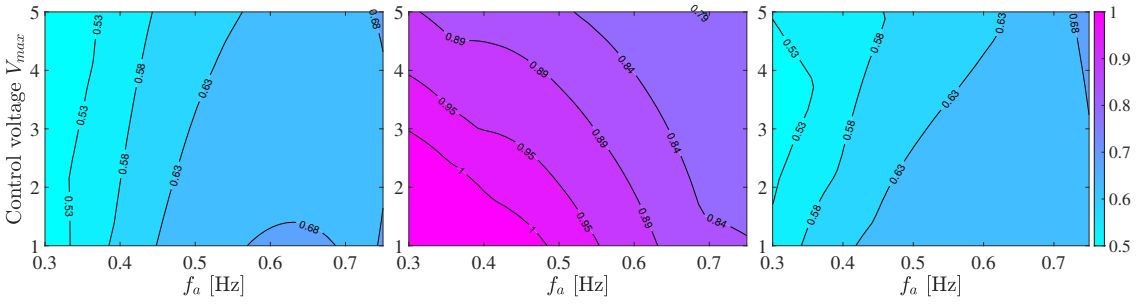

(a) First story under LFE (b) Second story under LFE (c) Third story under LFE

Figure 4.38: Sensitivity analysis. $J_{3,P}$ for bidirectional SFPS with On-Off control.

Figure 4.37 and 4.38 show that the sensitivity analysis for the SFPS with an On-Off control law improves the response of the FPS to LFE for $J_{1,P}$ and $J_{3,P}$, respectively. This improvement is not as effective as the ideal system but is better than the passive FPS. For the first story, the use of maximum voltage can suddenly block the top plate sliding process, interrupting the requested dissipation process. For the other stories, the behavior is robust and would allow the use of minimum size for the FPS.

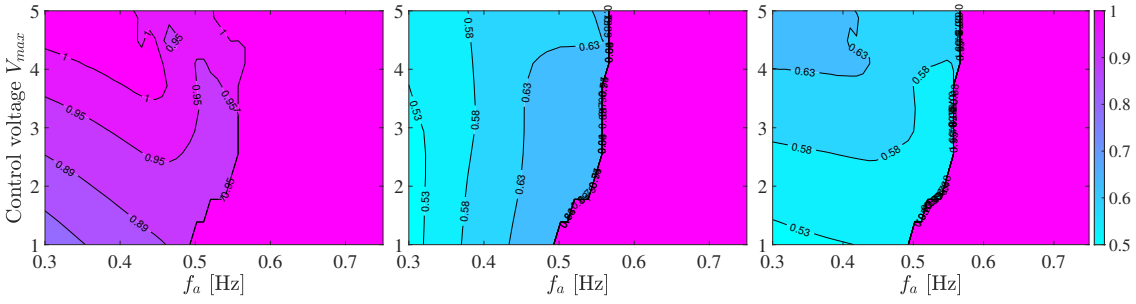

(a) First story under LFE (b) Second story under LFE (c) Third story under LFE

Figure 4.39: Sensitivity analysis. $J_{1,P}$ for bidirectional SFPS with variable control G(t).

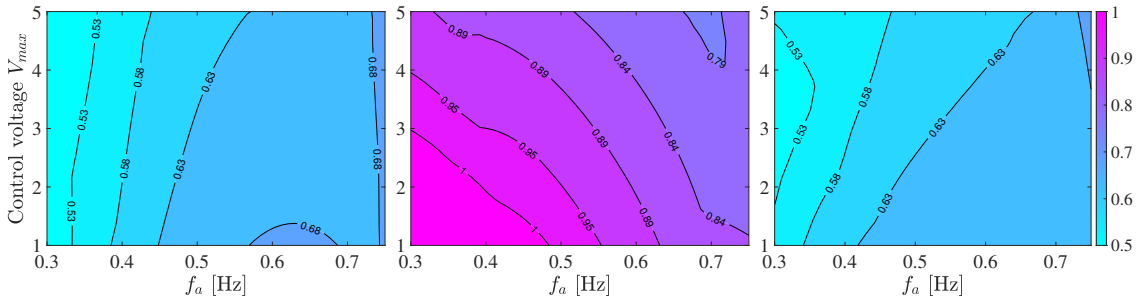

(a) First story under LFE (b) Second story under LFE (c) Third story under LFE

Figure 4.40: Sensitivity analysis. $J_{3,P}$ for bidirectional SFPS with variable control G(t).

Figures 4.39 and 4.40 show the response of the SFPS with a variable control law G(t) applied, where the system develops a better response with respect to the On-Off control law, transforming the sudden blocking effect generated by the application of the maximum voltage by a controllable management of the voltage and, consequently, of the damping force.

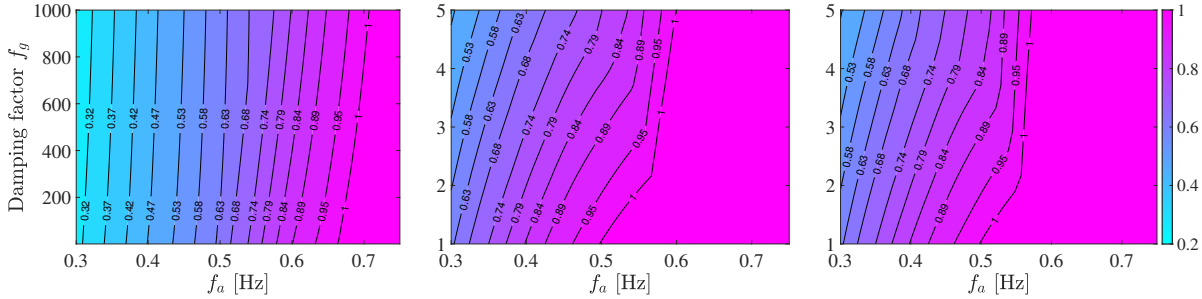

(a) SFPS with Ideal control (b) SFPS with On-Off control (c) SFPS with G(t) control

Figure 4.41: Sensitivity analysis. $J_{2,P}$ for bidirectional SFPS under LFE.

From Figures 4.37 to 4.40, it is worth mentioning that the contour plots obtained from On-Off and G(t) control are quite similar. The use of an MR damper improves the passive FPS performance depending on the pendulum size, which could be smaller without losing effectiveness in the energy dissipation process under LFE.

The effects of the MR dampers in the passive FPS can be appreciated in the contour plot for the second story, where, if a maximum voltage equal to 1 V is applied, the MR damper does not provide sufficient force to control the bearings displacement. As the V_{max} increases, the excessive lateral displacement experienced by the structure is reduced concerning the FPS performance.

The optimum performance of the SFPS under resonance effects is obtained for a lower frequency value f_a. However, this condition requires a considerable size for the FPS. Based

on this assumption, Figure 4.41 shows the contour plots for the bearing displacements of the SFPS. For a frequency of 0.55 Hz, the SFPS achieved the smaller size before the geometry was susceptible to collision with the ring or collapse if the ring is not present. Table 4.6 summarizes the performance functions ϕ_1 and ϕ_2 for each configuration.

Table 4.6: Optimum parameters for isolators configuration under LFE.

System	f_a	μ	f_g	V	**Story 1**		**Story 2**		**Story 3**	
					ϕ_1	ϕ_2	ϕ_1	ϕ_2	ϕ_1	ϕ_2
FPS	0.45	10%	-	-	8.99	17.50	7.03	12.81	5.98	11.09
$SFPS_{Ideal}$	0.45	10%	612.63	-	0.78	0.72	0.69	0.70	0.63	0.62
$SFPS_{On-Off}$	0.45	10%	-	5 V	0.92	0.82	0.76	0.77	0.76	0.70
$SFPS_{G(t)}$	0.45	10%	-	5 V	0.97	0.82	0.78	0.78	0.77	0.70

From table 4.6, it can be seen that SFPS behaves better than FPS, which cannot reduce the performance functions as it occurs under MCE design earthquake, developing a significant increase due to the resonant effect on the isolation device. SFPS maintains the performance function under the unity, ensuring that no additional dissipation capacity of the superstructure is required.

4.6.6 Performance under real earthquake records

The optimum configurations for the FPS and SFPS are now numerically tested under nine selected earthquakes scaled to fit the low-frequency response spectrum. The table 4.7 summarizes the performance indexes for each system studied.

Table 4.7: Response under selected earthquakes.

Earthq.	System	Index Performance														
		Bearing		Story 1				Story 2				Story 3				
		J_{2p}	$J_2 rms$	J_{1p}	J_{1rms}	J_{3p}	J_{3rms}	J_{1p}	J_{1rms}	J_{3p}	J_{3rms}	J_{1p}	J_{1rms}	J_{3p}	J_{3rms}	$J_{4,S}$
	FPS	1.46	0.44	1.43	0.84	0.70	0.29	0.59	0.50	1.06	0.98	0.63	0.53	0.64	0.67	3.31
El Alamo	$SFPS_{Ideal}$	0.52	0.15	0.66	0.60	0.44	0.39	0.46	0.40	0.53	0.53	0.43	0.36	0.41	0.39	0.59
6.8 Mw	$SFPS_{On-Off}$	1.14	0.32	1.12	1.21	0.55	0.57	0.57	0.53	0.87	0.92	0.56	0.48	0.57	0.57	2.07
Mex.	$SFPS_{G(t)}$	1.26	0.36	1.23	1.23	0.60	0.60	0.58	0.55	0.92	1.00	0.60	0.49	0.58	0.60	2.19
	FPS	1.57	0.37	1.44	0.75	0.71	0.25	0.53	0.42	1.13	0.87	0.57	0.46	0.71	0.57	2.66
Borrego	$SFPS_{Ideal}$	0.92	0.14	0.66	0.56	0.43	0.37	0.44	0.37	0.75	0.52	0.41	0.34	0.48	0.36	0.58
6.8 Mw	$SFPS_{On-Off}$	1.44	0.25	1.37	1.11	0.66	0.51	0.53	0.50	1.08	0.81	0.59	0.49	0.70	0.52	1.56
USA	$SFPS_{G(t)}$	1.44	0.28	1.39	1.15	0.66	0.53	0.52	0.50	1.09	0.86	0.59	0.49	0.70	0.53	1.65
Imperial	FPS	1.17	0.36	1.72	1.10	0.72	0.37	0.52	0.63	1.08	1.27	0.63	0.67	0.70	0.86	5.55
Valley	$SFPS_{Ideal}$	0.74	0.13	0.69	0.77	0.45	0.54	0.44	0.54	0.71	0.74	0.48	0.49	0.46	0.53	1.14
Mw 6.53	$SFPS_{On-Off}$	0.93	0.22	1.60	1.51	0.53	0.68	0.57	0.67	0.81	1.06	0.77	0.68	0.58	0.69	2.67
USA	$SFPS_{G(t)}$	0.98	0.26	1.44	1.51	0.57	0.73	0.59	0.69	0.88	1.20	0.70	0.68	0.60	0.75	2.94

Continues on next page

Table 4.7: Response under selected earthquakes.

Earthq.	System	Index Performance														
		Bearing		Story 1				Story 2				Story 3				
		J_{2p}	$J_2 rms$	J_{1p}	J_{1rms}	J_{3p}	J_{3rms}	J_{1p}	J_{1rms}	J_{3p}	J_{3rms}	J_{1p}	J_{1rms}	J_{3p}	J_{3rms}	$J_{4,S}$
Kern	FPS	1.11	0.41	1.05	0.78	0.55	0.27	0.44	0.45	0.78	0.93	0.52	0.48	0.50	0.62	3.02
County	$SFPS_{Ideal}$	0.53	0.14	0.41	0.59	0.30	0.37	0.33	0.38	0.42	0.51	0.31	0.35	0.30	0.36	0.56
Mw 7.36	$SFPS_{On-Off}$	0.90	0.26	0.90	1.16	0.45	0.52	0.45	0.51	0.70	0.82	0.43	0.48	0.47	0.52	1.64
USA	$SFPS_{G(t)}$	1.00	0.31	0.85	1.18	0.47	0.56	0.45	0.53	0.77	0.93	0.42	0.48	0.50	0.56	1.79
	FPS	1.43	0.46	1.25	0.75	0.52	0.26	0.54	0.45	0.90	0.88	0.52	0.48	0.56	0.60	2.73
Landers	$SFPS_{Ideal}$	0.55	0.17	0.60	0.60	0.39	0.40	0.41	0.40	0.49	0.53	0.36	0.36	0.37	0.39	0.60
Mw 7.28	$SFPS_{On-Off}$	1.11	0.28	1.01	1.12	0.47	0.48	0.49	0.48	0.74	0.73	0.50	0.49	0.49	0.48	1.27
USA	$SFPS_{G(t)}$	1.06	0.33	1.09	1.11	0.45	0.51	0.44	0.49	0.71	0.82	0.42	0.48	0.46	0.51	1.38
Northern	FPS	1.28	0.46	1.42	0.67	0.50	0.26	0.45	0.45	0.76	0.89	0.35	0.46	0.46	0.61	2.70
California	$SFPS_{Ideal}$	0.69	0.17	0.80	0.57	0.40	0.36	0.42	0.36	0.53	0.50	0.37	0.32	0.37	0.35	0.47
Mw 6.5	$SFPS_{On-Off}$	1.08	0.28	1.06	0.94	0.42	0.45	0.44	0.45	0.66	0.71	0.39	0.41	0.40	0.45	1.15
USA	$SFPS_{G(t)}$	1.11	0.33	1.15	0.98	0.46	0.49	0.51	0.47	0.68	0.80	0.40	0.43	0.42	0.50	1.27
	FPS	1.24	0.42	1.29	0.78	0.53	0.29	0.42	0.49	0.83	0.99	0.40	0.51	0.51	0.67	3.18
Parkfield	$SFPS_{Ideal}$	0.71	0.16	0.61	0.65	0.47	0.43	0.44	0.43	0.67	0.59	0.40	0.38	0.48	0.42	0.66
Mw 6.19	$SFPS_{On-Off}$	1.02	0.26	1.09	1.08	0.47	0.52	0.43	0.49	0.78	0.81	0.48	0.48	0.51	0.52	1.46
USA	$SFPS_{G(t)}$	1.05	0.30	1.02	1.16	0.48	0.56	0.44	0.52	0.80	0.91	0.47	0.49	0.52	0.57	1.60
Superst.	FPS	1.44	0.43	1.37	0.95	0.75	0.37	0.65	0.64	1.17	1.28	0.70	0.65	0.73	0.87	5.80
Hill	$SFPS_{Ideal}$	0.65	0.14	0.89	0.71	0.47	0.47	0.52	0.47	0.61	0.65	0.69	0.42	0.51	0.46	0.94
Mw 6.54	$SFPS_{On-Off}$	1.14	0.28	1.18	1.15	0.62	0.66	0.63	0.63	1.03	1.09	0.70	0.60	0.70	0.68	2.99
USA	$SFPS_{G(t)}$	1.20	0.32	1.23	1.23	0.63	0.71	0.60	0.65	1.05	1.20	0.67	0.60	0.69	0.73	3.19
	FPS	1.61	0.55	1.60	1.18	1.04	0.50	1.03	0.89	1.76	1.71	0.91	0.89	1.07	1.17	11.26
Smart 1	$SFPS_{Ideal}$	0.60	0.17	0.87	0.82	0.65	0.59	0.74	0.59	0.82	0.81	0.66	0.53	0.60	0.58	1.41
Mw 7.3	$SFPS_{On-Off}$	1.18	0.35	1.41	1.38	0.87	0.85	0.85	0.85	1.44	1.42	0.74	0.79	0.90	0.88	5.17
Taiwan	$SFPS_{G(t)}$	1.27	0.41	1.52	1.53	0.90	0.94	0.92	0.90	1.47	1.60	0.84	0.82	0.95	0.97	5.64

The SFPS configuration develops lower bearing displacement than the FPS. For the ideal SFPS, the bearing displacement never reaches the geometrical limit of the plate. The SFPS with On-Off control and variable G(t) control, which include the nonlinear behavior of the MR damper, develops lower bearing displacements than FPS without achieving the ideal behavior desired. All SFPS have achieved a reduction in the performance index of story 1 with respect to the FPS and similar values for stories 2 and 3. In terms of energy balance ($J_{4,S}$), the SFPS dissipates more energy on the isolation device, producing a reduction in the energy developed by the structure, which is reported in the last column from Table 4.7. The improvement achieved for the SFPS is around 82% for the ideal control, 49% for the On-Off control, and 45% for the variable G(t) control.

Figures 4.42 to 4.44 show the performance function in each story for the different configurations of isolation studied. For story 1 (Figure 4.42), all of the SFPS perform a better behavior than the FPS. In contrast, for stories 2 and 3, their behavior is more similar for the On-Off control and the variable G(t) control. The ideal control is better than the latter two, which is consistent with the results presented in Table 4.7.

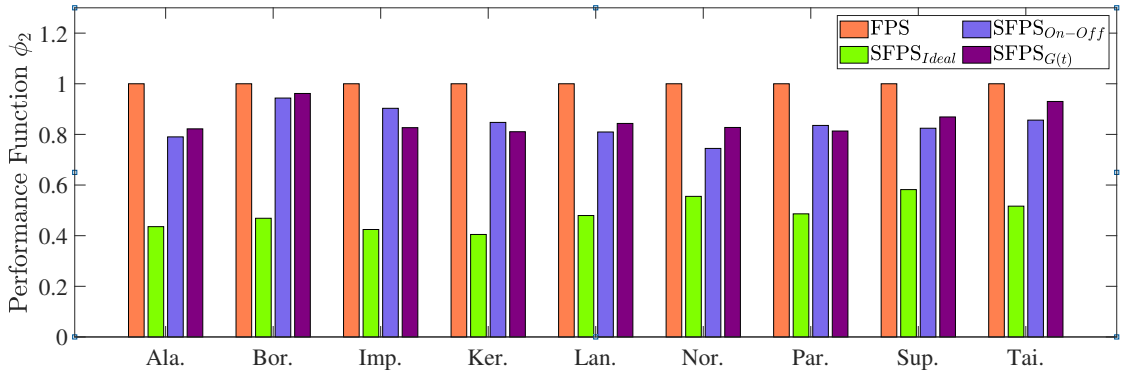

Figure 4.42: Performance function ϕ_2 of the configurations studied in story 1 for the nine earthquakes.

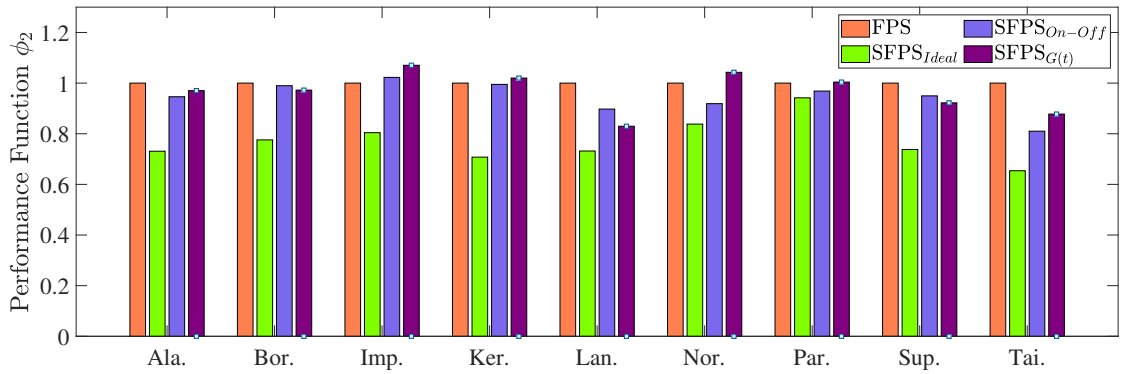

Figure 4.43: Performance function ϕ_2 of the configurations studied in story 2 for the nine earthquakes.

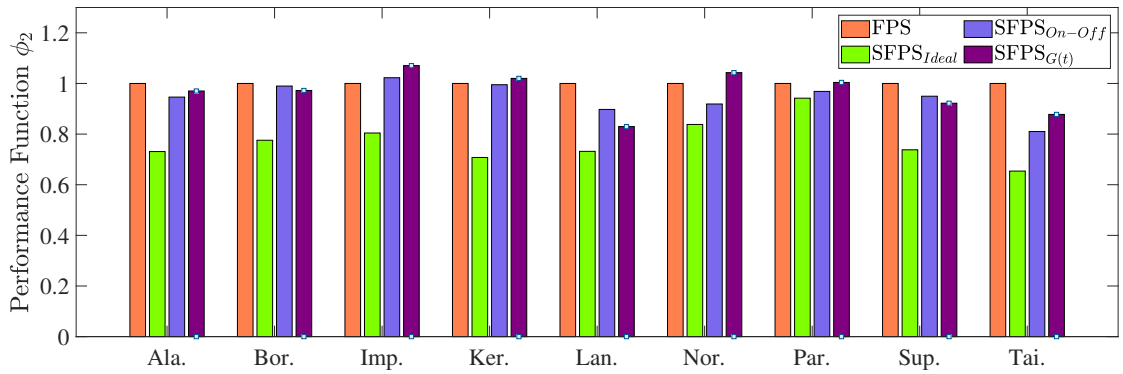

Figure 4.44: Performance function ϕ_2 of the configurations studied in story 3 for the nine earthquakes.

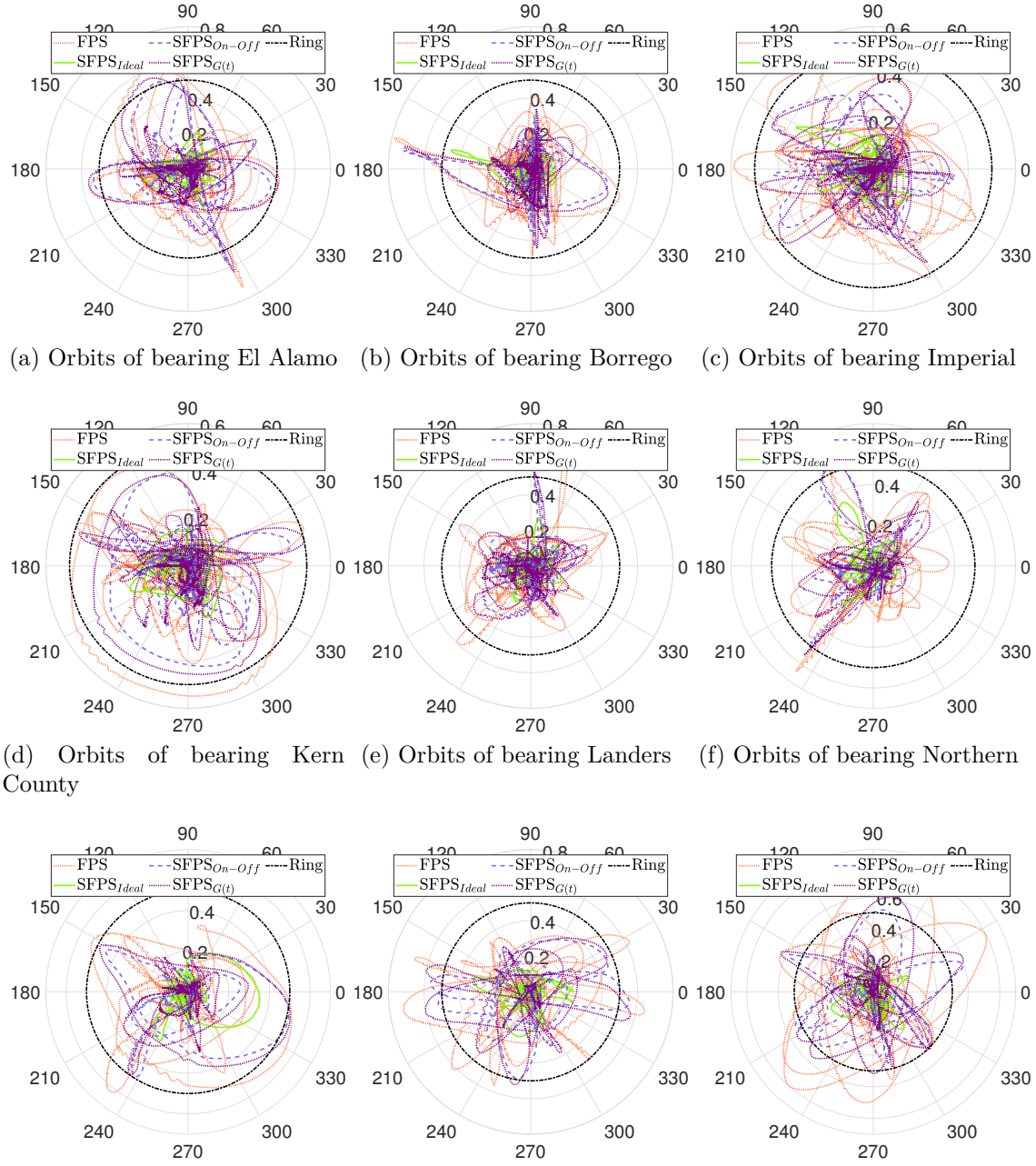

(a) Orbits of bearing El Alamo (b) Orbits of bearing Borrego (c) Orbits of bearing Imperial

(d) Orbits of bearing Kern County (e) Orbits of bearing Landers (f) Orbits of bearing Northern

(g) Orbits of bearing Parkfield (h) Orbits of bearing Superstition (i) Orbits of bearing Taiwan

Figure 4.45: Orbits of bearings under real earthquake records

Figure 4.45 shows the orbit plot of the different isolation configurations studied for each earthquake. In these plots, it is possible to observe a large amount of bearing displacement concentrated inside the concave plate for the semi-active version. However, when the resonance effect is too extreme, the semi-active versions with On-Off control and variable G(t) control cannot avoid experiencing large displacements, following the behavior developed by the passive version.

Chapter 5

Conclusions and future works

In this thesis, the design methodology of a phase control law has been studied and proposed to control the response of semi-active devices such as MR dampers to improve the behavior of passive devices and alleviate the detuning or saturation problems. MR dampers added to TMDs and FPSs are explored to consider the phase control in inertial and isolation systems, respectively. Several MR damper have been experimentally tested to carry out an identification process, allowing the numerical study of this type of device in both situations.

For both systems, the phase control law governs the response of the MR damper based on acceleration and velocity signal, which can be obtained through two accelerometers, one in the structure and the other in the passive device. For this reason, its implementation is quite simple, and the following conclusions can be drawn from each system considered:

Phase Control in the Inertial Systems

An STMD with phase control law in a lightweight FRP footbridge has been proposed to control the dynamic response. The first approach consisted of a numerical study of the optimum design of the STMD, where the design process was based on the solution of a multiobjective constrained minimization problem in which the parameters that define the control device are the design variables of the problem. The constraint has been adopted from the maximum vertical acceleration allowed by guidelines.

The methodology framework included the human-structure-actuator interaction for the first time, and 50 samples of the structure and the equivalent human system were generated to consider uncertainties of the coupled human-structure system. The same case was used to compare the STMD with the passive TMD. The optimum design of the STMD achieved a reduction of more than 50% with respect to the uncontrolled case; under detuned situations caused by uncertainties in the human-structure interaction system, the TMD needs a 26% higher mass to achieve a similar reduction capacity.

In order to consider a realistic scenary, the optimization process for a realistic simu-

lation of the STMD has been undertaken, using an MR damper (modeled by a Bingham model) as a semi-active device and including the required elements that must be taken into account for the feedback process and the implementation of the control law. The results reported a performance reduction compared with the TMD and the ideal STMD. However, the realistic STMD requires less mass than the STMD, and concerning the ideal STMD, the nonlinearities of the MR damper have been considered into the problem. Although an On-Off phase control has been adopted here, the proposed design methodology can be applied for other control strategies as long as the phase adjustment procedure corresponds to the one explained in Section 3.3.

Finally, the experimental test of the STMD with phase control law was performed on the FRP footbridge designed and constructed at the Laboratory of Structures of the Technical University of Madrid. The effectiveness of the STMD was compared with the TMD considering an On-Off control, a continuous gain control and a variable gain control.

The detuned effects between the FRP footbridge and the control device were taken into account in two situations: “detuned below”and “detuned above”with respect to the tuned situation. To achieve these effects, additional 20 kg have been placed on the FRP footbridge to consider a group of pedestrians acting as static dead load and include an additional support to consider the situation where the natural behavior of the roller support has changed, which reproduces each detuned situation respectively.

The final conclusion is that the performance of semi-active devices is better than that of the passive version in detuned situations, reducing the vibration level under the limits defined by the guidelines.

Phase Control in Base Isolation Systems

The use of SFPS with phase control law has been studied. First, an FPS is designed with a damper, which can be passive or semi-active. Therefore, two types of isolation systems have been considered and studied: (i) an FPS together with a passive damper and (ii) an FPS with a smart damper. For the second situation an On-Off control has been implemented. In order to evaluate the effectiveness and simplicity of the phase control law, a second control law based on a full-state feedback control was taken into account.

The design methodology proposed is based on a two-step design process that takes into account low and high intensity earthquakes. Each step is based on a function that weights different performance indexes in terms of their maximum and RMS values. More specifically, the following observations can be drawn:

- The FPS with low friction exhibits large bearing displacements under the design earthquake, while FPS with high friction will not activate under the serviceability earthquake. This effect is related to undesirable residual displacements when the design earthquake ends and experiences low intensity.
- The implementation of an FPS with additional damper allows us to use a concave

plate with low friction, increasing thus the re-centering capacity and avoiding the residual displacements.

- The FPS with a semi-active damper controls the bearing plate displacement acting when needed, avoiding the plate-to-ring impact of the collapse of the system under large ground motions for low friction FPS and allowing a better re-centering capacity. Additionally, for a similar performance as compared to a single FPS or the FPS with passive damper, the plate size for the SFPS may be significantly smaller.

- The single FPS performance fully depends on the friction coefficient value; however, the FPS equipped with a damper is robust to changes of the friction coefficient, showing better performance when the damper is semi-active.

- The SFPS has similar behavior with a phase control and a full-state feedback control. However, the implementation of phase control in practice become easier as compared to energy control. The phase control requires to measure the response in acceleration and this is possible using directly an accelerometer placed in the concave plate. The full-state feedback control requires measuring the velocity and displacement of the structure and, this process could take a longer time for multi-story buildings. Additionally, an accurate model is needed to get this law to be effective.

Finally, the SFPS is updated to consider realistic conditions in a numerical model, such as i) bidirectional behavior in the isolation system, ii) an identified model of a Sponge MR damper, and iii) the uncertainties associated with realistic conditions for the application of the phase control law.

The performance of the SFPS with a phase control law, with an On-Off control and a variable gain control, against the performance of the FPS under a series of low-frequency earthquakes was evaluated to consider the resonant effects on the isolation device. The FPS develops a large bearing displacement even for friction coefficient values of 10%, which requires a larger concave plate size with respect to the design earthquakes. Otherwise, there will be instability due to plate-to-ring impact. The FPS presents a robust behavior to this type of earthquake, avoiding the plate-to-ring effect with a smaller plate size. In addition, the energy dissipation is better, reducing at least 45% of the mechanical energy demand developed by the structure for the SFPS considering the nonlinearities of the MR damper and 80% of the ideal SFPS.

Future work will focus on strategies to reduce the influence of MR damper nonlinearities by exploring dynamic inversion control laws. Additionally, the extension of phase control to other passive control devices such as supplemental rotational inertia for seismic protection of structures may be studied [131].

Bibliography

1. Biswas, W. K. Carbon Footprint of Embodied Energy Consumpiton Assessment of Building Construction Works in Western Australia. *International Journal of Sustainable Built Environment,* **2014**, *3*, 179-186.

2. Fenner, A. E., Kibert, C. J., Woo, J., Morque, Shirley. The Carbon Footprint of Buildings: A Review of Methodologies and Applications. *Renewable and Sustainable Energy Reviews,* **2018**, *94*, 1142-1152.

3. Rahman, A. Fancy, S. F., Bobby, S. A. Analysis of Drift due to Wind Loads and Earthquake Loads on Tall Structures by Programming Language C. *International Journal of Scientific & Research,* **2012**, *3*, Issue 6.

4. Bonkowski, P. A., Zembaty, Z., Minch M. Y. Seismic Effects on Leaning Slender Structure an Tall Buildings. *Engineering Structures,* **2019**, *198*, 109518.

5. Repetto, M. P., Solari, G. Wind-Induced Fatigue Collapse of Real Slender Structures. *Engineering Structures,* **2010**, *32*, 3888-3898.

6. Jones, C. A., Reynolds, P., Pavic, A. Vibration Serviceability of Stadia Structures Subjected to Dynamic Crowd Loads: A Literature Review. *Journal of Sound and Vibration,* **2011**, *330*, 1531-1566.

7. Ingólfsson, E. T., Georgakis, C. T., Jönsson, J. Pedestrian-Induced Lateral Vibrations of Footbridges: A Literature Review. *Engineering Structures,* **2012**, *45*, 21-52.

8. ISE. Dynamic Performance Requirements for Permanent Grandstands Subject to Crowd Action: Recommendations for Management, Design and Assessment. *London, UK: Institution of Structural Engineers,* **2008**, *330*, 1531-1566.

9. Kelly J. M. Aseismic Base Isolation: Review and Bibliography. *Soil Dynamics and Earthquake Engineering,* **1986**, *5*, No 3.

10. Buckle, I. G., EERI, M., Mayes, R. L. Kelly J. M. Seismic Isolation: History, Application, and Performance - A World View. *Earthquake Spectra,* **1990**, *6*, No 2.

11. Warn G. P., Ryan, K. L. A Review of Seismic Isolation for Buildings: Historical Development and Research Needs. *Buildings,* **2012**, *2*, 300-325.

12. Tsai, C. S. Seismic Isolation Devices: History and Recent Developments. Proceedings of the ASME 2015 Pressure Vessels and Piping Conference. *PVP2015 Boston Massachusetts,* **2015**, *2* 45068.

13. Lopez Garcia, D., Soong T. T. Slinding Fragility of Block-Type Non-Structural Components. Part 1: Unrestrained Components. *Earthquake Engng Struct Dyn,* **2003**, *32* 111-129.

14. Nepal, S. Saitoh, M. Improving the Performance of Conventional Base Isolation Systems by an External Variable Negative Stiffness Device Under Near-Fault and Long-Period Ground Motions. *Earthq Eng & Eng Vib,* **2020**, *19* 985-1003.

15. Mayes, R. L., Naeim, F. The Seismic Design - "Chapter 14 Design of Structures with Seismic Isolation". *Springer Science + Bussness Media, LLC* **2001**, *Second Edition.*

16. Aguiar, R.; Vergara, F.; Monge, J.P. Análisis Sísmico de una Estructura con Aisladores FPS de Primera y Segunda Generación y Elastoméricos Con Núcleo De Plomo. *Rev. Int. Ing. Estructuras* **2014**, *19*, 35-89.

17. Jangid, R.S. Optimum Friction Pendulum System for Near-Fault Motions. *Engineering Structures,* **2005**, *27*, 349-359.

18. Ramallo, J. C., Johnson, E. A., Spencer, B. F., Sain, M. K. Semiactive Building Base Isolation. *Proceedings of the American Control Conference* **1999**, *San Diego, California.*

19. Mohebbi, M., Dadkhah, H. Effective Semiactive Base Isolation System under Multiple Earthquakes. *Advances in Civil Engineering* **2018**, *ID 7382481,* 12.

20. Zhu, Y. P., Lang, Z. Q., Kawanishi, Y., Kohiyama, M. Semi-actively Implemented Non-linear Damping for Building Isolation Under Seismic Loadings. *Front. Built Environ,* **2020**, *6,* Art. 19.

21. Tubino, F., Piccardo, G. Tuned Mass Damper Optimization for the Mitigation of Human-Induced Vibrations of Pedestrian Bridges. *Meccanica,* **2015**, *50* 809-824.

22. Alhassan, M. A., Al-Rousan, R. Z., Al-Khasawneh, S. I. Control of Vibrations of Common Pedestrian Bridges in Jordan Using Tuned Mass Dampers. *Procedia Manufacturing,* **2020**, *44* 36-43.

23. Werkle, H., Butz, C., Tatar, R. Effectiveness of "Detuned"TMD's for Beam-Like Footbridges. *Advances in Structural Engineering,* **2013**, *16* No 1.

24. Yamaguchi, H., Harnpornchai, N. Fundamental Characteristics of Multiple Tuned Mass Dampers for Suppressing Harmonically Forced Oscillations. *Earthquake Engineering and Structural Dynamics* **1993**, *22*, 51-62.

25. Li, Q., Fan, j., Nie, J., Li, Q, Chen, Y. Crowd-induced Random Vibration of Footbridge and Vibration Control using Multiple Tuned Mass Dampers. *Journal of Sound and Vibration* **2010**, *329*, 4068-4092.

26. Pinkaew, T. Fujino, Y. Effectiveness of Semi-active Tuned Mass Dampers Under Harmonic. *Engineering Structures.* **2001** *850-856*

27. Wang, L., Nagarajaiah, S., Shi, W., Zhou, Y. Semi-active Control of Walking-Induced Vibrations in Bridges using Adaptive Tuned Mass Damper Considering Human-Structure-Interaction. *Engineering Structures.* **2021** *112743*

28. Yao, J.T.O. Concept of Structural Control. *Journal of Structural Division (ASCE).* **1972**, *Vol. 98 Iss: 7*, 1567-1574.

29. Saeed, T. E.; Nikolakopoulos, G.; Jonasson J-E.; Hedlund, Hans. A State-of-Art Review of Structual Control Systems. *Journal of Vibration and Control.* **2015**, *21(5)*, 919-937.

30. Makris, N. Seismic Isolation: Early History *Earthquake Engng Struct Dyn.,* **2018**. *1-15*

31. Elsesser, E.; Jokerst, M.; Naaseh, S. Historic Upgrades in San Francisco. *Civil Engineering* **1997**, *67(10)*, 50-53.

32. City and County of San Francisco. *https://sf.gov/location/san-francisco-city-hall* **Accessed 16 September 2023**.

33. Engineering News-Record. The 10 Largest Base-Isolated Buildings in the World. *https://www.enr.com/articles/42366-the-10-largest-base-isolated-buildings-in-the-world* **Accessed 16 September 2023**.

34. Symans, M.D.; Charney, F.A.; Whittaker, A.S.; Constantinou, M.C.; Kircher, C.A.; Johnson, M.W.; and McNamara, R.J. Energy Dissipation Systems for Seismic Applications: Current Practice and Recent Developments. *J. Struct Eng* **2008**, *134(1)*, 3-21.

35. Javanmardl, A.; Ibrahlm, Z.; Ghaedl, K.; Ghadlm, H.B. Hanlf, M.U. State-of-the-Art Review of Metallic Dampers: Testing, Development and Implementation. *Arch Computat Methods Eng.* **2020**, *27*, 455-478.

36. Pall, A.S.; Masch, C.; Fazio, P. Friction Joints for Seismic Control of Large Panel Structures. *PCI Journal* **1980**, *25(6)*, 38-61.

37. Pall, A.S.; Masch, C. Friction-damped concrete shearwalls. *Journal Proceedings* **1981**, *78(3)*, 187-193.

38. Jaisee, S. Yue, F. Ooi, Y.H. A State-of-the-Art Review on Passive Friction Dampers and their Applications. *Engineering Structures* **2021**, *235*, 112022.

39. Soong T.T. State-of-the-Art Review: Active Structural Control in Civil Engineering. *Engineering Structures* **1988**, *Vol 10, Issue 2*, 74-84.

40. Ikeda, Y. Active and Semi-active Control of Buildings in Japan. *Journal of Japan Association for Earthquake Engineering* **2004**, *Vol 4, No 3*, Special Issue.

41. Symans, M.D.; Constantinou, M.C. Semi-active Contro Systems for Seismic Protection of Structures: A State of the Art Review. *Engineering Structures* **1999**, *21*, 469-487.

42. Kobori, T.; Takahashi, M.; Nasu, T.; Niwa, N. and Ogasaware, K. Seismic Response Controlled Structure with Active Variable Stiffness System. *Earthquake Engineering and Structural Dynamics* **1993**, *22*, 925-941.

43. Weber, F.; Boston C.; Maslanka M. An Adaptive Tuned Mass Damper Based on the Emulation of Positive and Negative Stiffness with an MR Damper. *Smart Mater. Struct.* **2011**, 20, 015012. F. Weber, C. Boston, M. Maślanka

44. Weber, F. Semi-active Vibration Absorber Based on Real-Time Controlled MR Damper. *Mechanical Systems and Signal Processing* **2014**, 46(2), 272-288.

45. Weber, F.; Distl, H.; Fischer, S.; Braun, C. MR Damper Controlled Vibration Absorber for Enhanced Mitigation of Harmonic Vibrations *Actuators* **2016**, 5, 27.

46. Aly, S.; Ramaswamy, A. Semi-active Base Isolation System for Buildings using MR Dampers https://earthquake.usgs.gov/hazards/interactive/ **accessed on date October 2023**.

47. Dounis, A. I.; Tiropanis, P.; Syrcos, G. P.; Tseles, D. Evolutionay Fuzzy Logic Control of Base-Isolated Structures in Response to Earthquake Activity. *Struct. Control Health Monit.* **2007**, 14, 62-82.

48. Shook, D.A.; Roschke, P.N.; Ozbulut, O. E. Superelastic Semi-active Damping of a Base-isolation Structure. *Struct. Control Health Monit.* **2008**, 15, 746-768.

49. Stanway, R.; Sproston, J. L.; and Stevens, N. G. Non-linear Identification of an Electrorheloligical Vibration Damper. *IFAC Identification and Sys. Parameter Estimation.* **1985**, 195-200.

50. Gamota, D. R. and Filisko, F. E. Dynamic Mechanical Studies of Electrorheological Materials: Moderate Frequencies. *J. Rheol.* **1991**, 35, 399.

51. Bouc, R. Modèle Mathématique Dh̀ystérésis: Application Aux Systèmes à un Degrè de Libertè. *Acustica (in French)* **1971**, 24, 16-25.

52. Spencer B.F., Dyke S.J., Sain M.K., and Carlson J.D. Phenomenological Model of a Magnetorheological Damper. *Engineering Mechanics* **1997**, *122*, 3.

53. Kwok, N. M.; Ha, Q. P.; Nguyen, T. H.; Samali, Li. B. A Novel Hysteretic Model for Magnetorheological Fluid Dampers and Paramter Identification using Particle Swarm Optimization. *Sensors adn Actuators.* **2006**, 132, 441-451.

54. Barrera-Vargas, C.A., Díaz, I.M., García-Palacios, J.H., Soria, J.M. Semi-active Tuned Mass Damper: Magnetorheological Damper Identification and Performance Evaluation. *Conference on Structural Dynamics* **2021**, *Gijón, España.*

55. Wen, Y. K. Method for Random Vibration of Hysteretic Systems. *Journal of Engineering Mechanics. American Society of Civil Engineers.* **1976**, 102(2), 249–263.

56. Zhang, S.; Shi, W.; Chen, Z. Modeling and Parameter Identification of MR Damper Considering Excitation Characteristic and Current. *Shock and Vibration.* **2021**, ID 6691650, 17.

57. Aziz, M. A.; Mohtasim, S. M.; Ahammed, R. State of the Art Recent Developments of Large Magnetorheological (MR) Dampers: A Review. *Korea-Aust. Rheol. J.* **2022**, 34, 105-136.

58. Yoshida, O. and Dyke, S. J. Seismic Control of a Nonlinar Benchmark Building Using Smart Dampers. *Journal of Engineering Mechanics-ASCE.* **2004**, 130, 386-392.

59. Jung, H.; Choi, K.; Park, K. Cho, S. Seismic Protection of Base Isolated Structures using Smart Passive Control System. *Smart Structures and Systems.* **2007**, 3, 385-403.

60. Ha, Q. P.; Kwok, N. M.; Nguyen, M. T.; Li, J. and Samali, B. Mitigation of Seismic Response on Building using MR Dampers with Lyapunvo-Based Control. *Struct. Control Health Monit.* **2008**, 15, 604-621.

61. Preumont, A. Vibration Control of Active Structures An Introduction. *Kluwer Academic Publishers* **2007**.

62. Weber, F.; Feltrin, G. and Olaf, H. SAMCO Final Report - F05 Guidelines for Structural Control. *Tech. Rep. Structural Engineering Research Laboratory, Swiss Federal Laboratories for Materials Testing and Research.* Dübendorf, Switzerland, 2006.

63. Bitaraf, M.; Ozbulut, O. E.; Hurlebaus, S.; Barroso, L. Application of Semi-active Control Strategies for Seismic Protection of Buildings with MR Dampers. *Engineering Structures.* **2010**, 32, 3040-3047.

64. Xu, Lh.; Li, ZX. Semi-active Predictive Control Strategie for Seismially Excited Structures Using MRF-04K Dampers. *J. Cent. Sourth Univ.* **2012**, 19, 2496-2501.

65. Soong, T.T.; Dargush, G.F. Passive Engery Dissipation Systems in Structural Engineering. *Willey, New York* **1997**.

66. Koo, J.H.; Ahmadian, M.; Setareh, M.; Murray, T.M. In Search of Suitable Control Methods for Semi-active Tuned Vibration Absorbers. *J. Vib. Control* **2004**, *10*, 163–174.

67. Karnopp, D. C. Active and Semi-active Vibration Isolation. *Journal of Mechanical Design.* **1995**, 117, 177-185.

68. Aguirre, N. Magnetorheological Dampers: Modeling and Control Design for Civil Engineering Structure. *Universitat Politècnica de Catalunya* **2011**, *Barcelona, Spain.*

69. Hanagan L.M. Active Control of Floor Vibrations. *Virginia Polytechnic Institute and State University* **1994**, *Blacksburg, Virginia.*

70. Nyawako, D.; Reynolds, P. Response-dependent Velocity Feedback Control for Mitigation of Human-Induced Floor Vibrations. *Smart Mater. Struct.* **2009**, *18*, 075002.

71. Frahm H. Device for Damping Vibration of Bodies. (*US patent 989,958*) **1911.**

72. Yang, F., Sedaghati, R., Esmailzadeh, E. Vibration Suppression of Structures using Tuned Mass Damper Technology: A State of the Art Review. *Journal of Vibration and Control* **2022** *Vol 28* 812-836.

73. Den Hartog J. P. Mechanical Vibrations. *New York: McGraw-Hill* **1956.**

74. Wang, D., Wu, C., Zhang, Y., Li, S. Study on Vertical Vibration Control of Long-Span Steel Footbridge with Tuned Mass Dampers under Pedestrian Excitation. *Journal of Construction Steel Research* **2019**, *154* 84-98.

75. Liu K, Liu L, Zhu Q, Liu Y, Zhou F. Dynamic Testing and Numerical Simultation of Human-Induced Vibration of Cantilevered Floor with Tuned Mass Dampers. *Structures* **2021**, *34* 1475-1488.

76. Garcia-Troncoso N, Ruiz Teran A, Stafford PJ. Attenuation of Pedestrian-induced Vibrations in Girder Footbridge using Tuned Mass Dampers *Advances in Bridge Engineering* **2020**, 1:14.

77. Xu YL, Kwok KCS, Samali B. Control of Wind-Induce Tall Building Vibration by Tuned Mass Dampers. *Journal of Engineering and Industrial Aerodynamics* **1992**, *40* 1-32.

78. Elias S, Matsagar V. Wind Response Control of Tall Building with a Tuned Mass Damper. *Journal of Building Engineering* **2018**, *15* 51-60.

79. Lu Z, Xiaoyi C, Zhang D, Dai K. Experimental and Analytical Study on the Performance of Particle Tuned Mass Dampers under Seismic Excitation. *Earthquake Enginnering and Structural Dynamics* **2017**, *46* 697-714.

80. Salvi J, Pioldi F, Rizzi E. Optimum Tuned Mass Damper under Seismic Soil-Structure Interaction. *Soil Dynamics and Earthquake Engineering* **2018**, *114* 576-597.

81. Pinkaew T, Lukkunaprasit P, Chatupote P. Seismic Effectiveness of Tuned Mass Dampers for Damage Reduction of Structures. *Engineering Structures* **2003**, *25* 39-46.

82. Shi W, Wang L, Lu Z, Zhang Q. Application of an Artificial Fish Algorithm in an Optimum Tuned Mass Damper Design for a Pedestrian Bridge. *Appli. Sci.* **2018**, *8* 175.

83. Greco R, Marano GC, Fiore A. Performance-Cost Optimization of Tuned Mass Damper under Low-Moderate Seismic Actions. *Struc.Design Tall Spec. Build.* **2016**, *25* 1103-1122.

84. Barrera-Vargas, C.A., Naranjo-Pérez, J., Díaz, I.M., García-Palacios, J.H. Design of a Semiactive TMD for Lightweight Pedestrian Structures Considering Human-Structure-Actuator Interaction. *Actuators* **2022**, *11,101.*

85. Zhang, D.; Pan, P.; Zeng, Y.; Guo, Y. A Novel Robust Optimum Control Algorithm and Its Application to Semi Active Controlled Base Isolated Structures. *Bull. Earthq. Eng.* **2020**, *18*, 2431-2460.

86. Gu, X.; Yu, Y.; Li, Y.; Li, J.; Askari, M.; Samali, B. Experimental Study of Semi-active Magnetorheological Elastomer Base Isolation System using Optimal Neuro Fuzzy Logic Control. *Mech. Syst. Signal Process.* **2019**, *119*, 380–398.

87. Moutinho, C. Testing a Simple Control Law to Reduce Broadband Frequency Harmonic Vibrations using Semi-active Tuned Mass Dampers. *Smart Mater. Struct.* **2015**, *24*, 055007.

88. Gallegos-Calderón, C.; Naranjo-Pérez, J.; Díaz, I.M.; Goicolea, J.M. Identification of a Human-Structure Interaction Model on an Ultra-Lightweight FRP Footbridge. *Appl. Sci.* **2021**, *11*, 6654.

89. Dougill, J.W.; Wright, J.R.; Parkhouse, J.G.; Harrison, R.E. Human Structure Interaction during Rhythmic Bobbing. *Struct. Eng.* **2006**, *84*, 32–39.

90. Díaz, I.M.; Gallegos-Calderón, C., Ramírez Senent, J.; Renedo, C.M.C. Interaction Phenomena to Be Accounted for Human-Induced Vibration Control of Lightweight Structures. *Front. Built Environ.* **2021**, *7*, 658529.

91. ACMA. Pre Standard for Load and Resistance Factor Design (LRFD) of Pultruded Fiber Reinforced Polymer (FRP) Structure. *American Society of Civil Engineers ASCE* **2010**, *Reston (Virginia), United State.*

92. Shahabpoor, E.; Pavic, P.; Racic, V. Interaction between Walking Humans and Structure in Vertical Direction: A Literature Review. *Shock Vib.* **2016**, 3430285.

93. Zhang, M.; Georgakis, C.T.; Chen, J. Biomechanically Excited SMD Model of a Walking Pedestrian. *J. Bridge Eng.* **2016**, *21*, C4016003.

94. Ahmadi, E.; Caprani, C.; Ẑivanovic, S.; Heidarpour, A. Experimental Validation of Moving Spring-Mass-Damper Model for Human-Structure Interaction in the Presence of Vertical Vibrations. *Structures* **2021**, *29*, 1274-1285.

95. Butz, C.; Heinemeyer, C.; Goldack, A.; Keil, A.; Lukic, M.; Caetano, E.; Cunha, A. Advanced Load Models for Synchronous Pedestrian Excitation and Optimised Design Guidelines for Steel Footbridges. *Res. Fund Coal Steel Eur. Commision* **2008**, Final report, 167.

96. Blasco, X.; Herrero, J.M.; Sanchis, J.; Martínez, M. A New Graphical Visualization of N-Dimensional Pareto Front for Decision-Making in Multiobjective Optimization. *Inf. Sci.* **2008**, *128*, 3908-3924.

97. Soria, J.M.; Díaz, I.M.; García-Palacios, J.H. Further steps towards the tuning of inertial controllers for broadband-frequency-varying structures. *Struct Control Health Monit.* **2020**, *27*, 2461.

98. Díaz, I.M.; Reynolds, P. Robust Saturated Control of Human-Induced Floor Vibrations via a Proof-Mass Actuator. *Smart Mater. Struct.* **2009**, *18*, 125024.

99. Rosada, M. E. Aislamiento Sismico: Una Alternativa para Mejorar la Respuesta Sísmica de Estructuras. *Congreso Latinoamericano "Resiliencia Sísmica de las Edificaciones"ICCG y AGIES* **2018**, *Ciudad de Guatemala, Guatemala.*

100. Genatios, C., Lafuente, M. Introducción al Uso de Aisladores y Disipadores en Estructuras. *Serie GeóPolis,* **2016**, *Caracas: CAF.*

101. Kelly, J.M., Konstantinidis D. A. Mechanics of Rubber Bearing for Seismic and Vibration Isolation. *A John Wiley & Sons, ltd Publication* **2011**.

102. Kelly, J.M., Shinner, R. I. and Heine, A. J. Mechanisms of Energy Absorption in Special Devices for Use in Earthquake Resistant Structures. *Bulletin of N.Z. Society for Earthquake Engineering* **1972**, *Vol. 5 No 3*

103. Shinner, R. I., Kelly, J. M. and Heine, A. J. Hysteretic Dampers for Earthquake-Resistant Structures. *Earthq Eng Struct Dyn.* **1974**, *287-296*

104. Kelly, J. M. Earthquake Resistant Design with Rubber Second Edition. *NY: Springer* **1997**.

105. Turkingon, D.H., Carr, A. J., Cooke, N. and Moss, P. J. Seismic Design of Bridges on Lead Rubber Bearings. *Journal of Structural Engineering* **1989**, *Vol 115 No 12.*

106. Eem, S., Hahm, D. Large Strain Nonlinear Model of Lead Rubber Bearings for Beyond Design Basis Earthquake. *Nuclear Engineering and Technology* **2019**, *Vol 51, Issue 2* 600-606.

107. Hwang, J. S., Ku, S. W. Analytical Modeling of High Damping Rubber Bearings. *Journal of Structural Engineering* **1997**, *Vol 123, No 8.*

108. Deringöl, A. H., Güneyisi, E. M. Effect of Using High Damping Rubber Bearings for Seismic Isolation of the Buildings. *International Journal of Steel Structures* **2021**, *21(5)* 1698-1722.

109. Bekdaş G, Nidgeli SM. Estimating Optimum Parameters of Tuned Mass Dampers using Harmony Search. *Engineering Structures* **2011**, *33* 2716-2723.

110. Stanton, J F , Roeder C W. Elastomeric Bearings Design, Construction, and Materials. *National Cooperative Highway Research Program* **1982**, *Report 248.*

111. Chopra A K, Dynamic of Structure: 4th Edition *Pearson Education* **2012**, *Prentice Hall.*

112. Zelleke, D.; Matsagar, V. Energy-Based Predictive Algorithm for Semi-active Tuned Mass Dampers. *Struct. Des. Tall Spec. Build.* **2019**, *12*, 1–20.

113. Akiyama, H. Earthquake Resistant Design Method for Buildings Based on Energy Balance. *Reverté, S.A.: Tokyo, Japan* **2002**.

114. ACSE. Minimum Design Loads and Associated Criteria for Buildings and Other Structures. *The American Society of Civil Engineers* **2017**, *Reston, Virginia, USA.*

115. Agudelo, J.A. ACELSIN©. Available online: https://estructurando.net/descargas/software/ (accessed on date February 2020).

116. Gasparini, D.; Vanmarcke, E. Simulated Earthquake Motions Compatible with Prescribed Responde Spectra. *Department of Civil Engineering, Massachussets Institute of Technology* **1976**, *Cambridge, MA, USA.*

117. PEER. The Web-Based Pacific Earthquake Engineering Research Center. Available online: https://https://ngawest2.berkeley.edu (accessed on date July 2020).

118. Qu,Z-Q. Model Order Reduction Techniques: with Applications in Finite Element Analysis. *Springer-Verlag London.* **2004**.

119. Chopra A K, Dynamic of Structure: 4th Edition. *Pearson Education* **2012** *Prentice Hall.*

120. Preumont, A.; Seto, K. Active Control of Structures. *John Wiley & Sons, Ltd.* **2008**.

121. Domenico, D.; Gandeli, E.; Quanglini, V. Adaptive Isolation System Combining Low-friction Sliding Pendulum Bearings and SMA-Based Gap Dampers. *Eng. Struct.* **2020**, *212*, 110536.

122. Ponzo, F.; Di Cesare, A.; Leccese, G.; Nigro, D. Standard Requirements for the Recentring Capability of Curved Surface Sliders. *Ing. Sismica* **2019**, 3, 3323-3332.

123. USGS. United State Geological Survey. Available online: https://earthquake.usgs.gov/hazards/interactive/ **accessed on date October 2023**.

124. Xu, ZD.; Shen, YP.; Guo, YQ. Semi-active Control of Structures Incorporated with Magnetorheological Dampers using Neural Networks. *Smart Mater. Struct.* **2003**, 12, 80-87.

125. Masa'id, A.; Lenggana, B. W.; Ubaidillah, U.; Susilo, D. D.; Choi, SB. A Review on Vibration Control Strategies Using Magnetorheological Materials Actuators: Application Perspective. *Actuators* **2023**, 12, 113.

126. Spencer B.F.; Yang, G.; Carlson, J.D.; Sain M.K. Smart Dampers of Seismic Protection of Structure: A Full-Scale Study. *Second World Conference on Structural Control* **1998**, *Kyoto, Japan.*

127. Li, T. Yang, Y. Day, K. Ge, Q. Wang, J. Influence of Ground Motion Duration on Seismic Performance of RC Frame Isolated by High Damping Rubber Bearings. *Engineering Structures* **2022**, *262* 114398.

128. Mokha, A., Constantinou, M.C., Reinhorn, A. M., Zayas, V. A. Experimental Study of Friction Pendulum Isolation System. *Journal of Structural Engineering,* **1991** *Vol 117, No 4.*

129. Fenz, D. M., Constantinou, M. C. Spherical Sliding Isolation Bearings with Adaptive Behavior: Theory. *Earthquake engineering and Structural Dynamics* **2008**, *37* 163-183.

130. Weber, F., Distl, J. Braun, C. Isolation Performance Assessment of Adaptive Behaviour of Triple Friction Pendulum. *Journal of Civil Engineering Research* **2017**, *7* 17-33.

131. Makris, N., and Moghimi, G. Response of Seismic Isolated Structures with Supplemental Rotational Inertia. *Earthquake Engng Struct Dyn.* **2022**, *51(12)* 2956-2974.